Eur. Phys. J. Special Topics **181**, 1-103 (2010)

DOI: 10.1140/epjst/e2010-01221-4

THE EUROPEAN PHYSICAL JOURNAL SPECIAL TOPICS

Review

Optics of surface disordered systems

A random walk through rough surface scattering phenomena

I. Simonsen[a]

Department of Physics, Norwegian University of Science and Technology (NTNU), 7491 Trondheim, Norway

Received 28 July 2009 / Received in final form 4 May 2010
Published online 14 June 2010

Abstract. No surface is perfectly flat at every length scale. However, all natural and man-made surfaces show some degree of roughness. Therefore, it is imperative to know how surface disorder may affect physical process at, or in the immediate vicinity, of the surface. In this review, we focus on the long-standing problem of electromagnetic wave scattering from randomly rough surfaces. This topic has implications and practical applications in fields of science and engineering ranging from observational astronomy to the electronic and medical industry. How randomly rough surfaces can be described statistically is outlined, and we introduce the theoretical and computational methods most frequently used in the study of light scattering from randomly rough metal or dielectric surfaces. A large part of the review is devoted to the description and the discussion of the physical origin behind various multiple scattering phenomena that can exist when light interacts with a random surface. Some of the addressed phenomena are; the enhanced backscattering and satellite peak phenomena; forward scattering (specular peak) enhancement; coherent effects in the angular intensity correlation functions and the second harmonic generated light (nonlinear effect).

Contents

[a] e-mail: Ingve.Simonsen@ntnu.no

1 Introduction

We are surrounded by waves, and they effect our daily life in ways that many of us are not fully aware. Sound and light are our main tools for observing our immediate surroundings. Light is for example responsible for you being able to read these lines, and more importantly, to get access to the vast majority of the knowledge accumulated in writing by man throughout centuries of intellectual activities. X-ray and ultra sound techniques have given tremendous contributions to the success of modern medicine. Radio- and micro-waves are invaluable in modern communication technology including cellular phones and radio and TV broadcastings. Understanding of quantum waves, and their behavior, constitutes the foundation of electronics and semiconductor technologies – an essential ingredient in the past and future progress of computer hardware. The above list is not at all, or intended to be, complete. It could in fact easily have been made much longer. However, the bottom line that we want to make here is that with the ubiquitous presence of wave phenomena in various applications, it is not surprising to find that wave phenomena have had, and still have, a prominent position in our understanding of the physical world, and such phenomena are of out-most importance in science, medicine and technology.

If you take an introductory text on wave phenomena, you will find discussions of how plane waves of well-defined frequency propagate in a homogeneous, isotropic medium [1–12]. Thereafter, the authors typically discuss the scattering and transmission of such waves at a *plan* interface separating two semi-infinite media of different dielectric properties – the Fresnel formulae [1–12]. These formulae serve to accurately describe the scattering of light from, say, a mirror. However, from our everyday experience, we know that most surfaces are not mirror like, and they are often more complicated than two semi-infinite media. Most naturally occurring surfaces are actually not smooth at all. They are, however, rough at some scale. In fact, all objects, man-made or not, *have* to be rough at the atomic scale even though such small length scales often are not resolved by our probes.

It should be kept in mind that the characterization of a surface as being rough or smooth is not unique, and it is, therefore, not an intrinsic property of the surface. Instead it depends on the wavelength used to "observe" the surface. If the typical roughness is on a scale much smaller than the wavelength of the probe, this surface is considered as smooth. However, by using another light source of shorter wavelength, the same surface might be characterized as being rough or maybe even strongly rough. It is, among other factors, the surface topography and the wavelength of the probe that together go into the characterization of a surface as being rough or smooth.[1]

[1] When discussing the Rayleigh criterion later in this section we will see that also the angle of incidence of the light will play an important role.

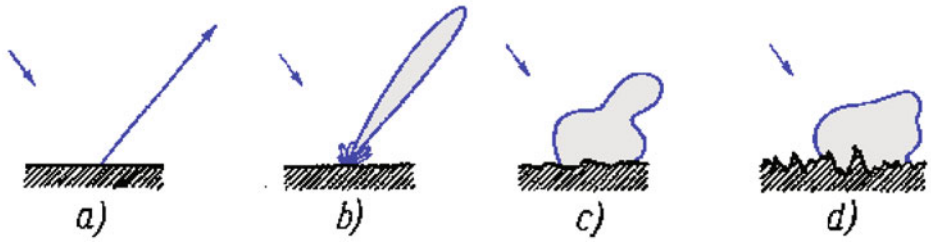

Fig. 1. An illustration showing the transition from specular (Fig. 1(a)) to diffuse scattering (Fig. 1(d)) of light from a surface of increasing roughness. The arrows indicate the direction of the incident light. (Adapted after Ref. [25].)

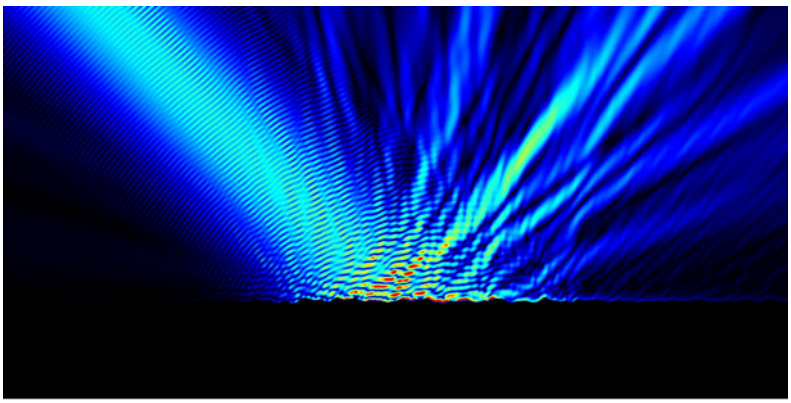

Fig. 2. When an electromagnetic wave is scattered (or transmitted) by a randomly rough surface, speckle patterns may result. The contour plot shows the spatial distribution of the intensity of light in the vicinity of a rough metal surface when it was illuminated from the top-left by a finite sized beam. The color scale is defined so that red corresponds to high intensity and blue to low (and black to zero). Notice in particular the "beams" of high intensity scattered from the surface in different directions ("the speckles"). These results were obtained on the basis of a rigorous computer simulation approach (see Sec. 4), and the assumed parameters were (meaning to be defined later): $\theta_0 = 45°$; $\lambda = 405\,\text{nm}$; $\delta = 50\,\text{nm}$; $a = 250\,\text{nm}$; $w = 10\lambda$; and $L = 80\lambda$. (Adapted after Ref. [45].)

Let us from now on assume an electromagnetic probe, *i.e.* light. If the surface can be considered as smooth (given the wavelength of the incident light), then the light is scattered (coherently) by the surface into the specular direction (Fig. 1(a)). As the roughness of the surface is increased so that the surface becomes weakly rough, a small fraction of the incident light will be scattered into other directions than the specular. This non-specular scattering is often called *diffuse scattering* or by some authors *incoherent scattering*. As the roughness is increased even further, the magnitude of the diffuse (incoherent) component of the scattered light is increased on the expense of the magnitude of the specular component. When the surface roughness is so that the specular component can be more-or-less neglected relative the diffuse component, the surface is said to be strongly rough. This transmission from as smooth to a strongly rough surface is depict in Figs. 1. Moreover, since a rough surface will give rise to a partly random phase of the scattered electromagnetic field, a complex intensity pattern will result due to the scattered field interfering constructively or destructively as angle of scattering is altered. Such patters are known as *speckle patterns* and they show rich properties that have fascinated researchers for decades [13–15]. Figure 2 presents an example of such a pattern obtained by a rigorous computer simulation approach described later in this review (Sec. 4).

Due to the practical applications of waves, and the number of naturally occurring surfaces being rough, it is rather remarkable that it took several hundreds years from the birth of optics as a scientific discipline to anyone started to consider wave scattering from rough surfaces. As far as we know today, the first such theoretical study was made at the end of the 19th century (probably in the year of 1877) by one of the greatest scientists of its time, the British physicist

Lord Rayleigh [16–18]. He considered the scattering of light incident normally onto a sinusoidal surface.

In 1913 Mandel'shtam studied how light was scattered from liquid surfaces [19]. By doing so, he became the first to consider scattering from *randomly* rough surfaces. This, as it turned out, should define the beginning of an active research area – *wave scattering from randomly rough surfaces* – which still today, almost a century later, is an active and vibrant field [12,25–44].

However, it was after the second world war that the research effort put into this field started to accelerate [20–24], and since then a massive body of research literature has been generated in the field [12,25–44].

Up to the mid 1980s, most of the theories used to study rough surface scattering were single scattering theories [25–30,32,33,38,39]. However, from then onward, the main focus of the research has been on multiple scattering theories [40,42,46]. In addition, advances in experimental techniques have lately enabled experimentalists to fabricate surfaces under well controlled conditions by using, *e.g.*, a holographic grating technique [47,48]. This has opened for the unique possibility of direct comparison of theory and experiments in a way not possible a few decades ago.

Inspired by the work of Lord Rayleigh [16–18] researchers developed a criterion – the Rayleigh criterion – that can be used to determine when a given surface is to be considered as rough. Here, in addition to the properties of the surface, the wavelength of the incident light and the angle of incidence are incorporated [29].

To illustrate how this comes about, let us consider a rough surface defined by $x_3 = \zeta(x_1)$. On this surface we pick two arbitrary points, say, $(x_1, \zeta(x_1))$ and $(x_1', \zeta(x_1'))$. Let us now ask ourselves the following question: What is the phase difference between two waves being scattered from these two surface points? For simplicity, we will here only consider the specular direction since a more complete treatment will be given in later sections. Under this assumption, it is straightforward from a geometrical consideration to show that the phase (optical path) difference between the two waves is given by the expression

$$\Delta\phi = 2\,|\mathbf{k}|\,|\zeta(x_1) - \zeta(x_1')|\cos\theta_0, \tag{1}$$

where $|\mathbf{k}| = 2\pi/\lambda$ is the modulus of the wave vector of the incident light of wavelength λ, and θ_0 is the angle of incidence of the light as measured from the normal to the mean surface. From Eq. (1) we immediately observe that if the surface is flat, so that $\zeta(x_1) = \zeta(x_1')$, then the phase difference (in the specular direction) is always zero independent of the angle of incidence. However, if the surface is rough, $\Delta\phi \neq 0$ in general. If $\Delta\phi \ll \pi$, the two waves will be in, or almost in, phase and they will therefore interfere constructively. On the other hand, if $\Delta\phi \simeq \pi$, they will be more-or-less completely out off phase and interfere destructively, so that less energy will be scattered into the specular direction as compared to the situation where the two waves interfere constructively. In terms of the phase, a smooth surface would correspond to $\Delta\phi \ll \pi$, and a rough to $\Delta\phi \simeq \pi$. Thus, $\Delta\phi = \pi/2$ might be considered as the borderline between a smooth and a rough surface; if $\Delta\phi < \pi/2$ the surface is smooth, and otherwise ($\pi/2 < \Delta\phi \leq \pi$) it is rough. The criterion $\Delta\phi < \pi/2$ is the famous Rayleigh criterion for a smooth surface.

If the surface is randomly rough, it is practical to replace the height difference $\zeta(x_1) - \zeta(x_1')$ by a typical height fluctuation as provided, for example, by the standard deviation or root-mean-square (rms) height, δ, of the surface. Hence, the Rayleigh criterion for a rough surface can be expressed as [29]

$$R_a = |\mathbf{k}|\,\delta\cos\theta_0 \quad < \quad \frac{\pi}{4}, \tag{2}$$

where R_a is the so-called Rayleigh parameter. From the Rayleigh criterion, $R_a < \pi/4$, it should be observed that in addition to the surface topography itself and the wavelength of the light, also its angle of incidence goes into determining if a surface is rough or not. This is probably the most important lesson to be learned today from the Rayleigh criterion.

During the time that has passed since Lord Rayleigh [16–18] conducted his seminal work on rough surface scattering in the 1870s, this topic has been studied extensively. Since real systems are not perfectly flat, and thus contain some degree of roughness, its effect needs to be taken into consideration if one wants an accurate description of the light scattered from a real system. Hence, it is fair to say that until rather recently, the presence of roughness was mostly considered as an extra complication – something that one did not want, but simply was

forced into accounting properly for in order to reach an adequate description of the system at hand. However, recently, and in particular with the advent of nano-technology, this situation has changed dramatically. Now, surface roughness may be considered an advantage and systems are intentionally designed with rough surfaces. In such cases the surface structures are often designed, or tailored and optimized, towards particular applications. One talks about *engineered surfaces* [34,49–52]. For instance in photovoltaic systems, it is known that surface roughness may increase the efficiency of solar cells even if the optimal structure for such applications is still partly unknown [53]. In order to be able to perform such engineering and to optimize the structures towards applications, a excellent fundamental understanding of how light interacts with rough structures is essential.

The present review consists of essentially two main parts – part one focuses on the theoretical methods whilst part two is devoted to rough surface scattering phenomenology. In the first part we try to present an overview of some of the main theories and methods used in the study of wave scattering from randomly rough surfaces. We begin in Sec. 2 to describe how randomly rough surfaces can be described statistically. We then continue by summarizing the important results of electromagnetic theory including Maxwell's equations and so-called surface plasmon polaritons (Sec 3). Section 4 is devoted to the quantities and main techniques used in the field of electromagnetic wave scattering from randomly rough surfaces. We here review classical theories like small amplitude perturbation theory, many-body perturbation theory as well as numerical simulation approaches. This section serves the purpose of outlining the various theories and simplifies referencing when later discussing optical phenomenas. Finally in Sec. 5 we address some of the interesting (and partly unique) optical phenomena that may occur when light is scattered from randomly rough surfaces. Such effects include the backscattering and satellite peaks phenomena (weak localization); enhanced forward scattering (enhanced specular peak) phenomenon; angular intensity correlation function effects; and nonlinear effects (second harmonic generation).

2 Characterization of random rough surfaces

Almost everyone grows up with some kind of intuitive "feeling" of what is meant by a rough surface. The surface of a fractured stone, say, is normally looked upon as being rough, while a piece of paper as being smooth. However, on the micro-scale, where the human eye is not very sensitive, also the paper has some kind of structure. So in a strict sense, both the paper and the stone surface are rough. Paper is made out of fibers which is quite different from the crystals that are seen on the micro scale of the surface of the fractured stone. So the question is: How shall we quantify the difference in roughness between say the paper and the stone surface? One possibility is to measure by some suitable technique the surface topography. Such measurements will of course produce different results for the paper and stone surface. However, if we move to another area of the fractured stone and measure the surface topography here, we will obviously not get the same result as obtained in the previous measurement taken from another area of the same surface. So, how shall we be able to characterize the rough surfaces at hand, so that we are able to distinguish them from each other? In this section we intend to discuss in some detail how to characterize randomly rough surfaces in a quantitative way.

However, before we do so, let us take a look at what kind of rough surfaces we have. Depending on how the surface height fluctuates around some reference surface, we may categorize them as being deterministic or randomly rough. For random surfaces, one may in addition group them as correlated or uncorrelated surfaces, and they might occur as fractal or non-fractal surfaces depending on under which conditions they were formed. Rough surfaces that are found in nature are normally correlated randomly rough surfaces. We will therefore proceed by discussing how to characterize such surfaces [29,54,55].

2.1 Statistical description of randomly rough surfaces

Two randomly rough surfaces are never identical. Thus the knowledge of the surface topography alone is therefore not enough to be able to immediately say if two rough surfaces were generated

by the same underlying process, and therefore have to be looked upon as being identical (in a statistical sense). However, if we assume that the randomly rough surface can be considered as a continuous random process [56–61], then a statistical description might be relevant and useful. We will now introduce this method of characterization.

Under experimental conditions, the surface topography is measured relative to some reference surface. In our case we will assume that this reference surface is a planar surface. Other choices might be practical in some cases, but this will not be discussed here. Furthermore, it is convenient to choose our coordinate system so that this planar surface is located at $x_3 = 0$. In this case the randomly rough surface is just the roughness that perturb the plane $x_3 = 0$. For simplicity, we limit our discussion to one-dimensional surfaces. The extension to (isotropic) two-dimensional surfaces is trivial. For the purpose of this review it will be assumed that the surface does not possess any overhangs[2], that is to say that the surface profile function, that we will denote by $\zeta(x_1)$, is a single-valued function of the lateral coordinate x_1. For characterization of surfaces where the surface profile function does not fulfill this property the reader is invited to consult Refs. [45,62,63].

In order for the surface profile function $\zeta(x_1)$ to be planar on average, it must, with our choice for the coordinate system, have a vanishing mean, *i.e.* we must require that

$$\langle \zeta(x_1) \rangle = 0. \tag{3}$$

Here the angle brackets are used to denote a spatial average over a large spatial region. If, however, the surface is *ergodic* [57–61], as we will assume here, this spatial average is equal to an average over an ensemble of realizations of $\zeta(x_1)$. It is therefore, under the assumption of ergodicity, more convenient to think of $\langle \cdot \rangle$ as an ensemble average.

Another notion that is important when characterizing rough surfaces is *stationarity* [29]. A surface is said to be stationary, or translation invariant, if its statistical properties are independent of which portion of the surface was used in their determination. That the surface roughness possesses stationarity is crucial for the applicability of many of the theories used to study rough surface scattering. Rigorous numerical simulations (Sec. 4.10), however, can still handle non-stationary surfaces.

2.1.1 Gaussian random surfaces

In theoretical studies of light scattering from rough surfaces, the random surfaces have in the overall majority of the studies been assumed to possess Gaussian height statistics. Such a statistics is rather appealing from a theoretical point of view since moments of any order can be related to the first two moments. Such moments either vanish (odd moments), or they are related to the second moment (even moments) [29]. Fortunately, also real surfaces are often found to be Gaussian of which one example is given in Figs. 3.

The zero-mean property, Eq. (3), does not specify how the different heights along the surface are located relative to one another. Such information is provided by the height-height correlation function. Under the assumption of $\zeta(x_1)$ being stationary we can write

$$\langle \zeta(x_1)\zeta(x_1') \rangle = \delta^2 W(|x_1 - x_1'|), \tag{4}$$

where δ is the root-mean-square (rms)-height of the surface profile function, and $W(|x_1|)$ is the height auto-correlation function normalized so that $W(0) = 1$. In cases where $W(|x_1|) = 1$ ($W(|x_1|) = -1$) one speaks of perfect correlation (anti-correlation). Furthermore it can be shown that $-1 \leq W(|x_1|) \leq 1$. Notice, that since the heights-distribution is Gaussian, Eqs. (3) and (4) together determines uniquely the statistical properties of the surface since all higher order moments can (for a Gaussian surface) be related to the first two.

In many of the perturbation theories developed for rough surface scattering, the power spectrum of the surface randomness is a quantity that appears more-or-less naturally. It is

[2] Such surfaces are also known as reentrant surfaces.

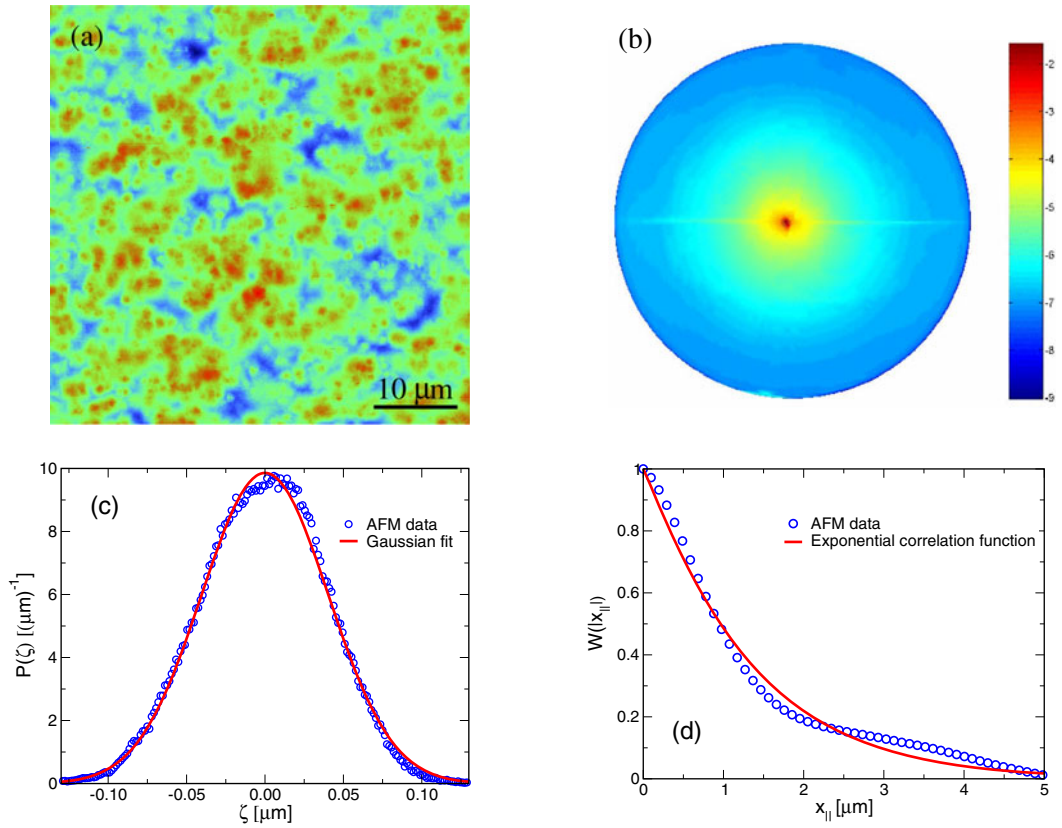

Fig. 3. Experimental height and light transmission measurements performed on a plastic film (a melt blown, linear low density polyethylene film of (mean) thickness $d = 50\,\mu m$). (a) A contour plot of the experimental surface profile function obtained from Atomic Force Microscopy (AFM) measurements over a $50 \times 50\,(\mu m)^2$ quadratic area. The color code is so that red corresponds to $0.015\,\mu m$ and blue to $-0.015\,\mu m$. Similar statistical properties were found for the top and bottom surface of the film. (b) Contour plot for the angular distribution of the measured logarithmic intensity of light of wavelength $\lambda = 0.6328\,\mu m$ that has been transmitted through the film. (c) The height distribution function $P(\zeta)$ calculated from the AFM data (open circles) and a Gaussian fit (solid line) corresponding to $\delta = 0.04\,\mu m$. (d) The height-height correlation function $W(|x_\parallel|)$ obtained from the AFM data (open circles) and, for comparison, an exponential correlation function $W(|x_\parallel|) = \exp(-|x_\parallel|/a)$ (solid line) corresponding to a correlation length of $a = 1.3\,\mu m$. It is observed that the empirical correlation function is more complex than a simple exponential function. (Adapted after Ref. [129].)

defined as the Fourier transform of the (normalized) correlation function [64]

$$g(|k|) = \int_{-\infty}^{\infty} dx_1\, W(|x_1|)\, e^{-ikx_1}. \tag{5}$$

In order to get an intuitive picture of how the surface height varies along the surface, it is often useful to supply the mean slope, s, and the mean distance between consecutive peaks and valleys, $\langle D \rangle$, as measured along the (lateral) x_1-direction. For a stationary zero-mean, Gaussian random process, the rms-slope, s, is related to the power spectrum by [64]

$$s = \left\langle [\zeta'(x_1)]^2 \right\rangle^{1/2} = \delta \sqrt{\int_{-\infty}^{\infty} \frac{dk}{2\pi}\, k^2 g(|k|)}, \tag{6}$$

and a good estimator for $\langle D \rangle$ has been shown to be [64]

$$\langle D \rangle \simeq \pi \sqrt{\frac{\int_{-\infty}^{\infty} dk\ k^2 g(|k|)}{\int_{-\infty}^{\infty} dk\ k^4 g(|k|)}}. \tag{7}$$

In the literature many different forms for the correlation function $W(|x_1|)$ have been considered (see *e.g.* Ref. [29] and references therein). However, here we will only be dealing with two such forms. They are the Gaussian form given by

$$W(|x_1|) = \exp\left(-\frac{x_1^2}{a^2}\right), \tag{8a}$$

$$g(|k|) = \sqrt{\pi} a\ \exp\left(-\frac{a^2 k^2}{4}\right), \tag{8b}$$

where a is the transverse correlation length, and the so-called rectangular or West-O'Donnell form

$$W(|x_1|) = \frac{\sin k_+ x_1 - \sin k_- x_1}{(k_+ - k_-)x_1}, \tag{9a}$$

$$g(|k|) = \frac{\pi}{k_+ - k_-}[\theta(k_+ - k)\theta(k - k_-) + \theta(k_+ + k)\theta(-k - k_-)], \tag{9b}$$

where $\theta(\cdot)$ is the Heaviside unit step function. In Eqs. (9) the quantities $k_\pm$, with $0 < k_- < k_+$, denote the lower and upper momentum cutoffs for the spectrum, and they will be given a more precise definition in later sections. The latter power spectrum was recently used by West and O'Donnell [65] in an experimental study of the enhanced backscattering phenomenon from weakly rough surfaces.

For the two above power spectra the mean slope, s, and the distance between consecutive peaks and valleys, $\langle D \rangle$, then become [64]

$$s = \begin{cases} \sqrt{2}\dfrac{\delta}{a}, & \text{Gaussian} \\ \dfrac{\delta}{\sqrt{3}}\sqrt{k_+^2 + k_+ k_- + k_-^2}, & \text{West} - \text{O}'\text{Donnell} \end{cases}, \tag{10}$$

and [64]

$$\langle D \rangle = \begin{cases} \dfrac{\pi}{\sqrt{6}} a, & \text{Gaussian} \\ \pi\sqrt{\dfrac{5}{3}\dfrac{k_+^3 - k_-^3}{k_+^5 - k_-^5}}, & \text{West} - \text{O}'\text{Donnell} \end{cases}. \tag{11}$$

Two surface profiles with the same (Gaussian) height distribution, but with a Gaussian and a West-O'Donnell power spectrum possessing nearly the same value of the rms-slope, s, are depicted in Figs. 4.

In later calculations, it will prove useful to also have available the Fourier representation of the surface profile function (and its Fourier inverse). They are defined as

$$\zeta(x_1) = \int_{-\infty}^{\infty} \frac{dk}{2\pi}\ \tilde{\zeta}(k) e^{ikx_1}, \tag{12a}$$

(12b)

and

$$\tilde{\zeta}(k) = \int_{-\infty}^{\infty} dx_1\ \zeta(x_1) e^{-ikx_1}. \tag{12c}$$

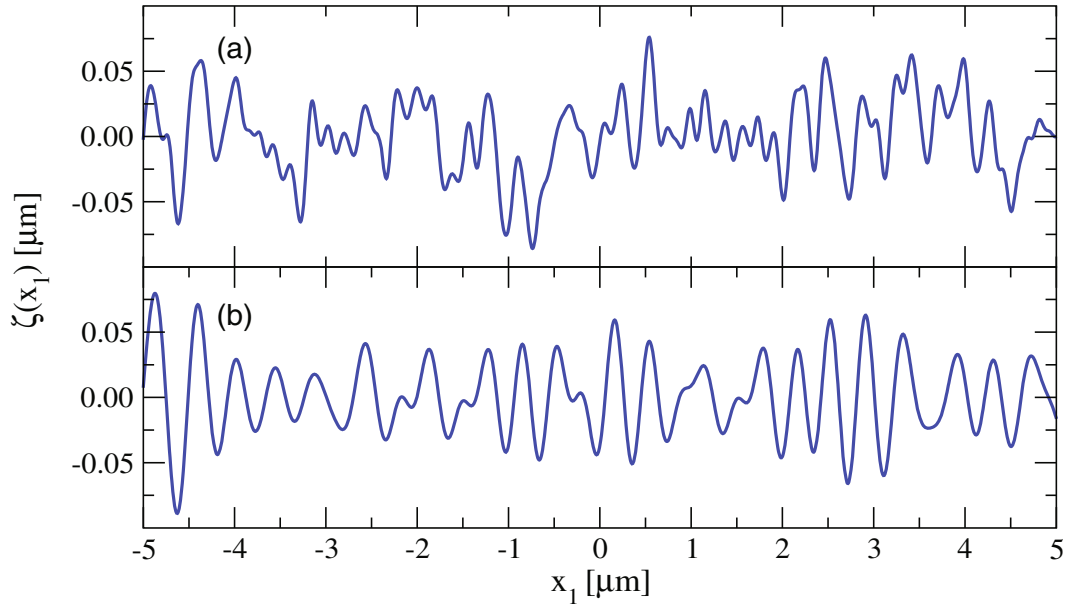

Fig. 4. Examples of two rough profiles both with Gaussian height distributions and with an rms-value $\delta = 30\,\text{nm}$. The power spectrum is of (a) the Gaussian type, with $a = 100\,\text{nm}$, and (b) the West-O'Donnell type, with $k_- = 0.82(\omega/c)$ and $k_+ = 1.97(\omega/c)$ with $\lambda = 632.8\,\text{nm}$ ($\omega/c = 2\pi/\lambda$). With these parameters, the rms-slope and distance between consecutive peaks and valleys are respectively $s = 0.424$ and $\langle D\rangle = 128.3\,\text{nm}$ for the Gaussian power spectrum, and $s = 0.427$ and $\langle D\rangle = 201.1\,\text{nm}$ in case of the West-O'Donnell power spectrum. Note that there are different scales on the first and second axes, with the result that the profiles appear much rougher than they are in reality. The two surface profiles where generated from the same underlying uncorrelated random numbers.

The Fourier transform of the surface profile function, $\tilde{\zeta}(k)$, also constitutes a zero-mean Gaussian random process with statistical properties [64]

$$\left\langle \tilde{\zeta}(k) \right\rangle = 0, \tag{13a}$$

$$\left\langle \tilde{\zeta}(k)\tilde{\zeta}(k') \right\rangle = 2\pi\delta(k+k')\delta^2 g(|k|), \tag{13b}$$

where $\delta(\cdot)$ denotes the Dirac delta function.

2.1.2 Non-Gaussian Random Surfaces

Naturally occurring surfaces can often show more complicated height distributions than the Gaussian [29]. To fully characterize such surfaces are quite difficult and probably explains why they have received less attention in the literature then they probably deserve. The main problem is that in order to characterize them statistically, moments of in principle infinite order have to be known. These moments are not, as for Gaussian surfaces, related to moments of lower order in a trivial way since the characteristic function is in general not known for non-Gaussian surfaces. We do not intend here to discuss non-Gaussian random surfaces in any detail, since we will not focus on them later. However, we would like to mention that as long as this kind of surfaces can be generated numerically, the scattering problem for non-Gaussian surfaces are not hard to handle by numerical simulations [36–38, 66–68]. On the other hand, small amplitude perturbation theory, say, can not be utilized in its standard form to non-Gaussian surfaces.

2.2 Self-affine surfaces

It has been known for quite some time that self-affine surfaces are abundant in nature. They can be found in various areas of natural science such as surface growth [69–71], fractured surfaces [72], geological structures [73,74], metallurgy [75], and biological systems [76] to mention a few.

A surface, $x_3 = \zeta(x_1)$, is self-affine, according to its definition, between the scales ξ_- and ξ_+, if it remains (either exactly or statistically) invariant in this region under transformations of the form

$$x_1 \to \Lambda x_1, \tag{14a}$$

$$\zeta \to \Lambda^H \zeta, \tag{14b}$$

for all positive real numbers Λ. Here H denotes the *roughness exponent*, also known as the *Hurst exponent*, and it characterizes this invariance. It is usually found in the range from zero to one ($0 < H < 1$). When $H = 1/2$ the surface is an example of the famous random (Brownian) walk where the surface increments are uncorrected. However, if $H \neq 1/2$ the increments are correlated; for $H > 1/2$ the profile is said to be *persistent* (correlated), and for $H < 1/2$ it is *anti-persistent* (anti-correlated). The reason for this naming is that if the self-affine "walker" when moving from the previous to the present space step went up, say, it is more likely that it will go up (down) in the next one if $H > 1/2$ ($H < 1/2$). Over the years numerous methods have been developed for measuring the Hurst exponent from experimental topography data [71,77–79].

The scaling relation 14 is often put in the more compact, but equivalent form

$$\zeta(x_1) \simeq \Lambda^{-H} \zeta(\Lambda x_1), \tag{15}$$

where it has been assumed that $\zeta(0) = 0$ and where $\simeq$ is used to indicate statistical equality. This relation says that if we take the original profile $x_3 = \zeta(x_1)$, enlarge (or contract) the lateral direction by rescaling x_1 into Λx_1, and *simultaneously* scaling ζ to $\Lambda^{-H}\zeta$, the profile $\zeta(x_1)$ and its rescaled version $\Lambda^{-H}\zeta(\Lambda x_1)$ should be indistinguishable. Of course, this holds true in an exact sense only for deterministic surfaces. In the statistical case, however, it is the statistical properties of the profile and its rescaled version that are indistinguishable. In Figs. 5 we presents some examples of self-affine surfaces of Hurst exponent $H = 0.3$ (Fig. 5(a)), $H = 0.5$ (Fig. 5(b)), and $H = 0.7$ (Fig. 5(c)). As can be seen from these figures the landscape becomes more "calm" the larger the Hurst exponent becomes.

The scaling relation Eq. (15) does not fully specify the self-affine surface. In particular no information is contained in Eq. (15) about the amplitude of the surface. Such information is provided by the length scale, ℓ, known as the *topothesy*. This length scale is define as the length, measured along the x_1-direction, over which the rms of the height-difference between two points separated by ℓ is just ℓ. To make this even more clear, let us introduce

$$\sigma(\Delta x_1) = \left\langle \{\zeta(x_1 + \Delta x_1) - \zeta(x_1)\}^2 \right\rangle_{x_1}^{\frac{1}{2}}, \tag{16}$$

as the rms-value of the height-difference measured over a window of size Δx_1. With this definition the topothesy is defined as the length scale for which

$$\sigma(\ell) = \ell. \tag{17}$$

From Eq. (16) it follows immediately that $\sigma(x_1) \sim x_1^H$, so that with Eq. (17) we get

$$\sigma\left(\Delta x_1\right) = \ell^{1-H} \Delta x_1^H. \tag{18}$$

Notice that Eq. (17) allows for a geometrical interpretation of the topothesy as the length scale over which the profile has a mean slope of 45 degrees. The smaller ℓ, the flatter the profile

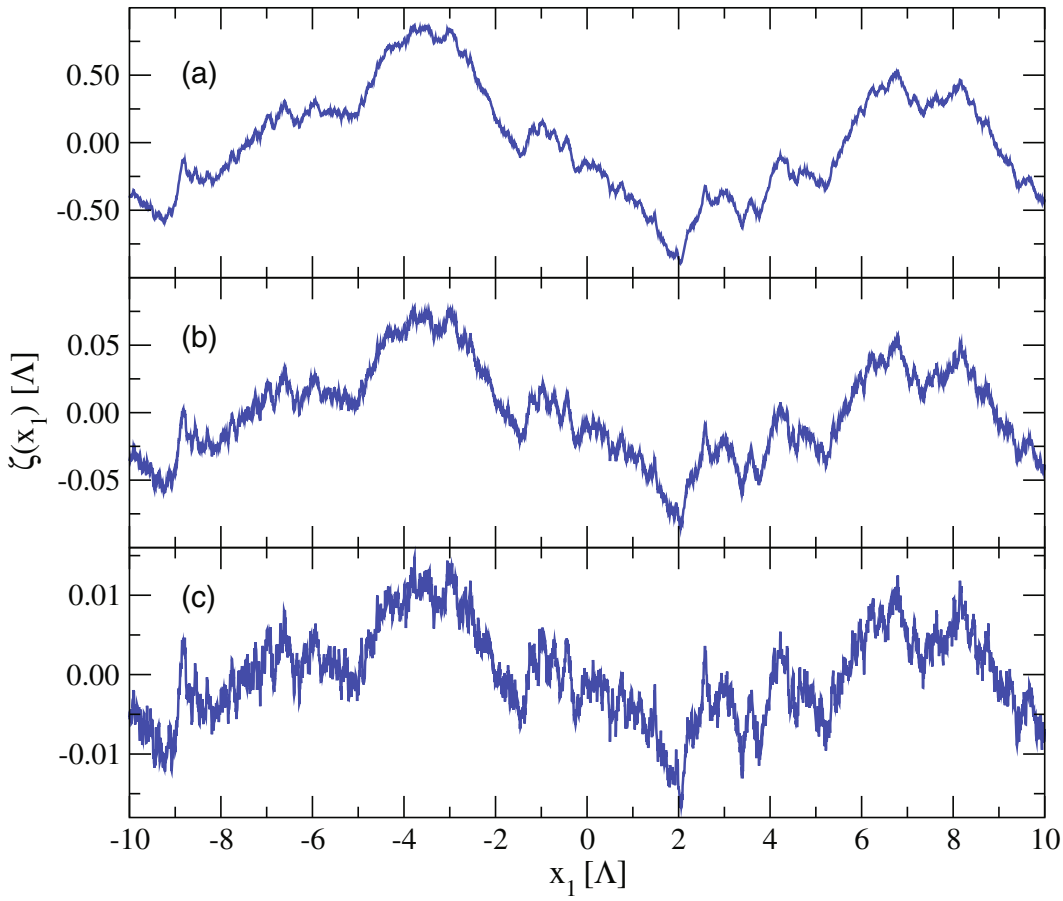

Fig. 5. Examples of self-affine profiles. The Hurst exponents are (a) $H = 0.3$; (b) $H = 0.5$; and (c) $H = 0.7$, where for all cases the topothesy is $\ell = 10^{-3}\,\Lambda$ with Λ an arbitrary length scale (notice the difference in amplitude for the three cases). The surfaces were generated by the Fourier filtering method from the same uncorrelated Gaussian distributed number. Notice how the rms-height of the surface as measured over its total length increases as we increase the Hurst exponent. This is in agreement with Eq. (18).

appears on a macroscopic scale. It should be stressed that in spite of the geometrical interpretation of ℓ, there is nothing a priori that restricts the topothesy to length scales where the self-affinity can be found. However, for the surfaces usually considered in scattering problems, we rather expect that $\ell \ll \xi_-$. When $\xi_- < \ell < \xi_+$, the topothesy makes the transition between the scales, below ℓ, for which a fractal dimension $D = 2 - H$ can be measured using *e.g.* the box counting method [71,77,80,81] and the scales, above ℓ, for which this dimension is just unity. For length scales $\xi_- < \Delta x_1 < \ell$ the fractal dimension is therefore nontrivial (read different from one) and we have an example of a self-affine fractal [71,77,80,81]. It should be noticed that the fractal property of the self-affine surface crucially depends on which length scale the surface is being observed. This essential point seems often to be overlooked in the literature where one too often treat self-affine surfaces as they were fractals [77,81] at any length scale.

Even if the self-affine correlations of the profile is fully characterized by its Hurst exponent H, its topothesy parameter ℓ and the bounds of the self-affine regime ξ_- and ξ_+, nothing is said about its height-distribution. It is therefore not uncommon to talk about for example a Gaussian self-affine surfaces meaning that the surface correlation is of the self-affine type, while the distribution of heights is Gaussian. Thus by specifying the self-affine parameters, *i.e.* H, ℓ, and $\xi_\pm$, in addition to the parameters needed in order to characterize the height-distribution,

the surface is completely specified. Under the assumption that the surface has Gaussian height distribution it can be shown that the probability, $p(\zeta; x_1)$ for finding height ζ at position x_1 given that $\zeta(0) = 0$, can be written as [71]

$$p(\zeta; x_1) = \frac{1}{\sqrt{2\pi}\ell^{1-H}x_1^H} \exp\left[-\frac{1}{2}\left(\frac{\zeta}{\ell^{1-H}x_1^H}\right)^2\right]. \tag{19}$$

However, independent of the height-distribute being Gaussian or not, $p(\zeta; x_1)$ should satisfy the following scaling relation [71,77]

$$p(\zeta; x_1) = \Lambda^H p(\Lambda^H \zeta; \Lambda x_1), \tag{20}$$

which can be derived from the scaling relation Eq. (14).

In fact, the scaling relation 14, or the equivalent form given in Eq. (15), are extremely powerful and can be used to derive many, if not most, of the properties of a self-affine surface. To show an explicit example of this, we would like to derive the scaling relation of the power spectrum of the surface. This scaling relation is the most popular one to use both for generating self-affine surfaces as well as to measure the Hurst exponents (see also Refs. [78,79] for other methods for measuring Hurst exponents). For a surface, $\zeta(x_1)$, of length, L_1, the power spectrum is according to the WienerKhinchin theorem defined as

$$g(|k|) = \frac{1}{L_1}\int_{-\frac{L_1}{2}}^{\frac{L_1}{2}} dx_1\, e^{ikx_1}\langle\zeta(y_1 + x_1)\zeta(y_1)\rangle_{y_1}\,, \tag{21}$$

where $\langle\zeta(y_1 + x_1)\zeta(y_1)\rangle_{y_1}$ is the (two-point) correlation function. By taking advantage of the scaling relations 14 and 15, one finds

$$g\left(\left|\frac{k}{\Lambda}\right|\right) \simeq \frac{1}{\Lambda L_1}\int_{-\frac{\Lambda L_1}{2}}^{\frac{\Lambda L_1}{2}} d(\Lambda x_1)\;\; e^{ikx_1}\left\langle\Lambda^H\zeta(y_1 + x_1)\;\Lambda^H\zeta(y_1)\right\rangle_{y_1}. \tag{22}$$

Hence, one obtains from Eq. (22) that

$$g\left(\left|\frac{k}{\Lambda}\right|\right) \simeq \Lambda^{2H+1} g\left(|k|\right), \tag{23}$$

so that the power spectrum itself has to scale like

$$g\left(|k|\right) \sim k^{-2H-1}. \tag{24}$$

For more details about self-affine surfaces and their properties the reader is referred to the literature [71,77,81].

2.3 Numerical generation of randomly rough surfaces

We have just described how to statistically characterize randomly rough surfaces. In analytical work, this is all what we need. However in a numerical Monte Carlo simulation approaches to be presented in Sec. 4.10, individual surface, called realizations, have to be generated so that they possess the right statistical properties. The question therefore is: How can we do this? We do not intend to give a detailed discussion of this here, but will only sketch how it can be done.

As long as the power spectrum of the surface is known, an efficient way of generating the surface is by using the so-called Fourier filtering method [71,77]. This method essentially consists of two main steps. First, *uncorrelated* random numbers of the type wanted for the height distribution fynction of the surface are generated in real space and thereafter transformed to Fourier space. Second, these numbers are filtered by the square root of the power spectrum $g(|k|)$, and the result transform back to real space by an inverse Fourier transform. After these steps the resulting surface will have the desired height distribution and (height-height) correlation function. It was in this way that the surfaces shown in Figs. 4 and 5 were generated. For additional details the reader is advised to consult Refs. [38,64,66,71,77].

3 Elements of electromagnetic theory

The present review concerns itself mainly with rough surfaces and the scattering of electromagnetic wave from such. In this section, we therefore review some of the basic results of electromagnetic theory, including surface plasmon polaritons (SPPs) [39,43,44,82,83] that are important for the understanding of scattering from weakly randomly rough metal surfaces. The present section also serves to define our notation that will be use extensively in the following sections. The style of this section is kept quite brief, since all the material should be well known. More detailed treatments can be found, for instance, in some of the many excellent and classic texts on electrodynamics [1–7].

3.1 Maxwell's equations and the constitutive equations

3.1.1 Maxwell's equations

The Maxwell's equations – put forward in 1861 by the Scottish physicist James Clerk Maxwell – unified, in one magnificent theory, all electric and magnetic phenomena. They are the fundamental equations of electromagnetism, in the same way that Newton's law is to classical mechanics. In fact, the Maxwell's equations are in a way even more fundamental since they are even consistent with the theory of special relativity that Einstein developed years later. For all these reasons, the Maxwell's equations are among one of the greatest triumphs of natural science and the human mind.

Strictly speaking the equations as put forward by Maxwell only apply to point charges in vacuum. A dielectric, for example, consists of a very huge number of point charges. To deal with them all individually is an impossible task, and it is therefore practical to introduce effective fields, $\mathbf{D}$ and $\mathbf{H}$, in order to represent their collective behavior. This dielectric approach to electromagnetism represents great simplifications. It is based on the following two assumptions [1]: (*i*) the response of the background medium is dipole-like as well as linear in the applied fields, and (*ii*) the medium is (close-to) homogeneous throughout the region of interest. The first assumption obviously breaks down if the fields become too strong while the latter breaks down on short length scales. Hence the resulting effective field theory, or effective Maxwell theory as we might call it, should be treated as a long-wavelength approximation to electromagnetism for weak fields. In most practical situations the above approximations are fortunately well satisfied, and in particular, they are valid for the type of scattering system that we will be considering.

In the SI-system of units, the (effective) Maxwell's equations take on the following form [1–11,43]

$$\nabla \cdot \mathbf{D} = \rho, \tag{25a}$$

$$\nabla \cdot \mathbf{B} = 0, \tag{25b}$$

$$\nabla \times \mathbf{E} = -\frac{\partial \mathbf{B}}{\partial t}, \tag{25c}$$

$$\nabla \times \mathbf{H} = \mathbf{J} + \frac{\partial \mathbf{D}}{\partial t}. \tag{25d}$$

Here $\mathbf{E}$ and $\mathbf{H}$ denote the electric and magnetic field vectors, respectively. These field vectors make together up what is known as the electromagnetic field. The field quantities $\mathbf{D}$ and $\mathbf{B}$, known as the electrical displacement and the magnetic induction (or magnetic flux density), respectively, are included in order to describe the effect of the electromagnetic field on matter. Finally, ρ and $\mathbf{J}$ denote the charge density and the (charge) current density, respectively. Those two latter quantities act like sources for the electromagnetic field, $\mathbf{E}$ and $\mathbf{H}$, and they fulfill the continuity relation

$$\frac{\partial \rho}{\partial t} + \nabla \cdot \mathbf{J} = 0. \tag{26}$$

The various quantities appearing in the Maxwell's equations, and related formulae, are summarized in Table 1 where also their SI-units are given.

Table 1. Summary of the quantities contained in Maxwell's equations, as well as their SI-units.

Quantity	SI-unit	Name
$\mathbf{E}$	V/m	Electric field
$\mathbf{H}$	A/m	Magnetic field
$\mathbf{D}$	C/m^2	Electric displacement
$\mathbf{B}$	Wb/m^2	Magnetic induction
ρ	C/m^3	Charge density
$\mathbf{J}$	A/m^2	Current density

3.1.2 Constitutive equations

The Maxwell's equations (25) consist of eight scalar equations. However, the field vectors, $\mathbf{E}$, $\mathbf{H}$, $\mathbf{D}$, and $\mathbf{B}$, represent in total 12 (scalar) variables, 3 for each of the 4 vectors. Thus, obviously, the Maxwell's equations alone do not uniquely specify a solution. Therefore, in order to obtain a unique solution to the Maxwell's equations, they are supplemented by so-called *constitutive relations* also known as material equations. In their most general form, these relations are complicated, and may show non-linear dependence on the field vectors $\mathbf{E}$ and $\mathbf{H}$ (*i.e.* non-linear electromagnetic theory) [84–86].

Here we will mostly be concerned with linear electromagnetic theory and only briefly touch upon the fascinating field of non-linear optics [1–11,43] (one exception is the non-linear phenomenon to be discussed in Sec. 5.5.1). The linear constitutive relations read [1–11,43]

$$\mathbf{D} = \varepsilon_\circ \varepsilon \mathbf{E}, \tag{27a}$$

$$\mathbf{B} = \mu_\circ \mu \mathbf{H}, \tag{27b}$$

where the constants $\varepsilon_\circ$ and $\mu_\circ$ are the *vacuum permittivity* and *vacuum permeability*, respectively.[3] In the SI-system they are given the following values

$$\varepsilon_\circ = \frac{1}{\mu_\circ c^2} \approx 8.854 \times 10^{-12}\ \mathrm{F/m}, \tag{28a}$$

$$\mu_\circ \equiv 4\pi \times 10^{-7}\ \mathrm{H/m}, \tag{28b}$$

where $c\ (= 1/\sqrt{\varepsilon_\circ \mu_\circ})$ denotes the speed of light in free space ($c = 299,792,458\,\mathrm{m/s}$). Moreover, ε and μ are dimensionless constitutive parameters which are tensors of 2nd order and known as the *relative permittivity* tensor (dielectric function) and the *relative permeability* tensor, respectively. However, for isotropic and homogeneous media these tensors reduce to scalars. We stress that even if it was not said explicitly, the constitutive relations, Eqs. (27), are assumed to be satisfied in Fourier space. In real space, Eqs. (27), should therefore be interpreted as convolutions. Equivalently, Eqs. (27) can be written as [1–11,43]

$$\mathbf{D} = \varepsilon_\circ \mathbf{E} + \mathbf{P}, \tag{29a}$$

$$\mathbf{B} = \mu_\circ \mathbf{H} + \mu_\circ \mathbf{M}, \tag{29b}$$

where $\mathbf{P}$ and $\mathbf{M}$ are the (electric) polarization and magnetization (magnetic polarization), respectively.

[3] Here we have followed Kong [4] and used the somewhat unconventional notation where a circle ($\circ$) is used as the subscripts in $\varepsilon_\circ$ and $\mu_\circ$, instead of the more conventional zero (0). This is done in order to not confuse $\varepsilon_\circ$ with the relative permeability for medium zero that we later will denote by ε_0.

3.2 Electromagnetic wave equation

Probably the two most important consequences of the Maxwell's equations are the *wave equations* and the existence of solutions to these which are known as *electromagnetic waves* due to the wave-like nature. In this section, we derive the wave equations in a material medium. For simplicity, and since it is the most relevant case for this review, we will limit ourselves to a region of space which is source free and isotropic.

The derivation of the wave equations for the **E**-field in a source-free region (*i.e.* $\rho = 0$ and $\mathbf{J} = \mathbf{0}$), is achieved by eliminating the **H**-field from the Maxwell's equations. This is done by taking the curl of Eq. (25c), substituting Eq. (25d), and taking advantage of the constitutive relations 27. The result is (for a non-dispersive medium)

$$\nabla \times (\nabla \times \mathbf{E}) + \frac{\varepsilon\mu}{c^2}\frac{\partial^2 \mathbf{E}}{\partial t^2} = 0. \tag{30}$$

By applying the vector identity $\nabla\times(\nabla\times\mathbf{A}) = \nabla(\nabla\cdot\mathbf{A}) - \nabla^2\mathbf{A}$ to Eq. (30) and taking advantage of Eq. (25a) we obtain the well-known standard (space-time) wave equation for the electrical field in a source-free, homogeneous, isotropic and non-dispersive medium

$$\nabla^2\mathbf{E} - \frac{\varepsilon\mu}{c^2}\frac{\partial^2 \mathbf{E}}{\partial t^2} = 0. \tag{31}$$

In a similar way one can obtain a wave equation for the magnetic field by eliminating the electric field from the Maxwell's equations.

It should be noted that not every solution to the wave equation is also a solution to the Maxwell's equations. A solution to the wave equation must in addition satisfy Gauss's law, $\nabla \cdot \mathbf{E} = \mathbf{k} \cdot \mathbf{E} = 0$ in order to also be a solution of Maxwell's equations[4]. As the reader readily may check, the wave equation has a plane wave solution ($\mathbf{E}_0$ is a constant vector)

$$\mathbf{E} = \mathbf{E}_0 \exp(i\mathbf{k}\cdot\mathbf{x} - i\omega t),$$

if, and only if, the following *dispersion relation* is satisfied

$$|\mathbf{k}|^2 = \varepsilon\mu\,\frac{\omega^2}{c^2}, \tag{32}$$

where $\mathbf{k}$ and ω are the wave vector and the angular frequency associated with the plane wave.

When later considering the scattering from a surface located in, say, the x_1x_2-plane, it will be advantages to decompose the wave vector in a component parallel ($k_\parallel$) and perpendicular ($k_\perp$) to this plane, so that $|\mathbf{k}|^2 = k_\parallel^2 + k_\perp^2$. Inserting this into the dispersion relation, Eq. (32), one arrives at

$$k_\perp^2 = \varepsilon\mu\,\frac{\omega^2}{c^2} - k_\parallel^2, \tag{33}$$

which always has to be satisfied. If $k_\parallel$ is allowed to vary freely along the real axis, the perpendicular component of the wave vector has to be considered a function of $k_\parallel$ and ω; that is, $k_\perp \equiv k_\perp(k_\parallel, \omega)$. For instance, in vacuum, where $\varepsilon\mu = 1$, it follows from Eq. (33) that the perpendicular component of the wave vector becomes purely imaginary whenever $|k_\parallel| > \omega/c$, so the plane wave is exponentially decaying in the x_3-direction, *i.e.* an *evanescent wave*. On the other hand, when $|k_\parallel| < \omega/c$ the plane wave is *propagating* since now $k_\perp$ is real.

3.3 Boundary conditions

In Sec. 3.1 we introduced the Maxwell's equations and the constitutive relations. These equations can be solved for the field vectors in a region of space containing no boundaries. However,

[4] One concrete example of this is provided by $\mathbf{E} = \hat{\mathbf{x}}_3\, E_0 \cos(kx_3 - \omega t)$ that satisfies the wave-equation, but not $\nabla \cdot \mathbf{E} = 0$. It must therefore be discarded as a solution of the Maxwell's equations.

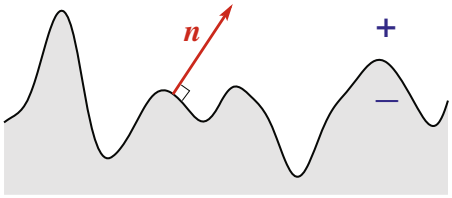

Fig. 6. A sketch of an interface separating two dielectric media. Also the normal vector to the surface, $\mathbf{n}$, is indicated (see Eq. (38b)).

no real medium is infinite, *i.e.* without boundaries. For practical applications of the electromagnetic theory it is therefore important to know how to treat the boundaries between two media of different electromagnetic properties. It is this question that we will address in this section.

Let us consider the geometry of Figure 6. It shows an arbitrary interface separating the otherwise homogeneous, isotropic and linear media labeled $\pm$. We have also introduced a normal vector for the interface, $\mathbf{n}$, which is directed into medium $+$. The question we now address is: How are the electromagnetic field vectors for the two media in the immediate vicinity of the interface related to each other? The answer to this question should be well-known and can be found in nearly any book on electromagnetic theory [1–11]. The results, for which the derivation will not be repeated here, are

$$\hat{\mathbf{n}} \cdot (\mathbf{B}_- - \mathbf{B}_+) = 0, \tag{34a}$$

$$\hat{\mathbf{n}} \cdot (\mathbf{D}_- - \mathbf{D}_+) = \rho_s, \tag{34b}$$

$$\hat{\mathbf{n}} \times (\mathbf{E}_- - \mathbf{E}_+) = 0, \tag{34c}$$

$$\hat{\mathbf{n}} \times (\mathbf{H}_- - \mathbf{H}_+) = \mathbf{J}_s, \tag{34d}$$

where the vector subscripts, $\pm$, are referring to the medium where the field vectors are evaluated. In Eqs. (34) ρ_s and $\mathbf{J}_s$ denote the surface charge density and the surface current density respectively, while the other quantities have been defined previously. In many areas of optics one deals with situations where the surface charge density and the surface current density are zero. Under such circumstances the component of $\mathbf{B}$ and $\mathbf{D}$ that are normal to the surface are continuous, while the vectors $\mathbf{E}$ and $\mathbf{H}$ have continuous tangential components.

It should be stressed that in arriving at the results 34, it has been assumed that the electromagnetic properties take on their bulk values all the way to the surface. This is obviously not true, but is a good approximation whenever the mean field theory applies.

3.3.1 Boundary condition at a general one-dimensional surface

Most of this review will concern itself with randomly rough surfaces that are effectively one-dimensional, *i.e.* the surface profile function $x_3 = \zeta(x_1, x_2)$ has a non-trivial dependence only on x_1, say, and does not depend explicitly on x_2. In this case the boundary conditions 34 simplifies as we now will see.

Let us start by assuming, without loss of generality, that the plane of incidence is the x_1x_3-plane and that the incident light is either p- or s-polarized. In such case, there is only one non-trivial field component needed in order to fully describe the electromagnetic field. For p-polarization this component is H_2, while for s-polarization it is E_2. Thus the primary field for a one-dimensional interface problem can be written as[5]

$$\Phi_\nu(x_1, x_3|\omega) = \begin{cases} H_2(x_1, x_3|\omega), & \nu = p, \\ E_2(x_1, x_3|\omega), & \nu = s, \end{cases} \tag{35}$$

[5] Note that written in this form, the physical dimension of the primary field, $\Phi_\nu(x_1, x_3|\omega)$, depends on polarization as indicated by the subscript ν.

where a harmonic time-dependence, $\exp(-i\omega t)$, has been assumed, but suppressed. This form for the primary field will be used frequently throughout this review. Notice the fact that the primary field can be fully described by a single vector component. This represents a dramatic simplification of the problem since it is reduced from a vector to a scalar problem.

When $\Phi_\nu(x_1, x_3|\omega)$ is known, the remaining components of the electromagnetic field can be calculated from the Maxwell's equations. These components are given for p-polarization as

$$E_1(x_1, x_3|\omega) = -\frac{i}{\omega\varepsilon_\circ\varepsilon(\omega)}\frac{\partial}{\partial x_3}H_2(x_1, x_3|\omega), \tag{36a}$$

$$E_3(x_1, x_3|\omega) = \frac{i}{\omega\varepsilon_\circ\varepsilon(\omega)}\frac{\partial}{\partial x_1}H_2(x_1, x_3|\omega), \tag{36b}$$

and for s-polarization they take the form

$$H_1(x_1, x_3|\omega) = \frac{i}{\omega\mu_\circ\mu(\omega)}\frac{\partial}{\partial x_3}E_2(x_1, x_3|\omega), \tag{37a}$$

$$H_3(x_1, x_3|\omega) = -\frac{i}{\omega\mu_\circ\mu(\omega)}\frac{\partial}{\partial x_1}E_2(x_1, x_3|\omega). \tag{37b}$$

In the above equations, $\varepsilon(\omega)$ and $\mu(\omega)$ denoted the frequency dependent dielectric function and the magnetic permeability, respectively, of the medium where the fields are being evaluated. The relations (36) and (37) are easily derived by using the two curl-equations contained in the Maxwell's equations, Eqs. (25c) and (25d), together with the constitutive relations, Eqs. (27).

Let us now try to focus on the boundary conditions that the primary field $\Phi_\nu(x_1, x_3|\omega)$ will be subjected to. By construction $\Phi_\nu(x_1, x_3|\omega)$ is a field component that is tangential to the surface independent of polarization. Therefore, it follows immediately from Eqs. (34a) and (34d) ($\rho_s = \mathbf{J}_s = 0$) that

$$\Phi_\nu^+(x_1, x_3|\omega)\big|_{x_3=\zeta(x_1)} = \Phi_\nu^-(x_1, x_3|\omega)\big|_{x_3=\zeta(x_1)}, \tag{38a}$$

where $\zeta(x_1)$ denotes the interface separating the two materials of different dielectric properties.

In order to satisfy the remaining boundary conditions expressed in Eqs. (34), we notice that for p- and s-polarization, respectively, we have

$$\hat{\mathbf{n}} \times \mathbf{E} = \hat{\mathbf{x}}_2 \frac{i}{\omega\varepsilon_\circ\varepsilon(\omega)}\partial_n\Phi_p,$$

$$\hat{\mathbf{n}} \times \mathbf{H} = \hat{\mathbf{x}}_2 \frac{i}{\omega\mu_\circ\mu(\omega)}\partial_n\Phi_s,$$

where ∂_n denotes the normal derivative to the surface and $\hat{\mathbf{x}}_2$ is a unit vector in the positive x_2-direction. If the one-dimensional interface can be represented as $x_3 = \zeta(x_1)$, where $\zeta(x_1)$ is a single-valued function of x_1 the normal derivative becomes

$$\partial_n = \hat{\mathbf{n}} \cdot \nabla = \frac{-\zeta'(x_1)\partial_{x_1} + \partial_{x_3}}{\sqrt{1 + (\zeta'(x_1))^2}},$$

where $\partial_{x_i} = \partial/\partial x_i$ and

$$\hat{\mathbf{n}} = \frac{\zeta'(x_1)\hat{\mathbf{x}}_1 + \hat{\mathbf{x}}_3}{\sqrt{1 + (\zeta'(x_1))^2}}. \tag{38b}$$

Here $\hat{\mathbf{x}}_i$ are the standard unit vectors of the underlying Cartesian coordinate system. Hence, the remaining boundary conditions can be expressed as

$$\frac{1}{\kappa_\nu^+(\omega)}\,\partial_n\Phi_\nu^+(x_1, x_3|\omega)\big|_{x_3=\zeta(x_1)} = \frac{1}{\kappa_\nu^-(\omega)}\,\partial_n\Phi_\nu^-(x_1, x_3|\omega)\big|_{x_3=\zeta(x_1)}, \tag{38c}$$

where $\kappa_\nu^\pm(\omega)$ are defined as

$$\kappa_\nu^\pm(\omega) = \begin{cases} \varepsilon_\pm(\omega), & \nu = p \\ \mu_\pm(\omega), & \nu = s \end{cases}. \tag{38d}$$

Equations (38) express the final results for the boundary conditions to be satisfied by the primary field $\Phi_\nu(x_1, x_3|\omega)$ on a one-dimensional interface $x_3 = \zeta(x_1)$.

3.4 Surface plasmon polaritons

In subsequent sections, we will see that so-called surface plasmon polaritons (SPPs) will play an important role for the rough surface scattering problem. We will therefore in this section define and discuss some of their characteristic properties [33,39,43,44,82,83].

Before starting our discussion, we have to know what a polariton is: According to its classical definition a polariton is defined to be an elementary electromagnetic wave, and therefore a solution of the Maxwell's equations, that may couple to one of several possible excitations possible in a condensed medium. Examples of such excitations are plasmons, phonons, mognons etc., and in such cases one talks of plasmon polaritons, phonon polaritons and magnon polaritons. With the notion of polariton established, one might definition an SPP as follows: *A surface plasmon polariton is a plasmon polariton where the associated electromagnetic field is confined to the surface separating two dielectric media.*

3.4.1 SPPs on a plan surface geometry

To see under what conditions SPPs might exist, and to discuss some of their properties, we will consider a planar interface separating two isotropic and homogeneous media [39,43,44,82,83]. For simplicity, the coordinate system will be chosen so that the interface is located at $x_3 = 0$. The materials above ($x_3 > 0$) and below ($x_3 < 0$) this surface will be characterized by frequency dependent dielectric functions $\varepsilon_+(\omega)$ and $\varepsilon_-(\omega)$, respectively. For simplicity we will assume that the imaginary parts of the dielectric functions can be neglected. However, this assumption is not essential, and the conclusion that we will arrive at is independent of this assumption. Furthermore, we will assume either p- or s-polarized incident light. Hence, the scalar wave equation might be used. A more complete discussion using vector fields can be found in Refs. [39,82,83].

According to the definition of SPP [39,43,44,82,83], we are interested in solutions to the Maxwell's equations, equivalent in our case to the scalar wave equation, that are wave-like parallel to the surface $x_3 = 0$ and that decays exponentially with increasing distance from the surface into each of the two media. Such a solution can be represented mathematically as [39]

$$\Phi_\nu^\pm(x_1, x_3|\omega) = \mathcal{A}_\nu^\pm \, e^{\mp\beta_\pm(\omega)x_3} \, e^{ikx_1}, \qquad \nu = p, s, \tag{39}$$

where $\mathcal{A}_\nu^\pm$ represent the amplitudes (to be determined). The decay constants $\beta_\pm(\omega)$ are defined as

$$\beta_\pm(\omega) = \sqrt{k^2 - \varepsilon_\pm(\omega)\frac{\omega^2}{c^2}}, \tag{40}$$

and they must be real and positive for Eq. (39) to describe an electromagnetic wave localized to the surface[6]. To investigate if Eq. (39) is an acceptable solution for our scattering system, we have to impose the boundary conditions, given in Eqs. (38), for the two polarizations. By utilizing the continuity of the fields on the flat surface, Eq. (38a), one finds that

$$\mathcal{A}_\nu^+ = \mathcal{A}_\nu^- \equiv \mathcal{A}_\nu,$$

[6] If we had allowed the dielectric functions of the problem to be complex with $Im\,\varepsilon_\pm(\omega) > 0$, we would have to require that $Re\,\beta_\pm(\omega) > 0$.

for all locations along the surface. Moreover, the normal derivative condition, Eq. (38c), gives the following condition for the existence of SPPs on a flat surface ($\partial_n = \partial_{x_3}$)

$$\left[\frac{\beta_+(\omega)}{\kappa_\nu^+(\omega)} + \frac{\beta_-(\omega)}{\kappa_\nu^-(\omega)}\right] \mathcal{A}_\nu = 0, \tag{41}$$

where we recall the definitions of $\kappa_\nu^\pm(\omega)$ from Eq. (38d). The most immediate consequence of this relation is that for s-polarization, since $\kappa_s^\pm(\omega) = 1$ (for non-magnetic materials) and $\beta_\pm(\omega)$ are assumed to be real and *positive*, the only solution to Eq. (41) is $\mathcal{A}_s \equiv 0$. Thus, a s-polarized surface plasmon polariton (surface wave) *cannot* exist.

However, for p-polarized light, where $\kappa_p^\pm(\omega) = \varepsilon_\pm(\omega)$, a non-trivial solutions might exist when ($\mathcal{A}_p \neq 0$)

$$\frac{\varepsilon_+(\omega)}{\varepsilon_-(\omega)} = -\frac{\beta_+(\omega)}{\beta_-(\omega)}. \tag{42}$$

Equation (42) is the dispersion relation for SPPs on a flat interface (if they exist). For this relation to be satisfied, the dielectric functions of the two media involved, have to have different signs due to the presence of the negative sign on the right-hand-side of Eq. (42) and that $\beta_\pm(\omega)$ both are (assumed to be) positive. Only such combination of materials will support SPPs. An important example of such a system at optical frequencies, is a metal with a planar interface to vacuum.

By squaring both sides of Eq. (42) and taking advantage of Eq. (40), the dispersion relation can be expressed as [39]

$$k_{spp}(\omega) = \sqrt{\frac{\varepsilon_+(\omega)\varepsilon_-(\omega)}{\varepsilon_+(\omega) + \varepsilon_-(\omega)}}\frac{\omega}{c}. \tag{43}$$

This equation gives an explicit expression for the wavenumber of the surface plasmon polariton. However, this formulae should be used with some care since it may, from the way it is derived from Eq. (42), introduce some spurious solutions. The additional and sufficient requirement that have to be satisfied is that $\beta_\pm(\omega)$ are positive while the two dielectric functions, $\varepsilon_\pm(\omega)$, have different sign.

We also note that the $1/e$ decay length of an SPP propagating along a surface is given in terms of the imaginary part of its wavenumber as

$$\ell_{spp}(\omega) = \frac{1}{2\,\mathrm{Im}\,k_{spp}(\omega)}. \tag{44}$$

3.4.2 SPPs at a planar free electron metal surface

As an illustration let us consider a free electron metal with a planar interface to vacuum. For such a metal the dielectric function is known to be [87,88]

$$\varepsilon_-(\omega) = \varepsilon_\infty(\omega)\left(1 - \frac{\omega_p^2}{\omega^2}\right), \tag{45}$$

and for vacuum one has $\varepsilon_+(\omega) = 1$. In the above equation $\varepsilon_\infty(\omega)$ is the background dielectric constant of the material while ω_p is the electronic plasma frequency. With Eq. (45) the frequency of the SPP can be shown to be

$$\omega_{spp}(k) = \left[\frac{1}{2}\left(\frac{k^2c^2}{\varepsilon_\infty(\omega)}\left(1+\varepsilon_\infty(\omega)\right) + \omega_p^2\right) - \frac{1}{2}\sqrt{\left(\frac{k^2c^2}{\varepsilon_\infty(\omega)}\left(1+\varepsilon_\infty(\omega)\right) + \omega_p^2\right)^2 - 4k^2c^2\omega_p^2}\,\right]^{\frac{1}{2}}. \tag{46}$$

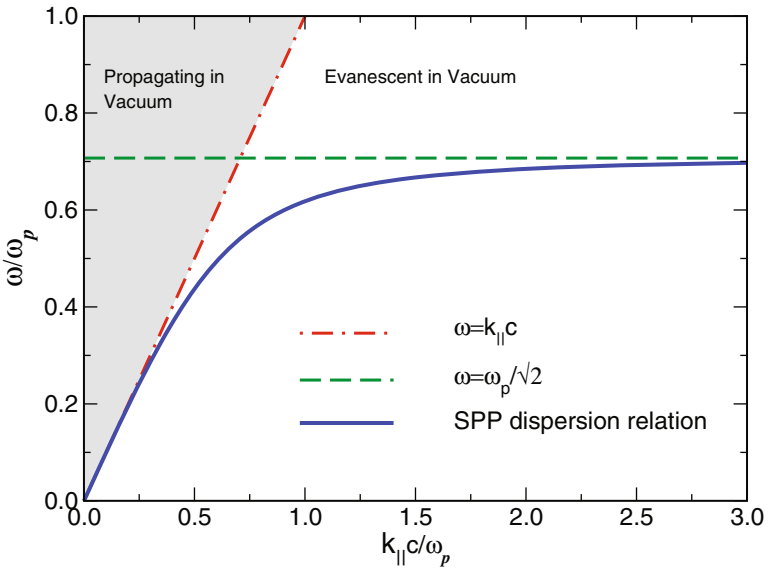

Fig. 7. Dispersion relation curve, Eq. (46), for a surface plasmon polariton (solid line) at a flat interface between a simple metal and vacuum (assuming $\varepsilon_\infty(\omega) = 1$). The dash-dotted line represents the light line $\omega = kc$, while the dashed line is the large momentum asymptotic limit, $\omega_{sp} = \omega_p/\sqrt{2}$, of the SPP dispersion curve (see Eq. (47)).

It should be noticed from this equation that

$$\omega_{spp}(k) = \begin{cases} kc, & k \to 0, \\ \sqrt{\dfrac{\varepsilon_\infty(\omega)}{\varepsilon_\infty(\omega)+1}}\,\omega_p, & k \to \infty, \end{cases} . \tag{47}$$

This means that in the small wave vector limit the SPP is *photon-like*, while in the large wave vector limit it is *plasmon-like*. In Fig. 7 the dispersion relation, Eq. (46), for a free electron metal is depicted. In this figure we have also included the light-line (dash-dotted line) $\omega = kc$, as well as the large wave vector limit (dashed line) of $\omega_{spp}(k)$.

From Fig. 7 we see that the dispersion curve for the SPP lies entirely to the right of the light-line, $\omega = kc$. The physical consequence of this is that there is no coupling between the surface plasmon polariton and light in vacuum for a flat vacuum-metal interface. Or put another way, light incident onto a planar vacuum-metal interface cannot excite surface plasmon polaritons. Later, however, we will see that if the surface is rough such coupling is possible (and other ways are outlined in Ref. [39]). This will give rise to many new and interesting multiple-scattering effects, as we discuss in some detail in Sec. 5.

4 Quantities and techniques used in the study of rough surface scattering

The intention of the present section is to introduce some of the quantities and techniques, both analytical and numerical, used in the study of wave scattering from randomly rough surfaces. In the first part of this section, we address some general properties of the scattering problem, while the second part is devoted to some of the central theoretical approaches used in solving it. In this section the outlined theories will not be applied to specific scattering problem, since this will partly be the focus of the following section.

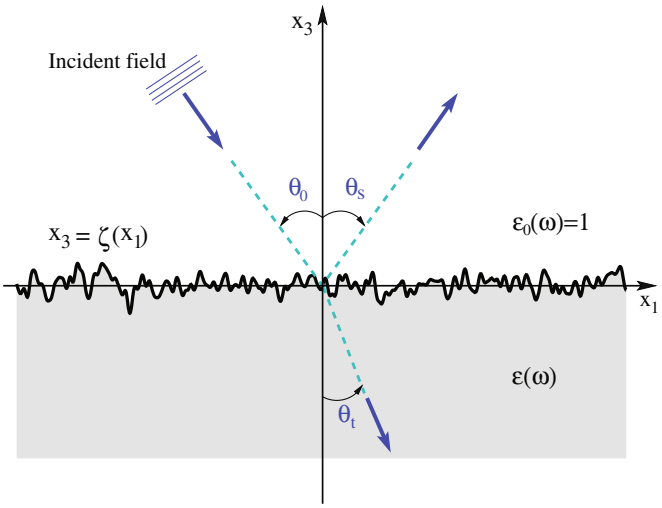

Fig. 8. The main scattering geometry used throughout this section for the wave scattering from a rough surface defined by $x_3 = \zeta(x_1)$. The region above the surface, $x_3 > \zeta(x_1)$, is assumed to be vacuum ($\varepsilon_+(\omega) = \varepsilon_0(\omega) = 1$), while the medium below the surface is a metal or dielectric and characterized by a frequency-dependent dielectric function $\varepsilon_-(\omega) = \varepsilon(\omega)$. Notice for what directions the angles of incident, θ_0; scattering, θ_s; and transmission, θ_t are defined positive. Moreover, an angle of transmission is only well-defined if the lower medium is transparent, *i.e.* if $Re\,\varepsilon(\omega) > 0$ (and $Im\,\varepsilon(\omega) \approx 0$).

4.1 Scattering geometry

The scattering geometry that we will mainly concern ourselves with in this section is depicted in Fig. 8. It consists of vacuum ($\varepsilon_+(\omega) = \varepsilon_0(\omega) = 1$) in the region $x_3 > \zeta(x_1)$, and a metal or dielectric characterized by an isotropic, frequency-dependent, dielectric function $\varepsilon_-(\omega) = \varepsilon(\omega)$, in the region $x_3 < \zeta(x_1)$. Here $\zeta(x_1)$ denotes the surface profile function and it is assumed to be a single-valued function of x_1 that is differentiable as many times as is necessary. Furthermore, it constitutes a zero mean, stationary, Gaussian random process which we from Sec. 2.1 recall is defined by

$$\langle \zeta(x_1) \rangle = 0, \tag{48a}$$

$$\langle \zeta(x_1)\zeta(x_1') \rangle = \delta^2 W(|x_1 - x_1'|). \tag{48b}$$

Here $W(|x_1|)$ denotes the auto-correlation function and it will be specified later.

The incident wave will be either p- or s-polarized and the plane of incidence is assumed to be the x_1x_3-plane. Furthermore, the angle of incidence, reflection, and transmission, θ_0, θ_s, and θ_t, respectively, are measured positive according to the convention given in Fig. 8.

4.2 Scattered field

From Sec. 3 we recall that in order to solve the scattering problem, we have to solve the Helmholtz equation and satisfy the boundary conditions at the rough interface $x_3 = \zeta(x_1)$, Eqs. (38), as well as at infinity. In the present section, we will give the form of the far fields that automatically satisfy the Helmholtz equation and the boundary conditions at infinity. We will discuss separately the case where the incident field is a plane wave and a finite sized beam.

However, before we do so, we recall that for the scattering geometry depicted in Fig. 8, the Maxwell's equations are equivalent to the scalar Helmholtz equation for the field $\Phi_\nu(x_1, x_3|\omega)$ defined by Eq. (35), *i.e.*

$$\Phi_\nu(x_1, x_3|\omega) = \begin{cases} H_2(x_1, x_3|\omega), & \nu = p, \\ E_2(x_1, x_3|, \omega), & \nu = s, \end{cases} . \tag{49}$$

It is the asymptotic, far-field behavior of $\Phi_\nu(x_1, x_3|\omega)$ that we are trying to determine.

4.2.1 Plane incident wave

Let us first consider the situation where the incident field is an either p- or s-polarized plane wave that can be written in the form[7]

$$\Phi_\nu^{inc}(x_1, x_3|\omega) = e^{ikx_1 - i\alpha_0(k,\omega)x_3}, \tag{50}$$

where k denotes the lateral component of the wave vector and $\alpha_0(k,\omega)$ its perpendicular component defined as[8]

$$\alpha_0(q,\omega) \equiv \alpha_+(q,\omega) = \begin{cases} \sqrt{\frac{\omega^2}{c^2} - q^2}, & |q| < \frac{\omega}{c}, \\ i\sqrt{q^2 - \frac{\omega^2}{c^2}}, & |q| > \frac{\omega}{c}. \end{cases} \tag{51}$$

Note, that the plane wave, Eq. (50), is propagating *downward* (in the direction of negative x_3) due to the negative sign of the last term in the argument to the exponential function. If this sign instead had been positive, the plane wave would have been propagating *upward*.

In passing, we make a comment on the customary notation used in writing Eqs. (50) and (51), since it might be a bit confusing at first. In Sec. 3.2 the parallel and perpendicular components of the wave vector, $\mathbf{k}$, were called, $k_\parallel$ and $k_\perp$, respectively. The notation introduced in Eqs. (50) and (51), and that will be used extensively throughout this review, is so that $k_\parallel \equiv k$ and $k_\perp \equiv \alpha_0(k,\omega)$ where the definition of $\alpha_0(k,\omega)$ follows from Eq. (33) (in vacuum). The reader should be aware, something that is an unfortunate side effect of this notation, that k is *not* the same as $|\mathbf{k}|$. Instead one has that $|\mathbf{k}|^2 = k^2 + \alpha_0^2(k,\omega)$.

With Eq. (50) the form of the field in region $x_3 > \max\zeta(x_1)$ that satisfied both the Helmholtz equation and the boundary condition at infinity ($x_3 = \infty$) can be written as

$$\Phi_\nu^+(x_1, x_3|\omega) = \Phi_\nu^{inc}(x_1, x_3|\omega) + \int_{-\infty}^{\infty} \frac{dq}{2\pi}\, R_\nu(q|k) e^{iqx_1 + i\alpha_0(q,\omega)x_3}, \tag{52a}$$

where the second term corresponds to the scattered field and $R_\nu(q|k)$ are unknown scattering (or reflection) amplitudes (from lateral wave numbers k to q) to be determined. Note that for the scattered field, the integration over the lateral component of the scattered wave vector, q, extends over the whole real axis so that both propagating and evanescent contributions are included for the scattered field(*c.f.* Sec. 3.2).

Similarly, a solution of the Helmholtz equation in the region $x_3 < \min\zeta(x_1)$ that satisfy the boundary condition at $x_3 = -\infty$ is

$$\Phi_\nu^-(x_1, x_3|\omega) = \int_{-\infty}^{\infty} \frac{dq}{2\pi}\, T_\nu(q|k) e^{iqx_1 - i\alpha(q,\omega)x_3}, \tag{52b}$$

where $T_\nu(q|k)$ denotes the transmission amplitude and the perpendicular component of the transmitted wave vector is defined as where ($\varepsilon_-(\omega) \equiv \varepsilon(\omega)$)

$$\alpha(q,\omega) \equiv \alpha_-(q,\omega) \;=\; \sqrt{\varepsilon(\omega)\frac{\omega^2}{c^2} - q^2}, \qquad Re\,\alpha, Im\,\alpha > 0. \tag{53}$$

Notice that these asymptotic expressions do note determine the field in the surface region $\min\zeta(x_1) < x_3 < \max\zeta(x_1)$. This and its consequence, will be discussed in more detail in Sec. 4.5 when we derive the so-called reduced Rayleigh equation.

[7] It should be noted that in writing Eq. (50) we have suppressed a non-dimension-less constant amplitude in order to simplifying the following mathematical expressions (see *e.g.* Ref. [89]). However, the expressions for the physical observable to be discussed later in this section are independent of this choice since such amplitudes cancel in these expressions.

[8] We will use the notation $\alpha_0(q,\omega)$ instead of $\alpha_+(q,\omega)$ in order to follow the notation frequently used in the literature.

4.2.2 Finite width incident wave

If the incident field is not a plane wave, but instead has a finite width, then the above expressions will have to be changed somewhat. In this case the incident field can be written as

$$\Phi_\nu^{inc}(x_1, x_3|\omega) = \int_{-\frac{\omega}{c}}^{\frac{\omega}{c}} \frac{dk}{2\pi} F(k) e^{ikx_1 - i\alpha_0(k,\omega)x_3}, \tag{54a}$$

i.e. as a weighted sum of plane waves. Here $F(k)$ is in principle an arbitrary function for which the integral exits. Due to the linearity of the Maxwell's equations, the scattered field becomes

$$\Phi_\nu^{sc}(x_1, x_3|\omega) = \int_{-\infty}^{\infty} \frac{dq}{2\pi} R_\nu(q,\omega) e^{iqx_1 + i\alpha_0(q,\omega)x_3}, \tag{54b}$$

where

$$R_\nu(q,\omega) = \int_{-\frac{\omega}{c}}^{\frac{\omega}{c}} \frac{dk}{2\pi} R_\nu(q|k) F(k). \tag{54c}$$

The total field in the region $x_3 > \max \zeta(x_1)$ is $\Phi_\nu^+(x_1, x_3|\omega) = \Phi_\nu^{inc}(x_1, x_3|\omega) + \Phi_\nu^{sc}(x_1, x_3|\omega)$.

In a similar way the field in the region $x_3 < \min \zeta(x_1)$ can be written as

$$\Phi_\nu^-(x_1, x_3|\omega) = \int_{-\infty}^{\infty} \frac{dq}{2\pi} T_\nu(q,\omega) e^{iqx_1 - i\alpha(q,\omega)x_3}, \tag{55}$$

where $T_\nu(q,\omega)$ is given by an expression similar to Eq. (54c).

In order to fully define the asymptotic forms of the field, the envelope $F(k)$ has to be given. Here we will only consider so-called Gaussian finite beams. Such beams are obtained if $F(k)$ has the Gaussian form. If the half-width of the incident beam is denoted by w, the Gaussian envelope $F(k)$ can be written as [66]

$$F(k) = \frac{w}{2\sqrt{\pi}} \frac{\omega}{c} \frac{1}{\alpha_0(k,\omega)} \exp\left[-\frac{w^2\omega^2}{4c^2} \left(\arcsin\frac{kc}{\omega} - \theta_0 \right)^2 \right]. \tag{56}$$

4.3 Mean differential reflection coefficient

In the previous section, we obtained the asymptotic forms of the scattered and transmitted fields. These fields are known whenever the scattering and transmission amplitudes, $R_\nu(q|k)$ and $T_\nu(q|k)$, are known. We will later in this section describe methods for how to determine these amplitudes.

However, these two amplitudes are not directly accessible in experiments. Since our ultimate goal is to compare the theoretical predictions to those of experimental measurements, one has to relate these amplitudes to measurable quantities. Such quantities are provided by, for instance, the so-called mean differential reflection and transmission coefficients [38,66]. These are not the only experimentally accessible quantities possible. However, other such quantities must necessarily be related to the reflection or transmission amplitudes, since they fully specify the scattering and transmission problem.

The mean differential reflection coefficient[9] is defined as the fraction of the total incident power scattered, by the randomly rough surface, into an angular interval of width $d\theta_s$ about

[9] If the surface is two-dimensional, as will be assumed in Sec. 5.6, one has to consider scattering into solid angle $d\Omega_s$ around the scattering direction (θ_s, ϕ_s) instead of into the angular interval $d\theta_s$ around the scattering angle θ_s as is the case if the surface is one-dimensional. Furthermore, one also has to take into account that depolarization may occur in scattering from two-dimensional surfaces. Hence the mean differential reflection and transmission coefficients in the $2D$-case have polarization indices referring to the polarization of the incident and scattered light respectively. See Sec. 5.6 for additional details.

the scattering angle θ_s. Thus, in order to obtain an expression for this quantity one has to find an expression for the power incident onto the rough surface and the power scattered from it. We recall that the total power contained in an electromagnetic wave of electric and magnetic field vectors $\mathbf{E}$ and $\mathbf{H}$, respectively, is given by the real part of the complex Poynting vector $\mathbf{S} = \mathbf{E} \times \mathbf{H}^*$, where the asterisk denotes complex conjugate. More useful to us is the time-averaged of this (complex) quantity that is given by [1,2,4–6,9]

$$\langle \mathbf{S} \rangle_t = \frac{1}{2} \mathbf{E} \times \mathbf{H}^*, \tag{57}$$

where $\langle \cdot \rangle_t$ indicates time average. Hence the time-averaged power incident on the rough surface, and scattered from it, are given by the real part of the 3-component of $\langle \mathbf{S} \rangle_t$, evaluated for the fields involved. The corresponding time-averaged total energy flux therefore becomes[10]

$$P = \int dx_1 dx_2 \; Re \langle \mathbf{S}_3 \rangle_t = L_2 \int dx_1 \; Re \langle \mathbf{S}_3 \rangle_t . \tag{58}$$

In writing the above equation we have taken advantage of the fact that for a one-dimensional rough surface with its generator along the x_1-direction (as we consider here), the x_2-integration becomes trivial and only contributes with a factor L_2, the length of the surface in the x_2-direction.

4.3.1 Plane incident wave

We recall that if the incident wave is a plane wave of the form given in Eq. (50), then the scattered field is given by the second term of Eq. (52a). The incident and scattered power thus become

$$P_{inc} = \frac{L_1 L_2}{2} \frac{c^2}{\omega} \alpha_0(k, \omega), \tag{59a}$$

and

$$\begin{aligned} P_{sc} &= \frac{L_2}{2} \frac{c^2}{\omega} \int_{-\frac{\omega}{c}}^{\frac{\omega}{c}} \frac{dq}{2\pi} \; \alpha_0(q, \omega) \left| R_\nu(q|k) \right|^2 , \\ &= \int_{-\frac{\pi}{2}}^{\frac{\pi}{2}} d\theta_s \; p_{sc}(\theta_s), \end{aligned} \tag{59b}$$

where

$$p_{sc}(\theta_s) = \frac{L_2}{4\pi} \omega \cos^2 \theta_s \left| R_\nu(q|k) \right|^2 . \tag{59c}$$

Hence, the differential reflection coefficient, according to its definition, is given by the following expression

$$\frac{\partial R_\nu}{\partial \theta_s} = \frac{p_{sc}(\theta_s)}{P_{inc}} = \frac{1}{L_1} \frac{\omega}{2\pi c} \frac{\cos^2 \theta_s}{\cos \theta_0} \left| R_\nu(q|k) \right|^2 .$$

Here it is to be understood that the lateral wave numbers k and q are related to the angles θ_0 and θ_s according to

$$k = \frac{\omega}{c} \sin \theta_0, \tag{60a}$$

$$q = \frac{\omega}{c} \sin \theta_s. \tag{60b}$$

Notice that $\partial R_\nu / \partial \theta_s$ includes the contribution from only one single realization of the rough surface. However, we are more interested in the mean of this quantity obtained by making an

[10] Recall that the coordinate system is chosen so that the x_1x_2-plane coincides with the average (planar) surface, and thet the incident plane is the x_1x_3-plane.

average over an ensemble of realizations of the rough surface profile. In consequence we obtain the following expression for the *mean differential reflection coefficient* (DRC)

$$\left\langle \frac{\partial R_\nu}{\partial \theta_s} \right\rangle = \frac{1}{L_1} \frac{\omega}{2\pi c} \frac{\cos^2 \theta_s}{\cos \theta_0} \left\langle |R_\nu(q|k)|^2 \right\rangle . \tag{61}$$

When light is scattered from a randomly rough surface both coherent (specular) and incoherent (diffuse) scattering processes will normally occur. The scattered power due to both these processes are contained in Eq. (61). In theoretical studies of wave scattering from rough surfaces it has proven useful to separate these two contributions even though such separation is not possible under experimental conditions. The separation is done by noticing that $\langle |R_\nu(q|k)|^2 \rangle$ can trivially be written as

$$\left\langle |R_\nu(q|k)|^2 \right\rangle = \left\langle |R_\nu(q|k)|^2 \right\rangle - |\langle R_\nu(q|k) \rangle|^2 + |\langle R_\nu(q|k) \rangle|^2 . \tag{62}$$

Here the last term (on the right hand side) corresponds to the coherently scattered light, while the first two terms are related to the light scattered incoherently. By using this result we find that the mean DRC can be divided into a coherent and an incoherent part, and they are respectively given by

$$\left\langle \frac{\partial R_\nu}{\partial \theta_s} \right\rangle_{\text{coh}} = \frac{1}{L_1} \frac{\omega}{2\pi c} \frac{\cos^2 \theta_s}{\cos \theta_0} |\langle R_\nu(q|k) \rangle|^2 , \tag{63a}$$

and

$$\left\langle \frac{\partial R_\nu}{\partial \theta_s} \right\rangle_{\text{incoh}} = \frac{1}{L_1} \frac{\omega}{2\pi c} \frac{\cos^2 \theta_s}{\cos \theta_0} \left[\left\langle |R_\nu(q|k)|^2 \right\rangle - |\langle R_\nu(q|k) \rangle|^2 \right] . \tag{63b}$$

Expressions for the *mean differential transmission coefficient*, $\langle \partial T_\nu / \partial \theta_s \rangle = \langle p_{tr}(\theta_t)/P_{inc} \rangle$, can be obtained in an analogous way by calculating $p_{tr}(\theta_t)$, the equivalent of $p_{sc}(\theta_s)$ in transmission. The results of such a calculation is that the expressions for $\langle \partial T_\nu / \partial \theta_s \rangle$ can be obtained from those of $\langle \partial R_\nu / \partial \theta_s \rangle$ by substituting the transmission amplitude $T_\nu(q|k)$ for the reflection amplitude, $R_\nu(q|k)$ and multiplying the final expression with a factor of $\sqrt{\varepsilon(\omega)}$ [38,180].

4.3.2 Finite width incident beam

In the previous subsection we considered a plane incident wave. Such waves can never be fully realized under experimental conditions, and it is therefore desirable under some circumstances to work with an incident beam of finite width.

A finite sized beam was already introduced in Subsec. 4.2.2 and with those expressions one gets for the incident and scattered power

$$P_{inc} = L_2 \frac{wc}{2\sqrt{2\pi}} \left[\text{erf}\left(\frac{w}{\sqrt{2}} \frac{\omega}{c} \left(\frac{\pi}{2} - \theta_0 \right) \right) + \text{erf}\left(\frac{w}{\sqrt{2}} \frac{\omega}{c} \left(\frac{\pi}{2} + \theta_0 \right) \right) \right] , \tag{64a}$$

where $\text{erf}(x)$ is the error-function [90], and

$$p_{sc}(\theta_s) = L_2 \frac{\omega}{2\pi^2} \cos^2 \theta_s \, |R_\nu(q|k)|^2 . \tag{64b}$$

Hence, the differential reflection coefficient, according to its definition, is given by the expression

$$\left\langle \frac{\partial R_\nu}{\partial \theta_s} \right\rangle = \frac{2}{(2\pi)^{\frac{3}{2}}} \frac{\omega}{cw} \cos^2 \theta_s \frac{\left\langle |R_\nu(q,\omega)|^2 \right\rangle}{\frac{1}{2}\left[\text{erf}\left(\frac{w\omega}{\sqrt{2}c} \left(\frac{\pi}{2} + \theta_0 \right) \right) + \text{erf}\left(\frac{w\omega}{\sqrt{2}c} \left(\frac{\pi}{2} - \theta_0 \right) \right) \right]} . \tag{65}$$

Also here lateral wave number, q, is understood to be related to the scattering angle *via* Eq. (60b). The coherent and incoherent contributions to the mean differential reflection coefficient are obtained in a completely analogous way as to how they were obtained for plane wave illumination.

4.4 General properties of the scattering problem

In order to solve the scattering problem, we have to calculate the scattering and transmission amplitudes, $R_\nu(q|k)$ and $T_\nu(q|k)$. However, before we start discussing various methods for doing so, we will introduce some general features that the scattering problem should fulfill. These properties are, among others, *reciprocity* and *unitarity*.

4.4.1 Reciprocity

A general property of the scattering problem is reciprocity. It involves the scattering matrix, $S_\nu(q|k)$, defined via the scattering amplitude according to

$$S_\nu(q|k) = \frac{\sqrt{\alpha_0(q,\omega)}}{\sqrt{\alpha_0(k,\omega)}} R_\nu(q|k). \tag{66}$$

The reciprocity theorem states that the scattering matrix, or just S-matrix for short, should satisfy the following relation

$$S_\nu(q|k) = S_\nu(-k|-q). \tag{67}$$

For the surface scattering problem, this relation can under rather general assumptions be derived rigorously from Lorentz's reciprocity theorem [30,91–93]. However, we will not present such an interesting, but lengthy derivation here. We would, however, like to point out that such a derivation does not assume anything about the dielectric functions involved. Furthermore, there is no restriction on how strongly rough the surface is, neither how it is correlated. Hence, the reciprocity theorem is generally valid. It should also be pointed out that there seems to be no equivalent theorem to Eq. (67) that involves the transmission amplitude $T_\nu(q|k)$. Reciprocity is therefore a property of the scattering matrix.

4.4.2 Unitarity

In cases where the scattering medium is a perfect reflector, *i.e.* if $\mathrm{Re}\,\varepsilon(\omega) < 0$ and $\mathrm{Im}\,\varepsilon(\omega) = 0$, the scattering matrix, $S_\nu(q|k)$, possess an additional property call *unitarity*. Since there is no absorption ($\mathrm{Im}\,\varepsilon(\omega) = 0$) and no transmission in the system, the energy incident on the rough, perfectly reflecting surface must be all scattered. Without going into details, this has the consequence that the following relation has to be satisfied [30]

$$\int_{-\frac{\omega}{c}}^{\frac{\omega}{c}} \frac{dq}{2\pi} S_\nu(q|k) S_\nu^*(q|k') = 2\pi\delta(k-k'), \qquad |k|, |k'| < \frac{\omega}{c}. \tag{68}$$

It can be derived by calculating the total energy flux scattered from the surface that, due to energy conservation, should equal the incident energy flux. Eq. (68) expresses the unitarity of the scattering matrix, and it is a consequence of the conservation of energy in the scattering process.

Even if Eq. (68) is derived under the assumption that energy conservation is satisfied, let us for a moment show how this indeed follows from the unitarity condition. Let us assume that the rough surface has length L_1. Then we know from the sampling theorem [94] that the smallest momentum variable that we can resolve is $2\pi/L_1$. By multiplying each side of Eq. (68) by $dk'/(2\pi)$ and integrating the resulting expression over an interval of length $2\pi/L_1$ that contains $k' = k$ one finds

$$\frac{1}{L_1} \int_{-\frac{\omega}{c}}^{\frac{\omega}{c}} \frac{dq}{2\pi} \left|S_\nu(q|k)\right|^2 = 1. \tag{69}$$

By using the definition of the scattering matrix, Eq. (66), together with Eq. (60b), one arrives at

$$\int_{-\pi/2}^{\pi/2} \left\langle \frac{\partial R_\nu}{\partial \theta_s} \right\rangle \, d\theta_s = 1, \tag{70}$$

where we have taken advantage of Eq. (61). From the definition of the mean differential reflection coefficient given in Sec. 4.3.1, we understand that Eq. (70) is just the conservation of energy for the scattering system considered.

4.4.3 Energy conservation

If, however, the lower medium is *not* a perfect reflector, but still is a non-absorbing medium ($\operatorname{Im}\varepsilon(\omega) = 0$) the unitarity condition Eq. (68) will no longer hold true. However, we should still have conservation of energy. This means that all energy incident onto the rough surface should be either scattered from it or transmitted trough it. This fact is expressed by the following equation

$$\mathcal{U}_\nu^{\mathrm{sc}}(\theta_0, \omega) + \mathcal{U}_\nu^{\mathrm{tr}}(\theta_0, \omega) = 1, \tag{71}$$

where θ_0 is the angle of incidence of the light, and

$$\mathcal{U}_\nu^{\mathrm{sc}}(\theta_0, \omega) = \int_{-\pi/2}^{\pi/2} \left\langle \frac{\partial R_\nu}{\partial \theta_s} \right\rangle \, d\theta_s, \tag{72a}$$

$$\mathcal{U}_\nu^{\mathrm{tr}}(\theta_0, \omega) = \int_{-\pi/2}^{\pi/2} \left\langle \frac{\partial T_\nu}{\partial \theta_t} \right\rangle \, d\theta_t. \tag{72b}$$

Physically $\mathcal{U}_\nu^{\mathrm{sc}}(\theta_0, \omega)$ expresses the fraction of the incident energy scattered from the surface, while in a similar way $\mathcal{U}_\nu^{\mathrm{tr}}(\theta_0, \omega)$ expresses the energy fraction transmitted through the system. Notice that the energy conservation condition should hold true for all angles of incidence and polarizations as well as being independent of the width of the incident beam. The only restriction is that there should be no medium that absorbs energy. However, if absorption is present, Eq. (71) might be modified by adding an absorption term to the right hand side. Unfortunately, this absorption term is hard to calculate in a rigorous way.

For practical purposes, the conditions Eqs. (70) and (71) are most frequently used as a test of the quality of numerical simulations (see Sec. 4.10) [224]. In such an approach these conditions are necessary, but not sufficient conditions for the correctness of the simulations.

4.5 Derivation of the reduced Rayleigh equation

The reduced Rayleigh equation (RRE), under which name we know it today, was first derived by Toigo, Marvin and Celli [95] in the last half of the 1970s. This equation is the single integral equation satisfied by the reflection or transmission amplitudes. Even if its precise region of validity is hard to quantify in detail, this equation has served as the starting point for many, if not all, of the perturbative techniques developed in the field of wave scattering from rough surface. We should stress, however, that the reduced Rayleigh equation is not restricted to the same limitations as perturbation theory, and that its validity goes beyond that of perturbation theories. Moreover, numerical simulations can be based directly on the RRE in order to obtain non-perturbative results [97,98].

We will below give the detailed derivation of the RRE for reflection. The scattering geometry that we consider is that of Fig. 8. This geometry is illuminated from above by a plane incident wave of either p- or s-polarization, and the incident plane is the x_1x_3-plane.

4.5.1 Rayleigh hypothesis

It should be apparent that for the region located above the maximum point of the surface, the total field takes the form as given by Eq. (52a), and similarly, the total field below the minimum point of the surface can be expressed according to Eq. (52b). In order to solve the scattering problem, one has to take into account the boundary conditions to be satisfied at the randomly rough surface $x_3 = \zeta(x_1)$. However, we do not know the form of the total field close to the surface, or to be more precise, in the surface region $\min \zeta(x_1) < \zeta(x_1) < \max \zeta(x_1)$. It should be obvious from a ray optical point of view, that at least for rather rough surfaces, expansions of the form (52) are not adequate to describe the total field in this region due to the lack of not allowing downward propagating scattered modes. However, as the surface becomes smother and smother, the asymptotic expansions of the field given earlier should represent a better and better approximation for the total field. This led Lord Rayleigh [16,17], when studying scattering from sinusoidal surfaces, to assume that the asymptotic expansions of the total field were not only valid in the region far away from the rough surface, but could also be used all the way down to the rough surface. Under this assumption, known today as the *Rayleigh hypothesis* [18], he could satisfy the boundary conditions on the rough surface and thereby derive the equation which lead to the solution of his scattering problem.

Validity of the Rayleigh hypothesis

Below this procedure will be demonstrated when applied to the wave scattering from a randomly rough surface. However, before doing so, we will dwell a little upon the validity of the Rayleigh hypothesis [18,99,100]. Theories based on this approximation do not properly include, as mentioned above, downward propagating scattered or upward propagating transmitted waves. From a naive ray optics argument, we realize that rays propagating towards the surface after interacting with it one or several times, will have to interact, at least, once more before escaping it. Therefore, in scattering geometries where the Rayleigh hypothesis is not valid, the scattered light has to receive substantial contributions from multiple scattering, and, thus, the surface has to be rather rough. It should, however, be stressed that this does not imply that for any scattering geometry dominated by multiple scattering, the Rayleigh hypothesis is doomed to break down. One might very well have processes dominated by multiple scattering without receiving essential contributions from downward propagating scattered waves. Good examples are provided by the ability of perturbative and numerical studies based on the Rayleigh hypothesis to show multiple scattering phenomena like the enhanced backscattering and satellite peaks [66,97,98] (Sec. 5.2.1).

Hence, the Rayleigh hypothesis is a good approximation if the surface is not too rough. However, at what level of roughness must we say that this approximation no longer is valid? There have been many studies devoted to the study of the validity of the Rayleigh approximation. For the sinusoidal surface, $x_3 = \zeta_0 \sin(\Lambda x_1)$, the Rayleigh hypothesis is formally valid when $\zeta_0 \Lambda < 0.448$ [101,102]. For randomly rough surface, however, the formal region of validity is currently unknown, but there seems to be consensus on the criterion [18,99,100,103]

$$\frac{\delta}{a} \ll 1, \tag{73}$$

where δ and a are the rms-height and correlation length of the surface respectively. The reader is encouraged to consult the literature for more details [18,103].

4.5.2 Rayleigh equations

We will now derive a set of two inhomogeneous coupled integral equation for the scattering and transmission amplitudes, $R_\nu(q|k)$ and $T_\nu(q|k)$. These equations are referred to as the Rayleigh equations, and it will now be demonstrate how they are obtained.

From Sec. 3.3 we recall that the boundary conditions to be satisfied by the field on the surface are the continuity of the field and its (scaled) normal derivative, *i.e.*

$$\Phi_\nu^+(x_1,x_3|\omega)\big|_{x_3=\zeta(x_1)} = \Phi_\nu^-(x_1,x_3|\omega)\big|_{x_3=\zeta(x_1)}\,, \tag{74a}$$

$$\partial_n\Phi_\nu^+(x_1,x_3|\omega)\big|_{x_3=\zeta(x_1)} = \left.\frac{\partial_n\Phi_\nu^-(x_1,x_3|\omega)}{\kappa_\nu(\omega)}\right|_{x_3=\zeta(x_1)}, \tag{74b}$$

where the normal derivative, ∂_n, and the symbol $\kappa_\nu(\omega)$ is defined in Eqs. (38b) and (38d).

If the Rayleigh hypothesis is assumed, the asymptotic field expansions of Sec. 4.2, can be used in order to fulfill the boundary conditions. By substituting the asymptotic expansions, Eqs. (52), into the boundary condition for the field, Eq. (74a), one is lead to the following integral equation

$$e^{ikx_1-i\alpha_0(k,\omega)\zeta(x_1)} + \int\frac{dq}{2\pi}\,R_\nu(q|k)e^{iqx_1+i\alpha_0(q,\omega)\zeta(x_1)} = \int\frac{dq}{2\pi}\,T_\nu(q|k)e^{iqx_1-i\alpha(q,\omega)\zeta(x_1)}.$$

If we now rewrite this equation, which will prove useful later, by using the properties of the Dirac δ-function, one gets

$$\int\frac{dq}{2\pi}e^{iqx_1}\Big[2\pi\delta(q-k)e^{-i\alpha_0(q,\omega)\zeta(x_1)}+R_\nu(q|k)e^{i\alpha_0(q,\omega)\zeta(x_1)}\Big] = \int\frac{dq}{2\pi}\;e^{iqx_1}\,T_\nu(q|k)\,e^{-i\alpha(q,\omega)\zeta(x_1)}. \tag{75a}$$

Doing the same for the boundary condition for the (scaled) normal derivative, *i.e.* Eq. (74b), one arrives at

$$\begin{aligned}\int\frac{dq}{2\pi}\;e^{iqx_1}&\Big[-2\pi\delta(q-k)\left\{\zeta'(x_1)q+\alpha_0(q,\omega)\right\}e^{-i\alpha_0(q,\omega)\zeta(x_1)}\\ &+R_\nu(q|k)\left\{-\zeta'(x_1)q+\alpha_0(q,\omega)\right\}e^{i\alpha_0(q,\omega)\zeta(x_1)}\Big]\\ &=-\frac{1}{\kappa_\nu(\omega)}\int\frac{dq}{2\pi}\;e^{iqx_1}\,T_\nu(q|k)\;\left\{\zeta'(x_1)q+\alpha(q,\omega)\right\}e^{-i\alpha(q,\omega)\zeta(x_1)}.\end{aligned} \tag{75b}$$

Together Eqs. (75) constitute a set of coupled inhomogeneous integral equations announced earlier – the Rayleigh equations.

4.5.3 Reduced Rayleigh equations

We will now continue to derive the so-called reduced Rayleigh equation (RRE) for reflection [38,95] and transmission [38,96]. The RRE is a single integral equation satisfied by the reflection or transmission amplitude. They are derived from the Rayleigh equations by eliminating the transmission or the reflection amplitude, respectively.

Reduced Rayleigh equation for reflection

In order to obtain the reduced Rayleigh equation for reflection, we have to eliminate the transmission amplitude, $T_\nu(q|k)$ from the (coupled) Rayleigh equations given in the previous subsection. Multiplying Eq. (75a) by

$$e^{-ipx_1-i\alpha(p,\omega)\zeta(x_1)}\left[-\zeta'(x_1)p+\alpha(p,\omega)\right], \tag{76}$$

and Eq. (75b) by

$$\kappa_\nu(\omega)e^{-ipx_1-i\alpha(p,\omega)\zeta(x_1)}, \tag{77}$$

adding the two resulting equations, and integrating the final result over x_1, one finds that the terms containing the transmission amplitude vanish exactly. In detail, the terms proportional to $T_\nu(q|k)$ are

$$\int dx_1 \frac{dq}{2\pi} T_\nu(q|k) \left[-\zeta'(x_1)(p+q) + \alpha(p,\omega) - \alpha(q,\omega)\right] e^{-i(p-q)x_1} e^{i(-\alpha(p,\omega)-\alpha(q,\omega))\zeta(x_1)}. \quad (78)$$

This expression is simplified by introducing an integral defined according to[11]

$$I(\gamma|q) = \int dx_1 \, e^{-i\gamma\zeta(x_1)} e^{-iqx_1}. \quad (79)$$

From this definition it follows that

$$\frac{qI(\gamma|q)}{\gamma} = -\int dx_1 \, \zeta'(x_1) e^{-i\gamma\zeta(x_1)} e^{-iqx_1}. \quad (80)$$

With Eqs. (79) and (80), Eq. (78) can be written in the form

$$\int \frac{dq}{2\pi} T_\nu(q|k) \left[\frac{(p-q)(p+q)}{\alpha(p,\omega)+\alpha(q,\omega)} + \alpha(p,\omega) - \alpha(q,\omega)\right] I(\alpha(p,\omega)+\alpha(q,\omega)|p-q).$$

After some simple algebra, it can be readily shown that the expression in the square brackets is identically zero, and thus the transmission amplitude $T_\nu(q|k)$ has been eliminated from the Rayleigh equations.

The reduced Rayleigh equation for reflection now follows from the remaining non-vanishing parts of the equation that can be written

$$\int \frac{dq}{2\pi} M_\nu^+(p|q) R_\nu(q|k) = M_\nu^-(p|k) \quad (81a)$$

where

$$M_\nu^\pm(p|q) = \pm \left[\frac{(p+\kappa_\nu(\omega)q)(p-q)}{\alpha(p,\omega) \mp \alpha_0(q,\omega)} + \alpha(p,\omega) \pm \kappa_\nu(\omega)\alpha_0(q,\omega)\right] I\left(\alpha(p,\omega) \mp \alpha_0(q,\omega)|p-q\right). \quad (81b)$$

If we restrict ourselves to p-polarization, the reduced Rayleigh equation as presented in Eqs. (81) takes on a simpler form. By a straight forward calculation one finds[12]

$$\int \frac{dq}{2\pi} N_p^+(p|q) R_p(q|k) = N_p^-(p|k), \quad (82a)$$

where

$$N_p^\pm(p|q) = \pm \frac{pq \pm \alpha(p,\omega)\alpha_0(q,\omega)}{\alpha(p,\omega) \mp \alpha_0(q,\omega)} I\left(\alpha(p,\omega) \mp \alpha_0(q,\omega)|p-q\right). \quad (82b)$$

Similarly for s-polarization one finds[13]

$$\int \frac{dq}{2\pi} N_s^+(p|q) R_s(q|k) = N_s^-(p|k), \quad (83a)$$

where

$$N_s^\pm(p|q) = \pm \frac{1}{\alpha(p,\omega) \mp \alpha_0(q,\omega)} I\left(\alpha(p,\omega) \mp \alpha_0(q,\omega)|p-q\right). \quad (83b)$$

[11] Be aware that different sign conventions appear in the literature for this quantity.
[12] Here the matrix elements $M_p^\pm(p|q)$ and $N_p^\pm(p|q)$ are related by $M_p^\pm(p|q) = (\varepsilon(\omega)-1)N_p^\pm(p|q)$.
[13] Here is $M_s^\pm(p|q) = (\varepsilon(\omega)-1)(\omega/c)^2 N_s^\pm(p|q)$.

Reduced Rayleigh equation for transmission

In the previous subsection it was shown that by eliminating the terms containing the transmission amplitude from the Rayleigh equations, the reduced Rayleigh equation for reflection was obtained. In a similar way, the scattering amplitude might be eliminated from the same equations, resulting in the reduced Rayleigh equation for transmission.

Here we will not go into details of how this is done, since the derivation mimics the one given in the previous subsection. Therefore, we will only state the resulting reduced Rayleigh equation satisfied by the transmission amplitudes $T_\nu(q|k)$ ($\nu = p, s$). In the case of p-polarization this equation reads [96]

$$\int_{-\infty}^{\infty} \frac{dq}{2\pi} \frac{I(\alpha(q,\omega) - \alpha_0(p,\omega)|p-q)}{\alpha(q,\omega) - \alpha_0(p,\omega)} \; [pq + \alpha_0(p,\omega)\alpha(q,\omega)]\, T_p(q|k) = 2\pi\delta(p-k) \frac{2\varepsilon(\omega)\alpha_0(k,\omega)}{\varepsilon(\omega)-1}, \tag{84a}$$

while for s-polarization it can be written as [96]

$$\int_{-\infty}^{\infty} \frac{dq}{2\pi} \frac{I(\alpha(q,\omega) - \alpha_0(p,\omega)|p-q)}{\alpha(q,\omega) - \alpha_0(p,\omega)} \; T_s(q|k) = 2\pi\delta(p-k) \frac{2\alpha_0(k,\omega)}{\frac{\omega^2}{c^2}\,[\varepsilon(\omega)-1]}. \tag{84b}$$

This concludes our discussion of the reduced Rayleigh equation.

In passing, we would like to mention that we here have only considered the simples geometry. Reduced Rayleigh equations have also been obtained for other more complex scattering geometries, both one- and two-dimensional, and for one or several rough surfaces [38,39,97,98,104–107,182].

4.6 Small amplitude perturbation theory

Among the oldest theories addressing rough surface scattering we find the small amplitude perturbation theory [20,104,108,117,181]. The starting point for this perturbation theory, like most of the perturbation theories developed for handling wave scattering from rough surface, is the reduced Rayleigh equation (81). If the rough surface is weakly rough, most of the light incident upon it is scattered into the specular direction. However, due to the surface roughness, a small fraction of the incident power is scattered away from the specular direction. Theoretically, this non-specular scattering is taken into account by assuming an expansion for the scattering amplitude in powers of the surface profile function of the form[14] [117]

$$R_\nu(q|k) = \sum_{n=0}^{\infty} \frac{(-i)^n}{n!} R_\nu^{(n)}(q|k). \tag{85}$$

Here $R_\nu^{(n)}(q|k)$ is assumed to be of order $\mathcal{O}(\zeta^n)$ in the surface profile function $\zeta(x_1)$. In order to solve the scattering problem by this method, we have to determine the expansion coefficients $\{R_\nu^{(n)}(q|k)\}$. However, to determine all these coefficients is obviously not practically possible if $\zeta(x_1)$ is a rough surface. Therefore, the expansion (85) is terminated at some upper value N, resulting in an N'th order perturbation theory. In practical application one usually takes N in the range 3–5. If the surface is weakly rough, the sum of these N terms will provide a good approximation to the total scattering amplitude $R_\nu(q|k)$. However, as the surface roughness becomes stronger and stronger, a higher number of terms have to be included in the expansion, and the method becomes cumbersome and not very practical since $R_\nu^{(n)}(q|k)$ for big values of n easily becomes complicated. Thus, the small amplitude perturbation theory is only of interest for weakly rough surfaces. Hence, it should therefore not represent any restriction to assume

[14] The factor $(-i)^n/n!$ is introduced for later convenience.

that the Rayleigh hypothesis is valid and therefore that $R_\nu(q|k)$ should satisfy the reduced Rayleigh equation, Eq. (81).

Under this assumption, the various terms in the expansion for the scattering amplitude can in principle be obtained by substituting its expansion, Eq. (85), into the reduced Rayleigh equation, Eq. (81), and satisfy the resulting equation order-by-order in the surface profile function $\zeta(x_1)$. However, before this can be done, $N_\nu^\pm(p|q)$, or equivalently $M_\nu^\pm(p|q)$, that enter the reduced Rayleigh equation, also have to be expanded in powers of the surface profile function. Since the matrix-elements, $N_\nu^\pm(p|q)$, only depend on $\zeta(x_1)$ through the integrals $I(\gamma|q)$, defined in Eq. (79), one makes the following expansion

$$I(\gamma|q) \equiv \int dx_1\, e^{-i\gamma\zeta(x_1)} e^{-iqx_1} = \sum_{n=0}^{\infty} \frac{(-i\gamma)^n}{n!}\, \tilde{\zeta}^{(n)}(q), \tag{86a}$$

where

$$\tilde{\zeta}^{(n)}(q) = \int_{-\infty}^{\infty} dx_1\, \zeta^n(x_1) e^{-iqx_1}, \tag{86b}$$

is the (inverse) Fourier transform of the nth power of the surface profile function. From the above equations it should be apparent why we made the choice we did for the prefactors in the expansion for $R_\nu(q|k)$.

When the expansion (86) is substituted into the expressions for $N_\nu^\pm(p|q)$, Eqs. (82b) and (83b), one obtains

$$N_\nu^\pm(p|q) = \sum_{n=0}^{\infty} \frac{\mathcal{N}_\nu^{\pm\,(n)}(p|q)}{n!} \tilde{\zeta}^{(n)}(p-q), \tag{87a}$$

where for p-polarization

$$\mathcal{N}_p^{\pm\,(0)}(p|p) = \frac{\varepsilon(\omega)\alpha_0(p,\omega) \pm \alpha(p,\omega)}{\varepsilon(\omega) - 1}, \tag{87b}$$

and

$$\mathcal{N}_p^{\pm\,(n)}(p|q) = (-i)^n \left[\pm pq + \alpha(p,\omega)\alpha_0(q,\omega)\right] \left[\alpha(p,\omega) \mp \alpha_0(q,\omega)\right]^{n-1}, \tag{87c}$$

when $n \geq 1$, while for s-polarization we have

$$\mathcal{N}_s^{\pm\,(0)}(p|p) = \frac{\alpha_0(p,\omega) \pm \alpha(p,\omega)}{\frac{\omega^2}{c^2}\left(\varepsilon(\omega) - 1\right)}, \tag{87d}$$

and

$$\mathcal{N}_s^{\pm\,(n)}(p|q) = \pm(-i)^n \left[\alpha(p,\omega) \mp \alpha_0(q,\omega)\right]^{n-1}, \tag{87e}$$

when $n \geq 1$.

With these relations available, a recurrence relations for $\{R_\nu^{(n)}(p|q)\}$, is readily obtained by substituting Eqs. (85) and (87) into the reduced Rayleigh equation, Eqs. (82a) and (83a), and equating terms of the same order in $\tilde{\zeta}(q)$. The resulting recurrence relation reads

$$\sum_{m=0}^{\infty} \binom{n}{m} \int_{-\infty}^{\infty} \frac{dp}{2\pi}\, \mathcal{N}_\nu^{+\,(n-m)}(q|p) \tilde{\zeta}^{(n-m)}(q-p) R_\nu^{(m)}(p|k) = \mathcal{N}_\nu^{-\,(n)}(q|k) \tilde{\zeta}^{(n)}(q-k). \tag{88}$$

Now the expansion coefficients for the scattering amplitude, $R_\nu^{(n)}(p|q)$, should be rather straight forward to obtain (at least in principle). The lowest order term ($n = 0$) is given as

$$R_\nu^{(0)}(q|k) = 2\pi\, \delta(p-k) R_\nu^{(0)}(k,\omega), \tag{89a}$$

where $R_\nu^{(0)}(k,\omega)$ is defined by (assuming $\varepsilon_0 = 1$ and $\mu = \mu_0 = 1$)

$$R_\nu^{(0)}(k,\omega) = \begin{cases} \dfrac{\varepsilon(\omega)\alpha_0(k,\omega) - \alpha(k,\omega)}{\varepsilon(\omega)\alpha_0(k,\omega) + \alpha(k,\omega)}, & \nu = p, \\ \dfrac{\alpha_0(k,\omega) - \alpha(k,\omega)}{\alpha_0(k,\omega) + \alpha(k,\omega)}, & \nu = s. \end{cases} \tag{89b}$$

In these expressions, the momentum variables k and q are understood to be related to the angles of incidence and scattering, θ_0 and θ_s respectively, through

$$k = \frac{\omega}{c}\sin\theta_0, \tag{90a}$$

$$q = \frac{\omega}{c}\sin\theta_s. \tag{90b}$$

The above results are, as expected, what one would obtain for the scattering from a planar surface, since $R_\nu^{(0)}(k,\omega)$ is nothing but the Fresnel reflection coefficients [9]. Notice that the δ-function in Eq. (89a), coming from $\tilde{\zeta}^{(0)}$, guarantees that the scattering is only into the specular direction.

The results for the higher order terms ($n \geq 1$) in the expansion of $R_\nu(q|k)$, describe the light scattered by the roughness into directions other than the specular. These terms can be calculated recursively from Eq. (88), but, unfortunately, such expressions easily become rather cumbersome for higher order terms. However, the first few terms are manageable, and they are given by the following expressions [109,117]

$$R_\nu^{(1)}(q|k) = \chi_\nu^{(1)}(q|k)\,\tilde{\zeta}(q-k), \tag{91a}$$

$$R_\nu^{(2)}(q|k) = \int_{-\infty}^{\infty}\frac{dp}{2\pi}\chi_\nu^{(2)}(q|p|k)\,\tilde{\zeta}(q-p)\tilde{\zeta}(p-k), \tag{91b}$$

$$R_\nu^{(3)}(q|k) = \int_{-\infty}^{\infty}\frac{dp_1}{2\pi}\int_{-\infty}^{\infty}\frac{dp_2}{2\pi}\chi_\nu^{(3)}(q|p_1|p_2|k)\,\tilde{\zeta}(q-p_1)\tilde{\zeta}(p_1-p_2)\tilde{\zeta}(p_2-k), \tag{91c}$$

where, the functions $\chi_\nu^{(1)}(q|k)$, $\chi_\nu^{(2)}(q|p|k)$, ... are somewhat lengthy functions of their arguments, and are therefore given separately in Appendix B.

As discussed previously, the first few terms of the expansion (85) with Eqs. (91) substituted, should hence for a weakly rough surfaces represent a good (3rd order) approximation to $R_\nu(q|k)$. Experimental accessible quantities could therefore be calculated based on this approximation. For instance, the mean differential reflection coefficient from the incoherent component of the scattered field is then, according to Eq. (63b), through fourth order in the surface profile function, given by

$$\left\langle \frac{\partial R_\nu}{\partial\theta_s}\right\rangle_{\text{incoh}} = \frac{1}{L_1}\frac{\omega}{2\pi c}\frac{\cos^2\theta_s}{\cos\theta_0}\left[\left\langle\left|R_\nu^{(1)}(q|k)\right|^2\right\rangle + \frac{1}{4}\left\{\left\langle\left|R_\nu^{(2)}(q|k)\right|^2\right\rangle - \left|\left\langle R_\nu^{(2)}(q|k)\right\rangle\right|^2\right\}\right.$$
$$\left. -\frac{1}{3}Re\left\langle R_\nu^{(3)}(q|k)R_\nu^{(1)\,*}(q|k)\right\rangle\right] + \mathcal{O}(\delta^6). \tag{92a}$$

In arriving at Eq. (92a) it has been assumed that the surface profile function, $\zeta(x_1)$, constitutes a zero-mean, stationary, Gaussian random process. Due to the Gaussian character of the surface, only terms that contain an even number of surface profile function survive the averaging process. The different averaged contained in Eq. (92a) can all be related to the set of functions $\{\chi_\nu^{(n)}(q|k)\}$ according to

$$\left\langle\left|R_\nu^{(1)}(q|k)\right|^2\right\rangle = L_1\delta^2 g(|q-k|)\left|\chi_\nu^{(1)}(q|k)\right|^2, \tag{92b}$$

$$\left\langle \left| R_\nu^{(2)}(q|k) \right|^2 \right\rangle - \left| \left\langle R_\nu^{(2)}(q|k) \right\rangle \right|^2 = L_1 \delta^4 \int_{-\infty}^{\infty} \frac{dp}{2\pi} g(|q-p|) g(|p-k|) \times \left\{ \left| \chi_\nu^{(2)}(q|p|k) \right|^2 + \chi_\nu^{(2)}(q|p|k) \chi_\nu^{(2)\,*}(q|q+k-p|k) \right\}, \tag{92c}$$

and

$$\left\langle R_\nu^{(3)}(q|k) R_\nu^{(1)\,*}(q|k) \right\rangle = L_1 \delta^4 g(|q-k|) \chi_\nu^{(1)\,*}(q|k) \int_{-\infty}^{\infty} \frac{dp}{2\pi} \times \left\{ \chi_\nu^{(3)}(q|p|q|k) g(|p-q|) + \chi_\nu^{(3)}(q|k|p|k) g(|p-k|) + \chi_\nu^{(3)}(q|p|p+k-q|k) g(|p-q|) \right\}. \tag{92d}$$

Notice that the term (92b) represents single scattering, while the terms in Eq. (92c) give the contribution due to double scattering, while Eq. (92d) represents a "mixed" contribution. The terms in Eqs. (92b)–(92d) are often referred to as the 1–1, 2–2, and 3–1 terms, respectively.

Accuracy of the small amplitude perturbation theory

So what accuracy can we expect to achieve by using the small amplitude perturbation theory, and for what range of surface parameters is it valid? There have been many studies in the past, both of theoretical, numerical, and experimental nature, addressing this issue [29,110,110,111,117]. Currently, there is consensus on small-amplitude perturbation theory being accurate when [29,110,111,117]

$$|\sqrt{\varepsilon(\omega)}| \frac{\omega}{c} |\zeta(x_1)| \ll 1, \tag{93a}$$

$$|\zeta'(x_1)| \ll 1. \tag{93b}$$

For a randomly rough surface of rms-height, δ, and (finite) correlation length, a, the above expressions translate into (*c.f.* Eqs. (6) and (10))

$$|\sqrt{\varepsilon(\omega)}| \frac{\omega}{c} \delta \;=\; 2\pi |\sqrt{\varepsilon(\omega)}| \frac{\delta}{\lambda} \ll 1, \tag{94a}$$

and

$$\frac{\delta}{a} \ll 1, \tag{94b}$$

where we have used that the average values for $|\zeta(x_1)|$ and $|\zeta'(x_1)|$ are of the order δ and $s \propto \delta/a$, respectively. The first condition (94a) comes from the fact that quantities containing the surface profile function should be expandable in a Taylor series about their mean surface. The second criterion that states that the correlation length of the surface can not be too big, originates from the fact that if the correlation length of the surface is too large the Gaussian height distribution becomes close to a δ-function with the result that the second order term in the perturbative expansion can be of the same order as the first order term even if Eq. (94a) is satisfied. Moreover, it has been found that if the surface is non-Gaussian it is found that the above criteria can be relaxed somewhat [112].

4.7 Unitary and reciprocal expansions

In the previous section we presented small-amplitude perturbation theory, which is based on the expansion of the scattering amplitude $R_\nu(q|k)$ in powers of the surface profile function

$\zeta(x_1)$. In Sec. 4.4.1 we claimed that a valid theory for rough surface scattering should satisfy reciprocity, *i.e.* the theory should satisfy the relation $S_\nu(q|k) = S_\nu(-k|-q)$, where $S_\nu(q|k)$ is the scattering matrix defined in Eq. (66). By inspecting the formulae obtained in the previous section for $R_\nu(q|k)$, it is at least not obvious that reciprocity is satisfied. Does this mean that small amplitude perturbation theory does not respect the principle of reciprocity, and therefore is an incorrect theory? The answer to this question is no, as you might have guessed, and the small amplitude perturbation theory does in fact respect reciprocity. However, to see this is not straight forward since an extensive rewriting of the expressions are required. Theories where reciprocity is not apparent at first glance is normally referred to by saying that the theory is not manifestly reciprocal.

Due to the lack of manifest reciprocity of small amplitude perturbation theory as well as the desire to map the classical scattering problem onto the formalism of a quantum mechanical scattering problem [113], Brown et al. [114,115], in the first half of the 1980s, constructed a theory which was manifestly reciprocal. This theory goes today under the name of many-body perturbation theory, but is also known as self-energy perturbation theory. It is this kind of perturbation theory that we will concern ourselves with in this section.

4.7.1 The transition matrix

The starting point for the many-body perturbation theory is to postulate the scattering amplitude $R_\nu(q|k)$ to satisfy the relation [39,115,180]

$$R_\nu(q|k) = 2\pi\delta(q-k)R_\nu^{(0)}(k,\omega) - 2iG_\nu^{(0)}(q,\omega)\mathcal{T}_\nu(q|k)G_\nu^{(0)}(k,\omega)\alpha_0(k,\omega). \tag{95}$$

Here $R_\nu^{(0)}(k,\omega)$ is the Fresnel reflection amplitude as defined by Eq. (89b). The second term of this equation, containing the transition matrix $\mathcal{T}_\nu(q|k)$, also known as the T-matrix, represents the field scattered away from the specular direction. Furthermore, $G_\nu^{(0)}(k,\omega)$ is the surface plasmon polariton Green's function for the planar vacuum-metal interface. This Green's function can be defined from the relation

$$2i\alpha_0(k,\omega)G_\nu^{(0)}(k,\omega) + R_\nu^{(0)}(k,\omega) = -1, \tag{96a}$$

that leads to the following expressions [39]

$$G_\nu^{(0)}(k,\omega) = \begin{cases} \dfrac{i\varepsilon(\omega)}{\varepsilon(\omega)\alpha_0(k,\omega) + \alpha(k,\omega)}, & \nu = p, \\ \dfrac{i}{\alpha_0(k,\omega) + \alpha(k,\omega)}, & \nu = s. \end{cases} \tag{96b}$$

4.7.2 Scattering potentials

The transition matrix is postulated to satisfy the following equation [39,115,180]

$$\mathcal{T}_\nu(p|k) = V_\nu(p|k) + \int_{-\infty}^{\infty} \frac{dq}{2\pi} V_\nu(p|q)G_\nu^{(0)}(q,\omega)\mathcal{T}_\nu(q|k), \tag{97a}$$

$$= V_\nu(p|k) + \int_{-\infty}^{\infty} \frac{dq}{2\pi} \mathcal{T}_\nu(p|q)G_\nu^{(0)}(q,\omega)V_\nu(q|k), \tag{97b}$$

where $V(q|k)$ is known as the *scattering potential*. It is supposed to be a non-resonant function of its arguments, *i.e.* not containing the Green's function $G_\nu^{(0)}$. In arriving at Eq. (97b) we have used explicitly that both $V_\nu(p|k)$ and $\mathcal{T}_\nu(p|k)$ are reciprocal, *i.e.* that $V_\nu(p|k) = V_\nu(-k|-p)$ with a similar expression for the transition amplitude[15].

[15] That this is indeed the case might be confirmed from the expressions to be derived later for these quantities.

We now seek an (integral) equation satisfied by the T-matrix. This is done by substituting Eq. (95) into the reduced Rayleigh equation (81), and thereby obtaining

$$\int \frac{dq}{2\pi} N_\nu^+(p|q) G_\nu^0(q,\omega) \mathcal{T}_\nu(q|k) = \frac{R_\nu^{(0)}(k,\omega) N_\nu^+(q|k) - N_\nu^-(p|k)}{2i\alpha_0(k,\omega) G_\nu^{(0)}(k,\omega)}. \tag{98}$$

Even though, the many-body perturbation theory could have proceeded from this equation, it has proven useful from a purely algebraic point of view, to instead of the T-matrix work in terms of the scattering potential $V_\nu(q|k)$. Thus we aim to obtain an integral equation for this quantity which our perturbation theory will be based directly upon. By substituting the right hand side of Eq. (97a) into Eq. (98), making a change of variable and using Eq. (97a) once more, one obtains the desired integral equation for the scattering potential

$$\int \frac{dq}{2\pi} A_\nu(p|q) V_\nu(q|k) = B_\nu(p|k), \tag{99a}$$

where the matrix elements are given by

$$\begin{aligned} A_\nu(p|q) &= \frac{\left[2i\alpha_0(q,\omega) G_\nu^{(0)}(q,\omega) + R_\nu^{(0)}(q,\omega)\right] N_\nu^+(p|q) - N_\nu^-(p|q)}{2i\alpha_0(k,\omega)} \\ &= -\frac{N_\nu^+(p|q) + N_\nu^-(p|q)}{2i\alpha_0(q,\omega)}, \end{aligned} \tag{99b}$$

and

$$B_\nu(p|k) = \frac{R_\nu^{(0)}(p,\omega) N_\nu^+(p|k) - N_\nu^-(p|k)}{2i\alpha_0(k,\omega) G_\nu^{(0)}(k,\omega)}. \tag{99c}$$

To obtain $A_\nu(p|q)$ we have explicitly taken advantage of Eq. (96a). With the expression presented for the matrix elements for the reduced Rayleigh equation, $N_\nu^\pm(q|k)$, it is now straightforward to obtain closed form expressions for $A_\nu(p|q)$ and $B_\nu(p|k)$, but we will not present such expressions here.

The integral equation (99) will be the starting point for our manifestly reciprocal many-body perturbation theory. The essence of the theory is to expanding the scattering potential in powers of the surface roughness $\zeta(x_1)$ according to

$$V_\nu(q|k) = \sum_{n=0}^{\infty} \frac{(-i)^n}{n!} V_\nu^{(n)}(q|k). \tag{100}$$

with similar expansions for $A_\nu(p|q)$ and $B_\nu(p|q)$. In these expressions the superscripts denotes, as earlier, the order of the corresponding terms in the surface profile function.

One of the advantages of this theory is that even a lower order approximation to the scattering potential corresponds to a resummation of an infinite number of terms in an expansion in powers of the surface profile function[16].

We will here not go into detail, but it can be shown that the results for the few first terms in the expansion of the scattering potential are [116–118]

$$V_\nu^{(1)}(q|k) = \begin{cases} i\dfrac{\varepsilon(\omega)-1}{\varepsilon^2(\omega)} \left[\varepsilon(\omega) qk - \alpha(q,\omega)\alpha(k,\omega)\right] \tilde{\zeta}^{(1)}(q-k), & \nu = p, \\ i\dfrac{\omega^2}{c^2}(\varepsilon(\omega)-1)\tilde{\zeta}^{(1)}(q-k), & \nu = s, \end{cases} \tag{101a}$$

[16] This is also the case for the so-called many-body (self-energy) perturbation theory to be presented in the next section.

for the 1st oder term, and

$$V_p^{(2)}(q|k) = i\frac{\varepsilon(\omega)-1}{\varepsilon^2(\omega)}\left[\alpha(q,\omega)+\alpha(k,\omega)\right]\left[qk-\alpha(q,\omega)\alpha(k,\omega)\right]\tilde{\zeta}^{(2)}(q-k) + 2i\frac{(\varepsilon(\omega)-1)^2}{\varepsilon^3(\omega)}\alpha(q,\omega)\int_{-\infty}^{\infty}\frac{dp}{2\pi}\tilde{\zeta}^{(1)}(q-p)\alpha(p,\omega)\tilde{\zeta}^{(1)}(p-k)\alpha(k,\omega), \quad (101b)$$

and

$$V_s^{(2)}(q|k) = i\frac{\omega^2}{c^2}(\varepsilon(\omega)-1)\left[\alpha(q,\omega)+\alpha(k,\omega)\right]\tilde{\zeta}^{(2)}(q-k), \quad (101c)$$

for the second order terms. Higher order terms can be found in *e.g.* Ref. [118]. It should be mentioned that by definition the lowest non-vanishing order of the scattering potential is 1st order in the surface profile function. In other words $V_\nu^{(0)}(p|q) = 0$ always.

As the reader easily may check, the above expressions are manifest reciprocal, *i.e.*

$$V_\nu^{(n)}(q|k) = V_\nu^{(n)}(-k|-q),$$

and this property should hold true to all orders in the surface profile function [115]. However, it should be emphasized that expressions of this form are not obtained directly from the solution of Eq. (99), but that some rewritings instead are needed for [116,117].

If the transmission matrix is expanded in a similar way to Eq. (100) for the scattering potential, *i.e.*

$$\mathcal{T}_\nu(q|k) = \sum_{n=0}^{\infty}\frac{(-i)^n}{n!}\mathcal{T}_\nu^{(n)}(q|k), \quad (102)$$

a recurrence relation for $\{\mathcal{T}_\nu^{(n)}(p|q)\}$ in terms of $V_\nu^{(m)}(p|q)$ can be derived and thus $T_\nu(q|k)$ to some order can be calculated.

Hence, through the calculation of the scattering potential, the T-matrix can be obtained. The contribution to the mean differential reflection coefficient from the incoherent component of the scattered light is

$$\left\langle\frac{\partial R_\nu}{\partial\theta_s}\right\rangle_{\text{incoh}} = \frac{1}{L_1}\frac{2}{\pi}\left(\frac{\omega}{c}\right)^3\cos^2\theta_s\cos\theta_0\left|G_\nu^{(0)}(q,\omega)\right|^2 \times\left[\left\langle|\mathcal{T}_\nu(q|k)|^2\right\rangle - |\langle\mathcal{T}_\nu(q|k)\rangle|^2\right]\left|G_\nu^{(0)}(k,\omega)\right|^2. \quad (103)$$

This expression is obtained by substituting Eq. (95) into the defining expression for the incoherent component of the mean DRC (Eq. (63b)).

4.8 Many-Body perturbation theory

The Green's function $G_\nu^{(0)}(q,\omega)$, we recall, is the surface plasmon polariton Green's function at a planar interface. In addition to this Green's function it is also useful to define a rough surface Green's function, $G_\nu(q|k)$, or more formally the Green's function of a ν-polarized electromagnetic field at the randomly rough interface. Some authors refer to this function as the *renormalized* Green's function. It is defined as the solution of the following equation [115,180,181]

$$G_\nu(q|k) = 2\pi\delta(q-k)G_\nu^{(0)}(k) + G_\nu^{(0)}(q)\int_{-\infty}^{\infty}\frac{dp}{2\pi}V_\nu(q|p)G_\nu(p|k). \quad (104a)$$

This equation is often in the literature referred to as the *Lippmann-Schwinger equation* [119] for the renormalized Green's function $G_\nu(q|k)$. Notice that from Eqs. (95) and (104a) it follows

that $R_\nu(q|k) = -2\pi\delta(q-k) - 2iG_\nu(q|k)\alpha_0(k)$. An alternative way of expressing the above equation is obtained by iterating on $G_\nu(q|k)$. The result can be written as

$$G_\nu(q|k) = 2\pi\delta(q-k)G_\nu^{(0)}(k) + G_\nu^{(0)}(q)\mathcal{T}_\nu(q|p)G_\nu^{(0)}(k), \tag{104b}$$

where we have used a Born series [113] expansion for the T-matrix in Eq. (97). This equation is often for simplicity expressed in operator form as $G = G_0 + G_0TG_0$.

In terms of the renormalized Green's function the mean DRC takes on the form

$$\left\langle \frac{\partial R_\nu}{\partial\theta_s} \right\rangle_{\text{incoh}} = \frac{1}{L_1}\frac{2}{\pi}\frac{\omega^3}{c^3}\cos^2\theta_s\cos\theta_0\left[\left\langle |G_\nu(q|k)|^2 \right\rangle - |\langle G_\nu(q|k)\rangle|^2\right], \tag{105}$$

where the method of smoothing [120] has been applied to Eq. (95) as well as the reduced Rayleigh equation. In these expressions the mean of the renormalized Greens function satisfies the *Dyson equation* [121]

$$\langle G_\nu(q|k)\rangle = 2\pi\delta(q-k)G_\nu^{(0)}(k) + G_\nu^{(0)}(q)\int_{-\infty}^{\infty}\frac{dp}{2\pi}\,\langle M_\nu(q|p)\rangle\,\langle G_\nu(p|k)\rangle\,, \tag{106a}$$

where the unaveraged *proper self-energy* $M_\nu(q|k)$ is a solution of the equation

$$M_\nu(q|k) = V_\nu(q|k) + \int_{-\infty}^{\infty}\frac{dp}{2\pi}\,M_\nu(q|p)G_\nu^{(0)}(p)\left[V_\nu(p|k) - \langle V_\nu(p|k)\rangle\right]. \tag{106b}$$

Since the surface profile function is stationary, both the renormalized Green's function and the proper self-energy are diagonal in the momentum variables q and k, *i.e.*

$$\langle G_\nu(q|k)\rangle = 2\pi\delta(q-k)G_\nu(k), \tag{107}$$

with a similar expression for the proper self-energy. Under this assumption the renormalized Green's function can formally be written as [116,117].

$$G_\nu(k) = \frac{1}{\left[G_\nu^{(0)}(k)\right]^{-1} - M_\nu(k)}. \tag{108}$$

Hence the surface polariton poles in $G_\nu(k)$ are shifted as compared to those of $G_\nu^{(0)}(k)$ due to the presence of $M_\nu(k)$. The self-energy can be calculated perturbatively as an expansion in powers of the surface profile function. The resulting perturbation theory is known as self-energy perturbation theory [117].

The two-particle average Green's function satisfies a *Bethe-Salpeter equation* [113,122] of the form[17]

$$\left\langle |G_\nu(q|k)|^2 \right\rangle = L_1 2\pi\delta(q-k)\,|G_\nu(q)|^2 + |G_\nu(q)|^2\int_{-\infty}^{\infty}\frac{dp}{2\pi}\,U_\nu(q|p)\left\langle |G_\nu(p|k)|^2 \right\rangle, \tag{109}$$

where $U_\nu(q|p)$ is the so-called irreducible vertex function. Formally, one may write the solution to Eq. (109) as

$$\left\langle |G_\nu(q|k)|^2 \right\rangle = L_1 2\pi\delta(q-k)\,|G_\nu(q)|^2 + L_1\,|G_\nu(q)|^2\,X_\nu(q|k)\,|G_\nu(k)|^2\,, \tag{110}$$

where $X_\nu(q|k)$ is the reducible vertex function. With this equation the mean DRC takes on the form

$$\left\langle \frac{\partial R_\nu}{\partial\theta_s} \right\rangle_{\text{incoh}} = \frac{2}{\pi}\frac{\omega^3}{c^3}\cos^2\theta_s\cos\theta_0\,|G_\nu(q)|^2\,X_\nu(q|k)\,|G_\nu(k)|^2\,. \tag{111}$$

[17] In arriving at this equation also here the method of smoothing [120] has been applied.

The reducible vertex function can be shown to be related to $U_\nu(Q|k)$ though the equation

$$X_\nu(q|k) = U_\nu(q|k) + \int_{-\infty}^{\infty} \frac{dp}{2\pi}\, U_\nu(q|p)\, |G_\nu(p)|^2\, X_\nu(p|k). \tag{112}$$

Unfortunately we do not know, in general, how to solve the Bethe-Salpeter equation (109). Hence some approximative methods have to be employed. The most frequently used methods are the Freilikher factorization [123], or a diagrammatic method [12,113,124]. In this latter approach $X_\nu(q|k)$ is approximated by a subset of (an infinite number of) diagrams. Those usually are the ladder diagrams and the maximally-crossed diagrams, where the former describes wave diffusion in the random media, while the latter is related to wave localization.

With this approach it can be shown that the reducible vertex function for p-polarized light incident on a rough metal surface can be written as [124]

$$X_p(q|k) = \left[U_p^{(0)}(q|k) + \frac{A(q|k)}{4\Delta^2} + \frac{A\left(\frac{q-k}{2}|\frac{k-q}{2}\right)}{(q+k)^2 + 4\Delta^2} \right], \tag{113}$$

which when substituted into Eq. (111) defines the mean DRC in this approximation. Here, $A(q|k)$ is a smooth function of its arguments and $\Delta = \Delta_\varepsilon + \Delta_{spp}$ is the (total) decay rate of surface plasmon polaritons due to Ohmic losses (Δ_ε) in the metal and conversion into other surface plasmon polaritons ($\Delta_{spp} \simeq Im(M(k_{spp}))$). Their mathematical expressions, as well as the other quantities appearing in Eq. (113), can be found in Ref. [124]. The first term in Eq. (113) is due to single-scattering, the second arises from the ladder diagrams, while the last one is the contribution from the maximally-crossed diagrams. This last term is the one that is responsible for the enhanced backscattering phenomenon that we will discuss in the next section.

It should be mentioned that in arriving at Eq. (113) the *pole-approximation* for the renormalized Green's function has been utilized. This approximation amount to writing

$$G_p(k) \simeq \frac{C(\omega)}{k - k_{spp} - i\Delta} - \frac{C(\omega)}{k + k_{spp} + i\Delta}, \tag{114}$$

where k_{spp} is the wave vector of the surface plasmon polariton (see Eq. (43)), and $C(\omega)$ is a constant. The Green's function for s-polarization does not have poles, and the pole-approximation is thus not relevant in this case.

4.9 Other perturbation theories

In Secs. 4.6 and 4.8 we discussed two popular perturbation theories. However, they are not the only ones [29]. Over the years, various theories have been developed. It is outside the scope of this review to discuss them all.

For completeness, however, we would still take the opportunity to present a (not complete list) of such theories. It includes: phase perturbation theory [117,125–129]; the local and non-local small-slope perturbation theories [32,130–132]; the distorted-wave Born approximation [133]; low contrast perturbation theory [134]; perturbation theories based on the Ewald-Oseen extinction theorem [135]; the full wave method [136]; the operator expansion [137]; and the unified perturbation theory [138].

4.10 Numerical simulation approach

In Secs. 4.6 and 4.8 two perturbation theories were discussed. Such theories catch the main physics of the scattering problem if the surfaces are not too rough. However, for interfaces

that are strongly rough, no perturbative approach can be used because too many terms in the expansions have to be included in order for the approach to be practical.

At the present time, there does not exist any analytic non-perturbative theory that is valid for an arbitrary roughness (and non will probably never be invented). The reason for the lack of such general analytic theory is that for strongly rough surfaces higher order scattering processes become important. In consequence, the boundary conditions to be satisfied on the random interface become dominated by non-local effects. This means that the total field on the surface at some point depends on the total field in other locations of the surface. These non-local dependencies hamper the development of analytic theories for strongly (multiple scattering) rough surfaces.

The best technique to resort to for strongly rough surfaces is a rigorous numerical simulation approach [35–37,66,66,67,224]. This approach, to be introduced below, is based on deriving a set of coupled integral equation for the source functions, the field and its normal derivative evaluated on the surface [38,66,68,139,140,224]. With the knowledge of these sources, the total field, and, thus, the solution to the scattering problem, can be obtained from the extinction theorem (Sec. 4.10.1) in any point above the surface.

In addition to this rigorous numerical simulation approach, it ought to be mentioned that another useful approach, though non-rigorous, exists. It is based on the direct solution of the reduced Rayleigh equations satisfied by the system [18,97,98,105,106], and it is particularly useful when the surfaces are weakly, or moderately, rough.

Moreover, for rough, but small-slope surfaces, the so-called Kirchhoff (tangent plane, or physical optics) approximation can be rather useful (and time-saving) [141]. This is a single-scattering approximation used to approximate the unknown source functions of the rigors approach, but without having to perform the computational expensive step of solving the linear system that they satisfy.

4.10.1 The extinction theorem

We will now derive the so-called *Ewald-Oseen extinction theorem* [1,2,4,9] first formulated by P.P. Ewald and C.W. Oseen in the beginning of last century [142–147]. The numerical simulation approach to be presented later in this section will be based directly upon this theorem.

Let us start by recall from Sec. 4.2 that the primary field, $\Phi_\nu(\mathbf{r}|\omega)$, satisfies the wave equation

$$\left[\nabla^2 + \varepsilon(\omega)\frac{\omega^2}{c^2}\right]\Phi_\nu(\mathbf{r}|\omega) = -J_\nu^{ext}(\mathbf{r},\omega), \tag{115}$$

where $\varepsilon(\omega)$ is the dielectric function of the medium where the field is evaluated and $J_\nu^{ext}(\mathbf{r})$ denotes an external source term for the field. In order to solve the scattering problem in question, one may solve this equation in the regions of constant dielectric functions and match the solutions by the boundary conditions that the field, and its (scaled) normal derivative, should satisfy on any interface (see Sec. 3.3). However, it is often more convenient to take advantage of certain integral theorems satisfied by the field, that is a consequence of the wave equation (115), and of which the extinction theorem is one example.

The wave equation (115) is accompanied by a Green's function defined *via* [148]

$$\left[\nabla^2 + \varepsilon(\omega)\frac{\omega^2}{c^2}\right]G(\mathbf{r}|\mathbf{r}';\omega) = -4\pi\,\delta(\mathbf{r}-\mathbf{r}'). \tag{116}$$

Furthermore, we are only interested in out-going solutions to this equation that fulfill the Sommerfeld's radiation condition (at infinity) [149]

$$\lim_{r\to\infty} r\,(\partial_r G - ikG) = 0, \tag{117}$$

where $r = |\mathbf{r}|$.

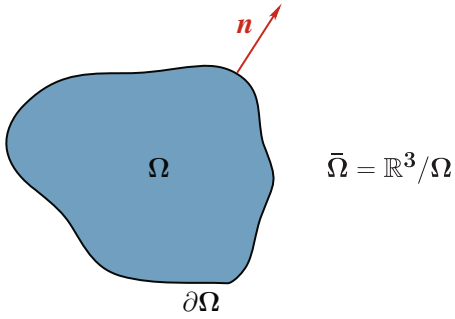

Fig. 9. The geometry considered in the extinction theorem.

In two-dimensions, an explicit representation of the out-going, free space Green's function is provided by [1,148]

$$G(\mathbf{r}|\mathbf{r}';\omega) = i\pi H_0^{(1)}\left(\sqrt{\varepsilon(\omega)}\frac{\omega}{c}\,|\mathbf{r}-\mathbf{r}'|\right), \tag{118}$$

where, $H_0^{(1)}(z)$, is the Hankel-function of the first kind and zeroth-order [90,148] and $\mathbf{r} = (x_1, x_3)$.

Let us start by considering a spatial domain Ω containing a homogeneous, isotropic dielectric medium. This region has a boundary $\partial\Omega$ (Fig. 9). The exterior of the region Ω will be denoted by $\bar{\Omega}$ where its boundary is $\partial\bar{\Omega}$. Notice that $\partial\bar{\Omega}$ includes $\partial\Omega$ in addition to the surface at infinity. We assume that an external source is present somewhere in the external region $\bar{\Omega}$ and that no sources are present within Ω.

If we multiply Eqs. (115) and (116) by, respectively, $G(\mathbf{r}|\mathbf{r}';\omega)$ and $-\Phi_\nu(\mathbf{r}|\omega)$, add the resulting equations, and finally integrate the result over the exterior region $\bar{\Omega}$ we are left with[18] ($\mathbf{r}' \in \bar{\Omega}$)

$$\begin{aligned} &-\frac{1}{4\pi}\int_{\bar{\Omega}} d\mathbf{r}'\left[\Phi_\nu(\mathbf{r}'|\omega)\,\nabla'^{\,2}G(\mathbf{r}'|\mathbf{r};\omega) - \nabla'^{\,2}\Phi_\nu(\mathbf{r}'|\omega)G(\mathbf{r}'|\mathbf{r};\omega)\right] \\ &= -\frac{1}{4\pi}\int_{\bar{\Omega}} d\mathbf{r}' J_\nu^{ext}(\mathbf{r}',\omega)G(\mathbf{r}'|\mathbf{r};\omega) + \begin{cases}\Phi_\nu(\mathbf{r}|\omega), & \mathbf{r}\in\bar{\Omega}\\ 0, & \mathbf{r}\notin\bar{\Omega}\end{cases}. \end{aligned} \tag{119}$$

Since $G(\mathbf{r}'|\mathbf{r};\omega)$ is the out-going free space Green's function the first term of the right hand side is just the incident field due to the source, *i.e.*

$$\frac{1}{4\pi}\int_{\bar{\Omega}} d\mathbf{r}' J_\nu^{ext}(\mathbf{r}',\omega)G(\mathbf{r}'|\mathbf{r};\omega) = \Phi_\nu^{inc}(\mathbf{r}|\omega). \tag{120}$$

This relation holds true independent of $\mathbf{r}$ being located in the exterior ($\bar{\Omega}$) or interior (Ω) region.

Furthermore, by taking advantage of Green's second integral identity that for two well-behaved[19] functions $u(\mathbf{r})$ and $v(\mathbf{r})$ defined on a region V, reads [1,148]

$$\int_V d\mathbf{r}\left[u(\mathbf{r})\nabla^2 v(\mathbf{r}) - v(\mathbf{r})\nabla^2 u(\mathbf{r})\right] = \int_{\partial V} dS\left[u(\mathbf{r})\partial_n v(\mathbf{r}) - v(\mathbf{r})\partial_n u(\mathbf{r})\right], \tag{121}$$

where ∂_n denotes the *outward* normal derivative to ∂V, Eq. (119) can be written as

$$\Phi_\nu^{inc}(\mathbf{r}|\omega) + \frac{1}{4\pi}\int_{\partial\Omega} dS'\left[\Phi_\nu(\mathbf{r}'|\omega)\partial_{n'}G(\mathbf{r}|\mathbf{r}';\omega) - \partial_{n'}\Phi_\nu(\mathbf{r}'|\omega)G(\mathbf{r}|\mathbf{r}';\omega)\right] = \begin{cases}\Phi_\nu(\mathbf{r}|\omega), & \mathbf{r}\in\bar{\Omega}\\ 0, & \mathbf{r}\notin\bar{\Omega}\end{cases}, \tag{122}$$

[18] We have here interchanged $\mathbf{r}$ and $\mathbf{r}'$ for later convenience.

[19] By well-behaved we here mean functions that at least are differential two times.

where dS' is a surface element. In writing Eq. (122) we have explicitly used the fact that the portion of the surface integral over $\partial\bar{\Omega}$, that corresponds to the surface at infinity vanishes due to Sommerfeld's radiation condition satisfied by $G(\mathbf{r}|\mathbf{r}';\omega)$. Hence, the only surface left in the surface integral is $\partial\Omega$ as indicated in the above equation. In addition we have also utilized the relation $\partial_n = -\partial_{\bar{n}}$ for the *outward* normal derivative to the region Ω, while $\partial_{\bar{n}}$ is the outward normal derivative for the same surface, but for region $\bar{\Omega}$. Notice that the incident field term is present due to the fact that the region $\bar{\Omega}$ contains a source. If this region is source-less, this term is missing.

Eq. (122) with the right-hand-side set to zero is the extinction theorem. It is so named because the incident field is extinguished in region Ω by the induced field as represented by the second term of the left-hand-side of this equation. Furthermore, Eq. (122) with $\mathbf{r} \in \Omega$ expresses the fact that the field at any point outside Ω can be found by performing a surface integral over $\partial\Omega$. In order to do so, however, the total field and its (scaled) normal derivative on the surface $\partial\Omega$ has to be known. Hence, the scattering problem is equivalent to finding the field and the (scaled) normal derivative on the surface.

The scattered and transmitted fields

From the above discussion, we learned that the essential quantities to look for is the field and its (scaled) normal derivative evaluated on the surface. We will now see how these two quantities can be calculated by taking advantage of the extinction theorem. This is done by applying Eq. (122) in turn to the different regions naturally defined by the scattering geometry as the regions of constant dielectric properties. For the scattering system depict in Fig. 8 this means to apply Eq. (122) separately to the regions $x_3 > \zeta_1(x_1)$ and $x_3 < \zeta_2(x_1)$. The result is[20]

$$\theta(x_3 - \zeta(x_1))\Phi_\nu^+(\mathbf{r}) = \Phi_\nu^{inc}(\mathbf{r}) + \frac{1}{4\pi}\int dx_1'\, \gamma(x_1') \times \left[\Phi_\nu^+(\mathbf{r}')\partial_{n'}G_+(\mathbf{r}|\mathbf{r}') - \partial_{n'}\Phi_\nu^+(\mathbf{r}')G_+(\mathbf{r}|\mathbf{r}')\right]\big|_{x_3'=\zeta(x_1')}, \quad (123a)$$

and

$$\theta(\zeta(x_1) - x_3)\Phi_\nu^-(\mathbf{r}) = -\frac{1}{4\pi}\int dx_1'\, \gamma(x_1')\left[\Phi_\nu^-(\mathbf{r}')\partial_{n'}G_-(\mathbf{r}|\mathbf{r}') - \partial_{n'}\Phi_\nu^-(\mathbf{r}')G_-(\mathbf{r}|\mathbf{r}')\right]\big|_{x_3'=\zeta(x_1')}. \quad (123b)$$

where the superscripts $\pm$ indicate solutions to the wave equation (115) in regions of dielectric function $\varepsilon_\pm(\omega)$. Furthermore, we have defined

$$\partial_n = \frac{\partial_{x_3} - \zeta'(x_1)\partial_{x_1}}{\gamma(x_1)}, \quad (124a)$$

where

$$\gamma(x_1) = \sqrt{1 + [\zeta'(x_1)]^2}. \quad (124b)$$

In writing Eqs. (123) we have taken advantage of the assumption made earlier that the surface, $\zeta(x_1)$, is a single-valued function of x_1 so that its surface element becomes

$$dS = \gamma(x_1)dx_1. \quad (125)$$

If this assumption does not hold true, the discussion becomes considerably more difficult. A treatment of this case can be found in, *e.g.*, Refs. [45,62,63]. However, we will here not consider this possibility further.

[20] In these equations, and some to come, we have suppressed an explicit reference to the frequency of the incident light in order to make the formulae more compact.

Notice that the integral equations (123) are uncoupled. However, by taking into account the boundary conditions to be satisfied on the rough surface $x_3 = \zeta(x_1)$, *i.e.*

$$\Phi_\nu^+(x_1, x_3; \omega)\big|_{x_3=\zeta(x_1)} = \Phi_\nu^-(x_1, x_3; \omega)\big|_{x_3=\zeta(x_1)}\,, \tag{126a}$$

$$\left.\frac{\partial_n \Phi_\nu^+(x_1, x_3; \omega)}{\kappa_\nu^+(\omega)}\right|_{x_3=\zeta(x_1)} = \left.\frac{\partial_n \Phi_\nu^-(x_1, x_3; \omega)}{\kappa_\nu^-(\omega)}\right|_{x_3=\zeta(x_1)}\,, \tag{126b}$$

the two integral equations will be coupled, and Eqs. (123) take on the form

$$\theta(x_3 - \zeta(x_1))\Phi_\nu^+(\mathbf{r}|\omega) = \Phi_\nu^{inc}(\mathbf{r}|\omega) + \int dx_1' \left[A_+(\mathbf{r}|x_1'; \omega)\mathcal{F}_\nu(x_1'|\omega) - B_+(\mathbf{r}|x_1'; \omega)\mathcal{N}_\nu(x_1'|\omega)\right], \tag{127a}$$

$$\theta(\zeta(x_1) - x_3)\Phi_\nu^-(\mathbf{r}|\omega) = -\int dx_1' \left[A_-(\mathbf{r}|x_1'; \omega)\mathcal{F}_\nu(x_1'|\omega) - \frac{\kappa_\nu^-(\omega)}{\kappa_\nu^+(\omega)} B_-(\mathbf{r}|x_1'; \omega)\mathcal{N}_\nu(x_1'|\omega)\right], \tag{127b}$$

where the symbols $\kappa_\nu^\pm(\omega)$ have been defined previously in Eq. (38d). Here we have introduced the source functions[21]

$$\mathcal{F}_\nu(x_1|\omega) = \Phi_\nu^+(x_1, x_3|\omega)\big|_{x_3=\zeta(x_1)}\,, \tag{128a}$$

$$\mathcal{N}_\nu(x_1|\omega) = \gamma(x_1)\partial_n \Phi_\nu^+(x_1, x_3|\omega)\big|_{x_3=\zeta(x_1)}\,, \tag{128b}$$

as well as the kernels

$$A_\pm(\mathbf{r}|x_1'; \omega) = \frac{1}{4\pi}\,\gamma(x_1')\,\partial_{n'} G_\pm(x_1, x_3|x_1', x_3')\Big|_{x_3'=\zeta(x_1')}\,, \tag{129a}$$

$$B_\pm(\mathbf{r}|x_1'; \omega) = \frac{1}{4\pi}\,G_\pm(x_1, x_3|x_1', x_3')\Big|_{x_3'=\zeta(x_1')}\,. \tag{129b}$$

Notice that the second term on the right-hand-side of Eq. (127a) represents the field scattered from the rough surface, $\Phi_\nu^{sc}(\mathbf{r}|\omega)$. By substituting the following Fourier representation for the Green's function [90]

$$G_+(\mathbf{r}|\mathbf{r}'; \omega) = \int_{-\infty}^{\infty} \frac{dq}{2\pi} \frac{2\pi i}{\alpha_+(q, \omega)}\, e^{iq(x_1 - x_1') + i\alpha_+(q,\omega)|x_3 - x_3'|}, \tag{130}$$

into Eqs. (129), and the resulting expression into Eq. (127a), we find that the scattered field far above the surface, $x_3 \gg \zeta(x_1)$, can be written as

$$\Phi_\nu^{sc}(\mathbf{r}|\omega) = \int_{-\infty}^{\infty} \frac{dq}{2\pi}\, R_\nu(q, \omega) e^{iqx_1 + i\alpha_+(q,\omega)x_3}, \tag{131a}$$

where the scattering amplitude is given by the following expression

$$R_\nu(q, \omega) = \frac{i}{2\alpha_+(q, \omega)} \int_{-\infty}^{\infty} dx_1\, e^{-iqx_1 - i\alpha_+(q,\omega)\zeta(x_1)} \left[i\left\{q\zeta'(x_1) - \alpha_+(q, \omega)\right\}\mathcal{F}_\nu(x_1) - \mathcal{N}_\nu(x_1)\right]. \tag{131b}$$

[21] Notice that the operator $\gamma(x_1)\partial_n$ appearing in $\mathcal{N}_\nu(x_1|\omega)$ is nothing but the *unnormalized* normal derivative.

In these expressions $\alpha_+(q,\omega)$, and later to be used $\alpha_-(q,\omega)$, are defined as in Eqs. (51) and (53).

If the medium occupying the region $x_3 < \zeta(x_1)$ is transparent, a transmitted field will also exist. It is given by the right-hand-side of Eq. (127b). Under this assumption, a Fourier representation for $G_-(\mathbf{r}|\mathbf{r}';\omega)$, equivalent the one given in Eq. (130), will give a transmitted field in the region $x_3 \ll \zeta(x_1)$ of the form

$$\Phi_\nu^{tr}(\mathbf{r}|\omega) = \int_{-\infty}^{\infty} \frac{dq}{2\pi}\, T_\nu(q,\omega) e^{iqx_1 - i\alpha_-(q,\omega)x_3}, \tag{132a}$$

where the transmission amplitude is defined as

$$T_\nu(q,\omega) = -\frac{i}{2\alpha_-(q,\omega)} \int_{-\infty}^{\infty} dx_1\, e^{-iqx_1 + i\alpha_-(q,\omega)\zeta(x_1)} \times \left[i\left\{q\zeta'(x_1) + \alpha_-(q,\omega)\right\} \mathcal{F}_\nu(x_1) - \frac{\kappa_\nu^-(\omega)}{\kappa_\nu^+(\omega)} \mathcal{N}_\nu(x_1) \right]. \tag{132b}$$

The equations for the source functions

In order to solve the scattering problem we see from Eq. (131b) that we need to know the source functions $\mathcal{F}_\nu(x_1|\omega)$ and $\mathcal{N}_\nu(x_1|\omega)$. The question therefore is: How to calculate these source functions? A coupled set of equations for these sources are most easily obtained by setting $x_3 = \zeta(x_1) + \eta$, with $\eta \to 0^+$, in Eqs. (127). Doing so results in the following set of inhomogeneous, coupled integral equations for the sources

$$\mathcal{F}_\nu(x_1) = \mathcal{F}_\nu^{inc}(x_1) + \int dx_1' \left[\mathcal{A}_+(x_1|x_1')\mathcal{F}_\nu(x_1') - \mathcal{B}_+(x_1|x_1')\mathcal{N}_\nu(x_1') \right], \tag{133a}$$

$$0 = \int dx_1' \left[\mathcal{A}_-(x_1|x_1')\mathcal{F}_\nu(x_1') - \frac{\kappa_\nu^-}{\kappa_\nu^+} \mathcal{B}_-(x_1|x_1')\mathcal{N}_\nu(x_1') \right], \tag{133b}$$

where the kernels are defined as

$$\mathcal{A}_\pm(x_1|x_1') = \lim_{\eta\to 0^+} A_\pm(\mathbf{r}|x_1')|_{x_3=\zeta(x_3)+\eta}, \tag{134a}$$

$$\mathcal{B}_\pm(x_1|x_1') = \lim_{\eta\to 0^+} B_\pm(\mathbf{r}|x_1')|_{x_3=\zeta(x_3)+\eta}. \tag{134b}$$

In order to solve Eqs. (133), the integral equations are converted into matrix equations by discretizing the spatial variables x_1 and x_1' and using a suitable quadrature scheme for approximating the integrals that they contain [140]. First, the infinitely long surface is restricted to a finite length L_1, so that the spatial integration range from $-L_1/2$ to $L_1/2$. Second, a grid defined according to

$$\xi_n = [x_1]_n \;=\; -\frac{L_1}{2} + \left(n - \frac{1}{2}\right)\Delta\xi, \qquad n = 1,2,3,\ldots,N, \tag{135}$$

with $\Delta\xi = L_1/N$ is introduced for x_1'. If we assume that the source functions are slowly varying functions over a grid cell (of size $\Delta\xi$), they can be considered as constant over this distance and therefore put outside the integral. The integral equations (133) are thus converted into the following matrix equation by putting $x_1 = \xi_m$

$$\mathcal{F}_\nu(\xi_m) = \mathcal{F}_\nu^{inc}(\xi_m) + \sum_{n=1}^{N} \left[\mathcal{A}_{mn}^+ \mathcal{F}_\nu(\xi_n') - \mathcal{B}_{mn}^+ \mathcal{N}_\nu(\xi_n') \right], \tag{136a}$$

$$0 = \sum_{n=1}^{N} \left[\mathcal{A}^{-}_{mn} \mathcal{F}_\nu(\xi'_n) - \frac{\kappa^{-}_\nu}{\kappa^{-}_\nu} \mathcal{B}^{-}_{mn} \mathcal{N}_\nu(\xi'_n) \right], \tag{136b}$$

where $\mathcal{F}^{inc}_\nu(\xi_m)$ is defined from Eq. (128a) by using $\Phi^{inc}_\nu(x_1, x_3|\omega)$ for the field $\Phi^{+}_\nu(x_1, x_3|\omega)$. Moreover, the matrix elements $\mathcal{A}^{\pm}_{mn}$ and $\mathcal{B}^{\pm}_{mn}$ are defined as

$$\mathcal{A}^{\pm}_{mn} = \int_{\xi_n - \Delta\xi/2}^{\xi_n + \Delta\xi/2} dx'_1 \, \mathcal{A}_{\pm}(\xi_m|x'_1), \tag{137a}$$

and

$$\mathcal{B}^{\pm}_{mn} = \int_{\xi_n - \Delta\xi/2}^{\xi_n + \Delta\xi/2} dx'_1 \, \mathcal{B}_{\pm}(\xi_m|x'_1). \tag{137b}$$

It should be kept in mind that these matrix elements are related to the Hankel function, $H^{(1)}_0(z)$, and its derivative, through the (two-dimensional) Green's function that enters via Eqs. (129) and (134). Care has to be taken when evaluating these matrix elements since the Hankel functions are singular when their arguments vanish. Hence the kernels, $\mathcal{A}_{\pm}(x_1|x'_1)$ and $\mathcal{B}_{\pm}(x_1|x'_1)$, are also singular when $x_1 = x'_1$. Fortunately these singularities are integrable so that the matrix elements, $\mathcal{A}^{\pm}_{mn}$ and $\mathcal{B}^{\pm}_{mn}$, in contrast to the kernels, are well defined everywhere. The somewhat technical procedure for showing this is presented in Appendix (A) from where we obtain that (see Eqs. (A.11) and (A.12)) [38,66,68,139,167],

$$\mathcal{A}^{\pm}_{mn} = \begin{cases} \Delta\xi \, A_{\pm}(\xi_m|\xi_n), & m \neq n, \\ \dfrac{1}{2} + \Delta\xi \, \dfrac{\zeta''(x_m)}{4\pi\gamma^2(\xi_m)}, & m = n, \end{cases} \tag{138a}$$

and

$$\mathcal{B}^{\pm}_{mn} = \begin{cases} \Delta\xi \, B_{\pm}(\xi_m|\xi_n), & m \neq n \\ -\dfrac{i}{4}\Delta\xi \, H^{(1)}_0\left(\sqrt{\varepsilon_\pm}\dfrac{\omega}{c}\dfrac{\gamma(\xi_m)\Delta\xi}{2e}\right), & m = n. \end{cases} \tag{138b}$$

The matrix equations (136), together with the expressions for the matrix elements Eqs. (138), can readily be put onto the computer and solved by standard techniques from linear algebra [94,150] in order to obtain the source functions. With these source functions available, the scattering amplitude, and, if defined, the transmission amplitude, can be obtained from Eqs. (131b) and (132b), respectively. These amplitudes are again related to physical observable quantities, like the mean differential reflection or transmission coefficients, as discussed earlier. Hence the scattering problem is in principle solved!

In passing we note that it was by the method described in this section that the speckle pattern shown in Fig. 2 was produced. After first solving Eqs. (136) to obtain the source function (on the surface), $\mathcal{F}_\nu(\xi_n)$ and $\mathcal{N}_\nu(\xi_n)$, Eqs. (127) were used to calculate the field everywhere in the geometry. Notice that Eqs. (127) only require a straight forward spatial integration along the surface in order to obtain the field at an arbitrary spatial point once the source functions are known. Even if these integrals are readily evaluated, it might be a somewhat time-consuming calculation if one wants to make a contour map like in Fig. 2 (many spatial points), because the Green's functions are relatively costly to calculate. Fortunately, in such cases, one may tabulate the Green's function and use a look-up tables and/or make the code run in parallel in which case a significant speed-up can be expected.

It should also be mentioned that the approach presented here can be generalized to more complicated scattering geometries like film systems etc. [38,68,139,167]. However, in such cases a higher demand is put on the computational resources since the size is increased of the underlying matrix system that determines the source functions.

The surface integral technique presented in this section can also be used where the interfaces of the problem at hand is not everywhere described by a mathematical function. In such cases

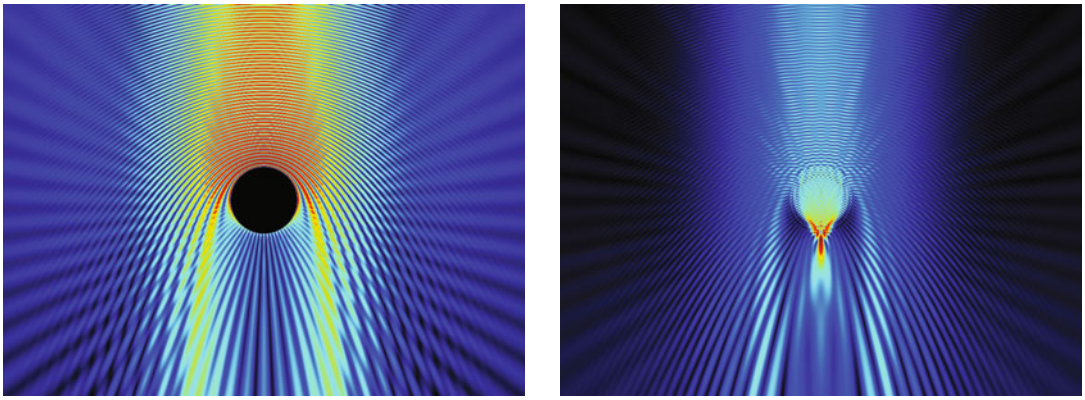

Fig. 10. Contour plots of the intensity of the light scattered by a (left) metal [$\varepsilon(\omega) = -17$] and (right) glass [$\varepsilon(\omega) = 2.25$] cylinder placed in vacuum ($\varepsilon_0 = 1$). Light of p-polarization and wavelength $\lambda = 405\,\mathrm{nm}$ was incident on the cylinder from above in the form of a beam of width $w = 15\lambda$. The radius of the circular cross-sections of the cylinders was $R = 5\lambda$. The surfaces were discretized by $N = 1901$ points. The color scale is defined so that red corresponds to high intensity and blue to low (and black to zero intensity). (After Ref. [45].)

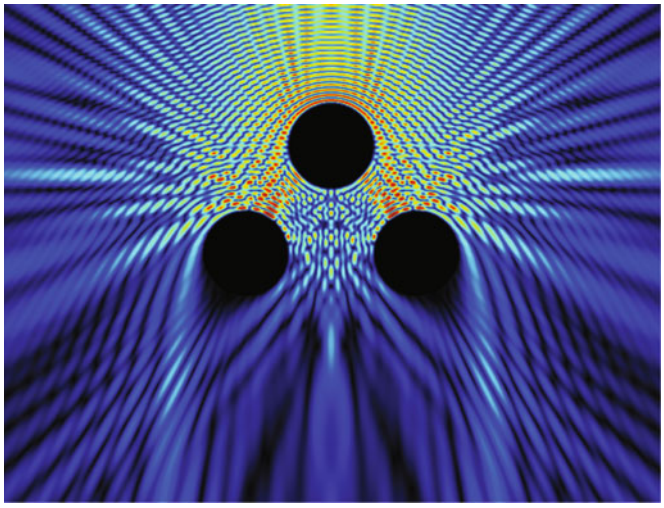

Fig. 11. The same as the left panel of Fig. 10, but now the scattering geometry consists of three identical metal cylinders arranged in an equilateral triangular pattern in vacuum. Note, in particular, the complex interference pattern in the gap between the cylinders. (After Ref. [45].)

the initial integration over the surface cannot be converted into an integration over x_1 like was done in Eq. (125). Instead one must keep the original integration over the surface by taking advantage of a parametric representation of the interface. We will not go into this here, but instead refer the interested reader to the literature [45,62,63]. Moreover, we in Figs. 10 and 11 present some simulation results that can be obtained for the scattered field by using the surface integral technique.

4.10.2 Remarks on the accuracy of the numerical simulation approach

The numerical approach described above is formally exact since *no* approximations have been introduced. It is therefore in principle applicable to scattering from surfaces of any roughness. It has proven useful in many situations, and serve today as a standard, and invaluable, tool for

rough surface scattering studies. This is in particular true for scattering from strongly rough surfaces where it represents the only rigorous available method at present.

Even if this approach is formally exact, it has some practical limitations. Imagine a weakly rough metal surface that is illuminated by p-polarized light. In this case the incident light can excite surface plasmon polaritons that will propagate along the rough surface. The mean free path of these surface plasmon polaritons can rather long for weakly rough surfaces.

In computer simulations we are not able to represent infinitely long surfaces due to the limited amount of computer memory. Instead we are restricted to surfaces of finite length. To avoid essential contributions to the simulation results from artificial scattering processes, like edge effects,[22] the length of the surfaces needs to be long. In order not to compromise the spatial resolution used in the simulations, big demands on computer memory and CPU-time is a consequence. This sets a practical limit for the use of rigorous numerical simulations for weakly rough surfaces. However, for such kind of roughness, perturbation theory, where we by construction are using surfaces of infinite length, are adequate and accurate as discussed earlier. The present limitation of the rigorous numerical simulation approach should therefore not represent a too severe restriction from a practical point of view.

In the introduction to Sec. 4.10, it was mentioned that non-rigorous numerical simulations can be based directly on the reduced Rayleigh equation (Sec. 4.5). The advantage of using a non-rigorous, over a rigorous, approach is that the former approach can handle *much* longer surfaces than the latter with the same use of computer memory [97,98]. Hence, the numerical solution of the reduced Rayleigh equation approach has the potential of reducing edge effects that are important for weakly rough surfaces supporting surface waves. The accuracy of this non-rigorous approach is obviously restricted to surfaces for which the Rayleigh hypothesis is valid. Therefore, it can not be applied to surfaces of arbitrary roughness, but it is valid for surfaces that practically can not be treated within perturbation theory. A direct numerical solution of the reduced Rayleigh (integral) equation can, therefore, be looked upon as bridging the gap between perturbation theory and rigorous numerical simulations.

5 Physical phenomena in electromagnetic wave scattering from randomly rough surfaces

Wave scattering from randomly rough surfaces has a long history in science [16,17,19,20]. In the overall majority of theoretical studies conducted up to the early 1980s, single-scattering approaches were used [25–30,32–39,41]. However, around this time scientists started to get interested in the effects and consequences of incorporating multiple-scattering events into the theories. It created a lot of excitement in the field when new and interesting multiple scattering phenomena were either predicted theoretically and/or observed in experiments. During the period of time that has passed since the early 1980s, multiple scattering effects from randomly rough surfaces have attracted much attention from theorists and experimentalists alike, and today the research in this field is concentrated mainly around different kinds of multiple scattering effects and various inverse scattering problems [33–41].

It ought to be mentioned that several of the effects that will be discussed in this section are not unique to surface scattering. In fact, several of them have their analogies in light scattering from volume disordered systems [12,27,28,151–153].

In the present section, we aim at discussing some of the new multiple scattering effects that might take place when electromagnetic waves are scattered from a randomly rough surface. The technical details on which the present section rely, were mainly outlined in the previous section, so unnecessary technical details have here been avoided whenever possible. Hence, most of the presentation is keep at a phenomenological, and hopefully pedagogical, level. However, as a service to the more technical oriented readers, an extensive reference to the original literature has been made.

[22] Edge effects may become important when, for instance, surface plasmon polaritons are scattered from the edges of our (finite length) surface.

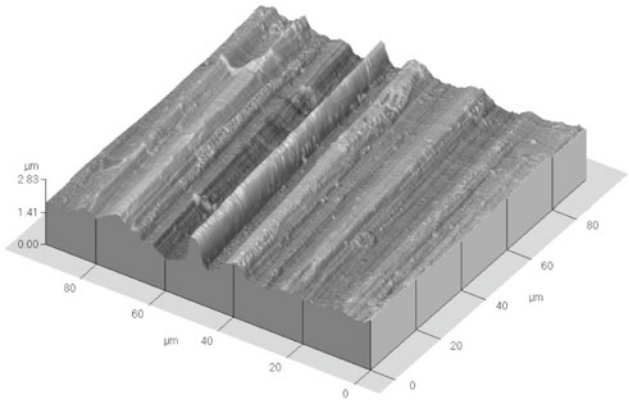

Fig. 12. An atomic force microscopy (AFM) image (512×512 pixels) of a cold-rolled aluminum alloy sheet. Notice the pronounced anisotropy of the surface due to the rolling process under which it was manufactured. The direction of the grooves is along the rolling direction. From the AFM topography data it was shown that this surface shows self-affine scaling over three orders of magnitude ranging in scale from 50 nm up to 50 μm. The Hurst exponents were found to be $H = 0.80 \pm 0.05$ perpendicular to the rolling direction, and $H \approx 0.5$ along it. (After Ref. [75].)

5.1 Scattering from self-affine surfaces

Even though the overall majority of material that will be discussed in this section will be devoted to multiple scattering effects, we will start by presenting some results where single-scattering often is adequate for the description of the phenomenon and where analytic results can be obtained. Moreover, this example partly serves to show that single scattering theories can still give rather interesting and non-trivial results.

In Sec. 2.2 we introduced the concept of self-affine surfaces. Such surface are abundant in nature, and can be found in both natural and man-made systems [77,154–158,160,161]. For instance, the surface of fractured silica glass is self-affine [158], and the same applies to the surfaces produced by fracturing many other materials [155,159]. A specific example of a man-made system that shows self-affine scaling is a cold-rolled aluminum plate (alloy sheet) [75] (Fig. 12).

Self-affine surfaces show so-called *scale invariance* (Sec. 2.2), and this invariance is characterized by the Hurst (or roughness) exponent, H ($0 < H < 1$). To see what this means, let us consider two distinct points at the surface, say, $(x_1, \zeta(x_1))$ and $(x_1', \zeta(x_1'))$. The lateral separation between these two points is $\Delta x_1 = x_1 - x_1'$, and the vertical separation is $\Delta\zeta(\Delta x_1) = \zeta(x_1) - \zeta(x_1')$. Assume now that the lateral separation is changed, *i.e.* rescaled, so that $\Delta x_1 \to \Lambda\Delta x_1$, where $\Lambda > 0$ is a positive constant. What is then known about the vertical height difference, $\Delta\zeta(\Lambda\Delta x_1)$? If the surface is self-affine, it then follows from the defining properties of a self-affine surface, Eq. (15), that

$$\Delta\zeta(\Lambda\Delta x_1) \simeq \Lambda^H \, \Delta\zeta(\Delta x_1), \tag{139}$$

where $\simeq$ is used to indicate "being statistical equal to". So changing (or rescaling) the lateral separation from Δx_1 to $\Lambda\Delta x_1$ with a suitable choice for Λ, has the consequence that the vertical height difference is changed from $\Delta\zeta(\Delta x_1)$ to $\Lambda^H\Delta\zeta(\Delta x_1)$ if the surface $x_3 = \zeta(x_1)$ is self-affine. In other words, if one knows the properties of the surface at *one single* length scale, then the properties at *all other* length-scales for which the surface respects self-affine scaling can be obtained by a trivial rescaling according to Eq. (139). This is the essence of scale-invariance, and this concept is rather powerful as will be seen below.

An important length-scale for self-affine surfaces is the so-called topothesy, ℓ. It signifies the (lateral) scale below which the surface shows fractal properties (and above, non-fractal) [77]. From the knowledge of H and ℓ (as well as the upper and lower cutoffs of the scaling regime, $\xi_\pm$), many of the important physical properties of the systems can be inferred.

We will now look into what consequence the knowledge of a surface being self-affine (and therefore scale-invariant) has on the angular distribution of the light scattered from it. For simplicity, we will in the following consider the scattering from a perfect electric conductor (PEC) and we will assume that the incident light is s-polarized. Under these assumptions, the scattering problem can be solved in close form within a single scattering (Kirchhoff) approximation [141]. This is achieved by taking advantage of $R(q|k)$ being expressed in closed form within the Kirchhoff approximation and that the average, $\langle |R(q|k)|^2 \rangle$, can be calculated analytically since the probability distribution function, $p(\Delta\zeta, \Delta x_1)$, of a height difference $\Delta\zeta$ over an window Δx_1 is known analytically (see Eq. (19)) for a self-affine surface. The detailed derivation of the expression for the mean differential reflection coefficient is given in Refs. [162,163], and it reads

$$\left\langle \frac{\partial R_s}{\partial \theta_s} \right\rangle = \frac{a^{-(\frac{1}{H}-1)}}{\sqrt{2}\cos\theta_0} \frac{\cos\frac{\theta_s+\theta_0}{2}}{\cos^3\frac{\theta_s-\theta_0}{2}} \mathcal{L}_{2H}\left(\frac{\sqrt{2}\tan\frac{\theta_s-\theta_0}{2}}{a^{\frac{1}{H}-1}} \right), \tag{140a}$$

with

$$a = \sqrt{2}\frac{\omega}{c}\ell \cos\frac{\theta_s+\theta_0}{2}\cos\frac{\theta_s-\theta_0}{2}, \tag{140b}$$

where, θ_s and θ_0, as usual, denote the angles of scattering and incidence, respectively. In writing Eq. (140a), the centered symmetrical Lévy stable distribution [164] of exponent α was introduced

$$\mathcal{L}_\alpha(x) = \frac{1}{2\pi}\int_{-\infty}^{\infty} dk\, e^{ikx} e^{-|k|^\alpha}. \tag{141}$$

It should be noticed that in Eqs. (140) the wavelength of the incident light, $\lambda = 2\pi/(\omega/c)$, only enters *via* the combination $(\ell/\lambda)^{1-\frac{1}{H}}$ which appears both in the prefactor and in the argument of the Lévy distribution. This quantity can be geometrically regarded as $s(\lambda)^{1/H}$ where $s(\Delta x_1) = (\ell/\Delta x_1)^{1-H}$ is the typical slope of the surface over the length scale Δx_1. The behavior of the scattered intensity is thus entirely determined by this typical slope over a wavelength, $s(\lambda)$, and the roughness exponent H. Moreover, it can be demonstrated that the features of the scattered intensity is strongly dependent on these parameters indicating a clear "self-affine footprint" in the scattered intensity.

The analytic expression for the mean differential reflection coefficient of a self-affine surface, Eq. (140a), was obtained within a single-scattering approximation (the Kirchhoff approximation). Hence, it is important to know how well such an approximation can represent the angular intensity distribution of the light scattered from a self-affine surface.

To look into this, we in Figs. 13 compare the prediction of Eqs. (140) for the mean differential reflection coefficient for a self-affine surface (dashed lines), to what can be obtained from rigorous computer simulations (solid lines) and experimental measurements (open symbols). The experimental measurements were performed on an industrially cold-rolled aluminum plate similar to what is shown in Fig. 12. The wavelength of the light used in the experiments was $\lambda = 0.6328\mu$m at which wavelength the dielectric function of aluminum is $\varepsilon(\omega) = -56.15 + i20.92$ [165]. Prior to the optical measurements the surface topography was characterized by AFM measurements and found to show (anisotropic) self-affine scaling consistent with a Hurst exponent $H = 0.80 \pm 0.05$ perpendicular to the rolling direction and $H \approx 0.5$ along it [160,166]. Moreover, the slope (over a wavelength) was found to be $s(\lambda) = 0.11 \pm 0.01$ which corresponds to a topothesy of about $\ell \approx 4.4 \cdot 10^{-5}\lambda$ [160,166]. In the experiments the incident light illuminated only a thin strip of the surface in a direction perpendicular to the rolling direction (the grooves) of the surface. This was done in order to imitate a one-dimensional roughness.

The results of Figs. 13 indicate that there is a very good agreement between the analytic, numerical and experimental results. For the analytic and numerical results the surface parameters were assumed to be those obtained from the AFM measured topography, *i.e.* $H = 0.80$ and $s(\lambda) = 0.11$. The observed discrepancy between the analytic and numerical/experimental results, mainly caused by neglecting multiple scattering, starts to become significant only for the largest scattering angles where the scattered intensity already is one to two orders of magnitude lower than the maximum value. Hence, the analytic (single-scattering) expression, Eqs. (140), is,

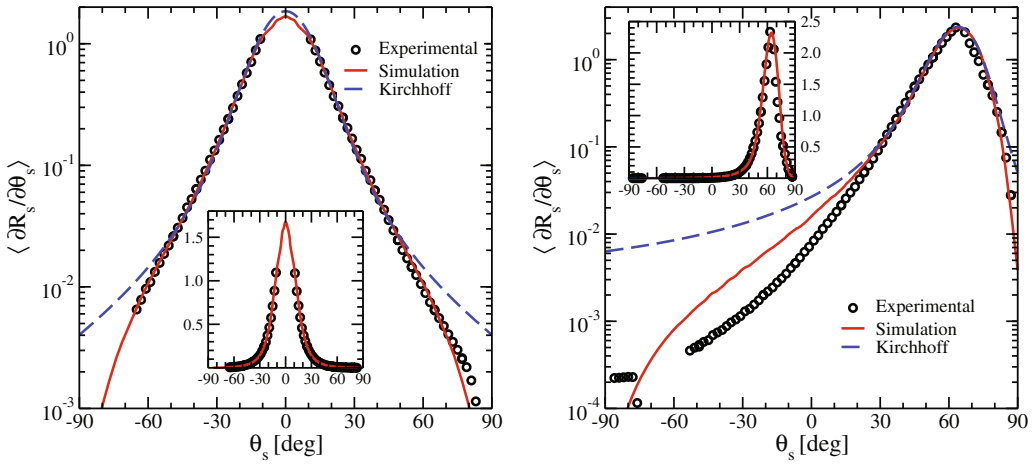

Fig. 13. The mean differential reflection coefficient, $\langle \partial R_s/\partial\theta_s \rangle$, vs. scattering angle, θ_s, for an aluminum self-affine surface of the type shown in Fig. 12 in log-linear (main panels) and linear-linear scales (insets). The incident light, of wavelength $\lambda = 0.6328\,\mu$m, was s-polarized and was incident onto the cold-rolled aluminum surface at angles of incidence (left) $\theta_0 = 0^\circ$ and (right) $\theta_0 = 65^\circ$. The open circles represent the experimental scattering data obtained for the rough aluminum surface. The solid lines are the results of rigorous numerical Monte Carlo simulations for the mean DRC of a self-affine aluminum surface of Hurst exponent, $H = 0.78$, and topothesy, $\ell = 2.79 \times 10^{-11}\,\text{m} = 4.4 \times 10^{-5}\,\lambda$. For the surface length we assumed $L = 63.28\,\mu\text{m} = 100\lambda$ that was discretized at $M = 1024$ evenly distributed points. For the dielectric constant of aluminum at the wavelength of the incident light we used $\varepsilon(\omega) = -56.15 + i20.92$ [165]. The simulation results were obtained by averaging over $N = 1500$ independent surface realizations. For the incident light we used a finite sized beam of half width $g = 6.4\,\mu$m. The dashed lines are the prediction of Eqs. (140) assuming the same roughness parameter and topothesy as for the surfaces used in the rigorous simulations. Notice, since Eqs. (140) assume a perfect conducting surface that the normalization of the simulation results and the analytic approximation differ. Since the experimental data were obtained using arbitrary units, we have adjusted them by a constant amplitude to be able to be compared to the simulation and analytic results. (After Ref. [166].)

at least for the parameters used here, well suited for describing the scattering from a self-affine metallic surface.

It should be noted that the agreement between the rigorous computer simulations and the experimental data is very good. For normal incidence, the agreement covers almost three orders of magnitude in intensity. Given that the surface is an industrially fabricated surface that is not manufactured in a controlled way, the agreement is no less than surprisingly good. Such results may pave the way for using the analytic expression (140) in a successfully, non-contact optical approach to the determination of self-affine parameters like the Hurst exponent and the topothesy. An optical approach to the determination of self-affine parameters, as compared to the more traditional contact approaches [71,77–79], is that the former is fast and can analyze larger surface areas.

5.2 Coherent effects in multiple-scattered fields: Weak localization of light on a randomly rough surface

In 1985, McGurn, Maradudin, and Celli [124] predicted theoretically the existence of what later has been known as the *enhanced backscattering phenomenon* in surface scattering. This phenomenon expresses itself as a well-defined peak in the retroreflection direction of the angular dependence of the light scattered incoherently from a rough surface. The authors of Ref. [124] were the first to report on a multiple scattering effect in the area of electromagnetic rough surface scattering. The enhanced backscattering phenomenon [124,167] is an example of what

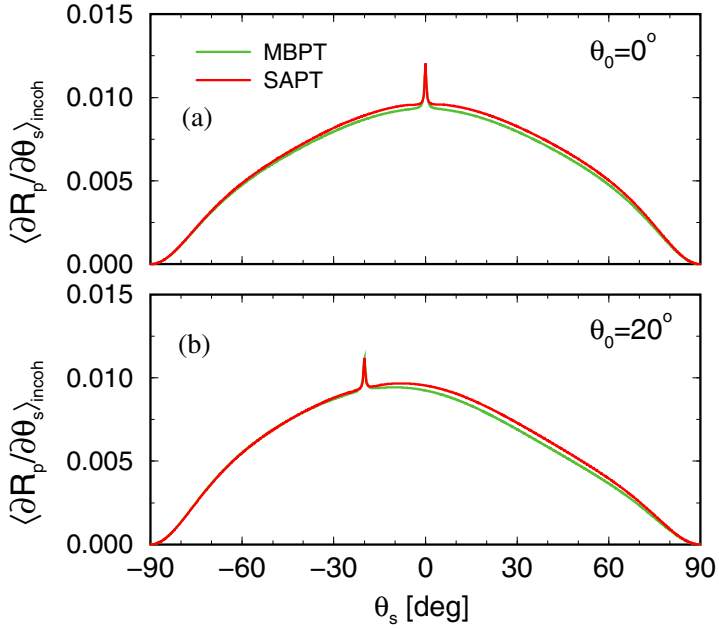

Fig. 14. Perturbative calculations of the mean differential reflection coefficient of the incoherent component of the light scattered from a randomly rough silver surface using small-amplitude perturbation theory (SAPT) and many-body perturbation theory (MBPT). For the SAPT curves, the mean DRC was calculated consistently to 4th order in the surface profile function (*c.f.* Eq. (92a)). The angles of incident of the light of wavelength $\lambda = 457.9\,\text{nm}$ were (a) $\theta_0 = 0^\circ$ and (b) $\theta_0 = 20^\circ$. The dielectric constant of silver at this wavelength is $\varepsilon(\omega) = -7.5 + i0.24$. The surface was characterized by a Gaussian height distribution of rms-height $\delta = 5\text{nm}$ and a Gaussian height-height correlation function of correlation length $a = 100\,\text{nm}$.

is known as a *coherent effect* in the multiple scattered field. Subsequently other coherent phenomena were predicted, like, enhanced transmission [171], enhancements due to the excitations of magnetoplasmons [177,179], satellite peaks [175,176], and enhanced forward scattering [173].

5.2.1 Enhanced backscattering

The backscattering enhancement phenomenon will be discussed fist. Since the mechanisms that give rise to it are different for weakly and strongly rough surfaces, they will be treated separately. The scattering system that will be considered is depicted in Fig. 8 and consists of a single rough vacuum-metal interface.

In 1985, McGurn, Maradudin, and Celli [124] predicted based on a perturbation theoretical study, that also in the retroreflection (anti-specular) direction of the angular dependence of the mean differential reflection coefficient (DRC) there might be an enhancement. This effect, known today as enhanced backscattering, manifest itself as a well-defined peak in the retroreflection direction of the angular dependence of the intensity of the light that has been scattered incoherently from the random surface.

In the original paper of McGurn et al. [124], the calculation of the enhanced backscattering peak was carried out for p-polarized light scattered from a weakly rough silver surface. Their calculations, based on a many-body perturbation theory, took into account multiple scattering events in the calculation of the intensity scattered incoherently by the surface. In Figs. 14 we present perturbative results for the incoherent component of the mean differential reflection coefficient for p-polarized light incident at angles $\theta_0 = 0^\circ$ (Fig. 14(a)) and $\theta_0 = 20^\circ$ (Fig. 14(b)) on a rough silver surface. These results were obtained by using small-amplitude perturbation theory (Sec. 4.6) and many-body perturbation theory (Sec. 4.8). Terms to 4th order in the

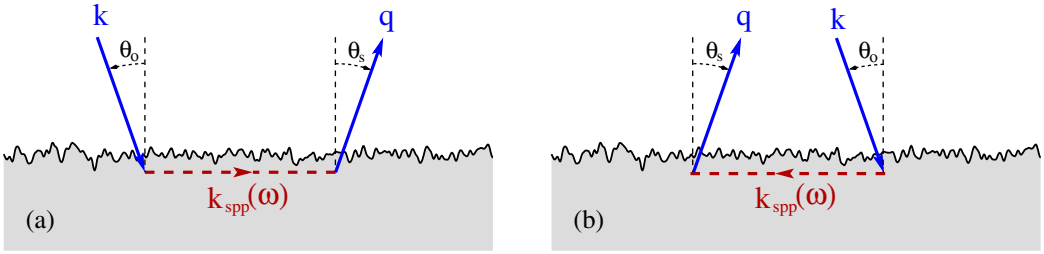

Fig. 15. Diagrams showing two of the scattering events that give rise to the enhanced backscattering peak phenomenon for weakly rough surfaces by interfering constructively.

surface profile function were included for the mean DRC which is enough to include all double scattering processes. The wavelength of the incident light was $\lambda = 457.9$nm, and the dielectric constant of silver at this wavelength is $\varepsilon(\omega) = -7.5 + i0.24$ [165]. The surface was assumed to be characterized by a Gaussian height distribution and the height-height correlation function was also of the Gaussian type. The root-mean-square (rms) height of the surface was $\delta = 5$nm while the correlation length was $a = 100$nm. From Figs. 14 we observe that the two perturbation theories give consistent results, but more importantly, they both produce well-pronounced peaks at the retroreflection directions, $\theta_s = -\theta_0$. It should be stressed that it is the *incoherent* component of the mean DRC that is plotted, so that the peak seen, say, at $\theta_s = 0^\circ$ in Fig. 14(a), is no specular effect[23] since no contributions from specular scattering have been included. That this is indeed the case should be apparent from the position of the enhanced backscattering peak when the angle of incidence is $\theta_0 = 20^\circ$ (Fig. 14(b)).

What is the origin of the enhanced backscattering peak phenomenon? It was quickly realized that it had to be caused by multiple scattering since it had not been seen earlier when using single scattering theories. It turned out that the origin of the effect lies in the interference between a multiple scattered path with its reciprocal partner [65,124]. To illustrate this, let us consider the double scattering path shown in Fig. 15(a). Here an incident wave excites, *via* the roughness, a surface plasmon polariton (SPPs)that propagates along the surface. At the next scattering event this SPP is converted back into a volume electromagnetic wave that propagates away from the surface. This path has a reciprocal partner (Fig. 15(b)) where the scattering takes place from the same scattering centers on the rough surface, but now in the opposite order. For the backscattering direction these two paths will have exactly the same amplitude and phase, *i.e.* they will be coherent, and interfere *constructively* (see Sec. 5.2.3 for mathematical details). However, as we move away from the backscattering direction, the two paths soon become phase incoherent so that their intensities just add. Thus, due to the interference nature of the enhanced backscattering peak, the intensity at the position of the peak should in the absence of single scattering be twice that of its background due to the cross-terms (interference terms) originating from the square modulus of the sum of the amplitudes needed in order to calculate the intensity. However, notice that it is not uncommon that single scattering gives considerable contribution to the mean differential reflection coefficient of the light scattered incoherently from the surface. In such cases, the height of the peak is not twice that of its background.

To show that multiple scattering indeed is the origin of the enhanced backscattering phenomenon, we show in Fig. 16 the different contributions to the incoherent component of the mean DRC obtained from Eq. (92a) that is a result from small-amplitude perturbation theory. We recall that the first term of this equation is the single scattering contribution (the 1–1 term), *i.e.* it is of 2nd order in the surface profile function $\zeta(x_1)$. The next two terms are both double scattering contributions that are 4th order contributions in the surface profile function. The last term in Eq. (92a) contains a single and third order scattering process (the 3–1 term). From Fig. 16 it is seen that the single scattering contribution is a smooth function of the angle of scattering, and the same holds true for the 3–1 term. However, Fig. 16 shows clearly that

[23] Recall that for normal incidence the specular and anti-specular directions coincide.

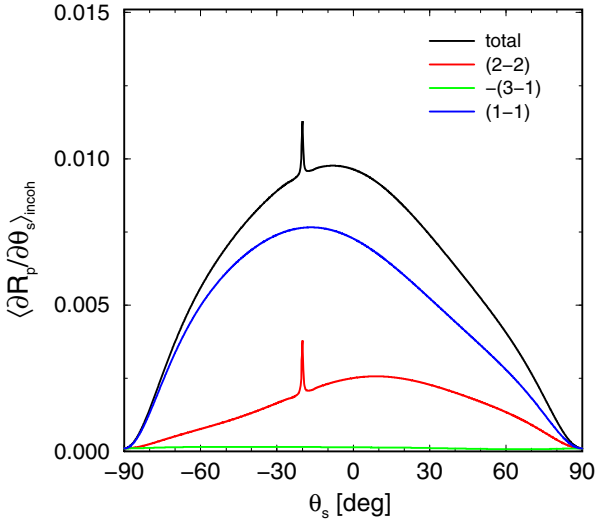

Fig. 16. The same as the SAPT curve from Fig. 14(b), but now in addition to the total (4th order) contribution to the incoherent component of the mean DRC also the separate contributions from Eq. (92a) are included. These contributions are the single scattering 1–1 term, Eq. (92b), the 2–2 double scattering term, Eq. (92c), and finally the (negative of the) 3–1 term, Eq. (92d). Notice that the enhanced backscattering peak comes from the 2–2 term, *i.e.* from the double scattering contribution.

the peak stems from the double scattering contribution (the 2–2 term), *i.e.* it comes from the second and third terms of Eq. (92a). In a diagrammatic language the 2–2 term comes from the maximally crossed diagrams (see *e.g.* Ref. [124]) (see also Refs. [38,181,182]).

It should be noted that even if we earlier only included fully the lowest order multiple scattering process (double scattering), higher order processes will not change the statement that the enhanced backscattering phenomenon is caused by multiple scattering through the constructive interference between a scattering path with its reciprocal partner [108].

The enhanced backscattering effect from weakly rough vacuum-metal surfaces was observed in experiments by West and O'Donnell [65] in 1995 in the scattering of p-polarization light from a rough gold surface of roughness $\delta = 10.9$nm (Figs. 17). The power-spectrum used in these experiments was of the rectangular type also known as the West-O'Donnell power-spectrum (see Eq. (9)). The remaining parameters used in the experiments are defined in the caption of Figs. 17 where also the experimental results are reproduced. For the two smallest angles of incidence well-defined peaks around the retroreflection direction are seen in the experimental results. The reason that no backscattering peak is seen for the largest angle of incidence ($\theta_0 = 18^\circ$) is that the power-spectrum does not allow the incident light to couple to SPPs. Moreover, in Figs. 17 the experimental data are compared to results obtained from small-amplitude and many-body perturbation theory, and satisfactory agreement is observed.

For weakly rough surfaces we just argued that the origin of the enhanced backscattering effect involves surface plasmon polaritons. In s-polarization, a rough (one-dimensional) vacuum-metal interface *cannot* support such surface waves (see Sec. 3.4). Hence, one does not expect to see any backscattering peak for this polarization for weakly rough surfaces. This is indeed seen from Figs. 18 that present numerical simulation results for the incoherent component of the mean DRC for p- and s-polarized incident light obtained on the basis of the solution of the reduced Rayleigh equation satisfied by the scattering amplitude [89,98]. The power spectrum used for the surface roughness was again of the rectangular (West-O'Donnell) type, and it was defined by the parameters $k_- = 0.782(\omega/c)$ and $k_+ = 1.336(\omega/c)$.

From Fig. 18(a) one also observes that the enhanced backscattering peaks do not exist (in p-polarization) for all angles of incidence, *e.g.*, for $\theta_0 = 20^\circ$. For the SPPs mediated multiple scattering process to take place (Figs. 15), it must be possible for the incident light, of lateral wavenumber $k = (\omega/c)\sin\theta_0$, to couple into rightward (+) and/or leftward-propagating (−)

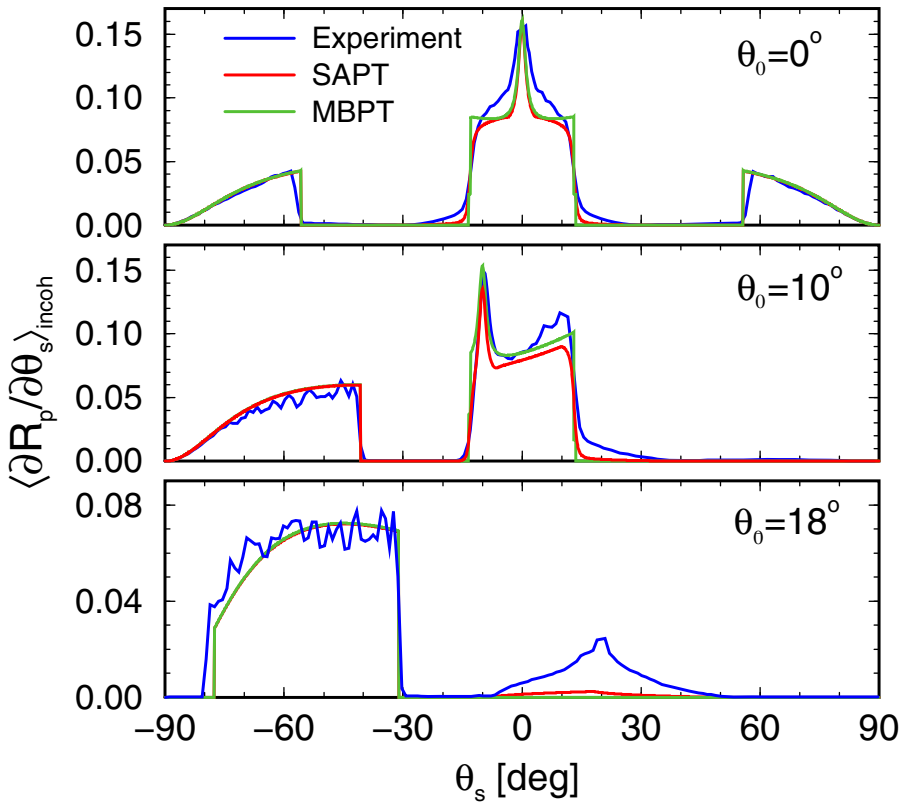

Fig. 17. Experimental results (blue lines) for the incoherent component of the mean differential reflection coefficient, $\langle \partial R_p/\partial\theta_s \rangle_{\rm incoh}$, as a function of the angle of scattering, θ_s. P-polarized light of wavelength $\lambda = 612.7\,$nm was incident on the surface at three different angles of incidence: $\theta_0 = 0^\circ$ (Fig. 17(a)), $\theta_0 = 10^\circ$ (Fig. 17(b)) and $\theta_0 = 18^\circ$ (Fig. 17(c)). The one-dimensional random gold surface ($\varepsilon(\omega) = -9.00 + i1.29$) had a roughness $\delta = 10.9\,$nm and was characterized by a rectangular (West-O'Donnell) power-spectrum of parameters (parameters $k_- = 0.82(\omega/c)$ and $k_+ = 1.29(\omega/c)$. The experimental results are compared to perturbative results obtained by small amplitude perturbation theory (SAPT; red lines) and many-body perturbation theory (MBPT; green lines). (Adapted after Ref. [65].)

SPPs of wavenumber $\pm k_{spp}(\omega)$. From the discussion in Sec. 4 it follows that this is only possible if $g(|\pm k_{spp}(\omega) - k|) \neq 0$, or if the angle of incidence (θ_0) is smaller in absolute value than the *critical* angle

$$\theta_{max} = \sin^{-1}\left(\frac{k_{spp}(\omega) - k_-}{\omega/c}\right). \tag{142}$$

Furthermore, it is straightforwardly shown that only for $|\theta_s| < \theta_{max}$ is out-coupling of SPPs into propagating waves possible. With the parameters assumed in the simulations presented in Figs. 18, one finds $\theta_{\rm max} = 17^\circ$, and this is the reason why no enhanced backscattering peak is seen in Fig. 18a when $\theta_0 = 20^\circ$. For the same reason, but with a slightly different value for θ_{max}, no enhanced backscattering peak was seen in the experimental results, shown in Figs. 17, when $\theta_0 = 18^\circ$. Moreover, the explanation for the rapid drop in intensity of p-polarized scattered light just outside $\theta_s = \pm\theta_{max}$, is that here out-coupling of SPPs into propagating waves is forbidden. For s-polarization (Fig. 18(b)), for which SPPs are not supported by the scattering geometry, there is nothing special about the scattering angles around $\pm\theta_{max}$ (and the mean DRC is smooth), and in particular, no enhanced backscattering peaks are observed.

Figs. 18 also show pronounced increase in the values of $\langle \partial R_\nu/\partial\theta_s \rangle_{incoh}$ for some (large) scattering angles in the range $|\theta_s| > \theta_{max}$ (for $\theta_0 = 0^\circ$ located at $\theta_s = \pm 51.4^\circ$). This has nothing

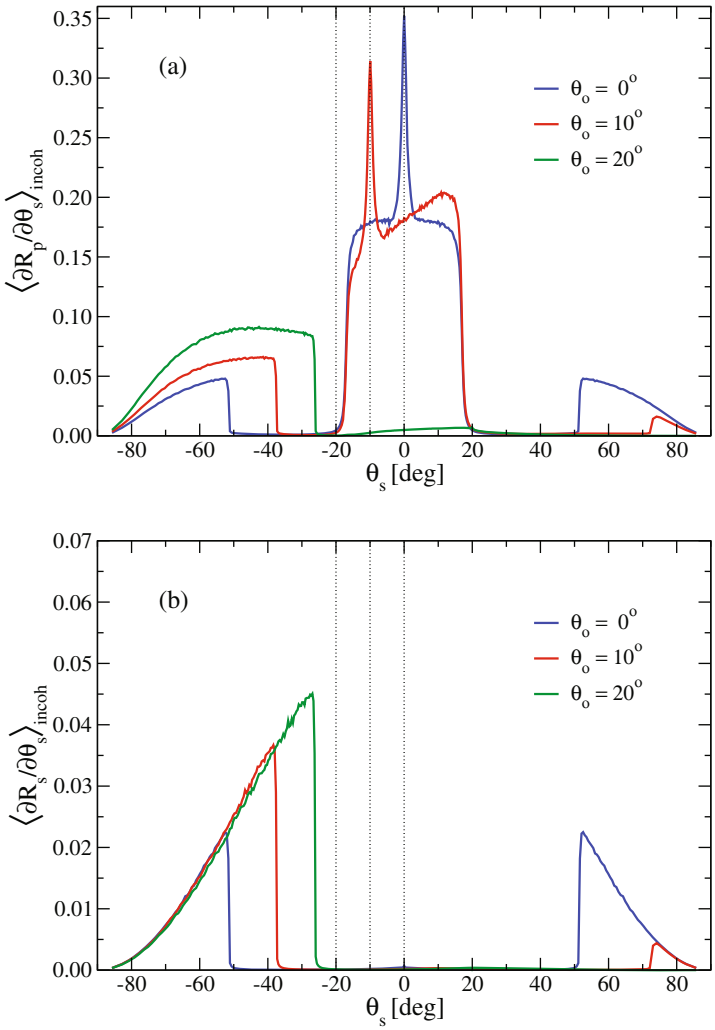

Fig. 18. The incoherent component of the mean differential reflection coefficient, $\langle \partial R_\nu / \partial \theta_s \rangle_{incoh}$, for (a) p- and (b) s-polarized plane wave incident from vacuum on a rough silver surface at wavelength $\lambda = 457.9\,\text{nm}$ ($\varepsilon(\omega) = -7.5 + 0.24i$) and an angle of incidence θ_0 as given by the legends. The rough surface (of length $L = 200\lambda$) had a Gaussian height distribution of rms-height 10 nm, and the a rectangular (West-O'Donnell) power spectrum of parameters $k = 0.782\omega/c$ and $k_+ = 1.366\,\omega/c$. The vertical dotted lines indicate the backscattering directions. The results were averaged over 10,000 realizations of the surface roughness. For p-polarized light, incident at an angle $|\theta_0| < \theta_{\max} = 17°$, the enhanced backscattering peaks are readily observed in the diffusely scattered light. Notice the difference in amplitude between the two sub-figures. (Adapted after Ref. [89].)

to do with SPPs, nor with multiple scattering, but is instead a consequence of single scattering (and the actual power spectrum parameters used). Moreover, this effect is observed for both p- and s-polarization, indicating that SPPs can not be involved. According to Eqs. (92a) and (92b), incident light of lateral wavenumber k and any polarization, can, by single scattering only, be coupled to propagating scattered light of lateral wavenumber q, if, and only if, $g(|q-k|)$ is non-zero. With the power spectrum assumed here this is possible when $|q-k| > k_-$. For instance, when the angle of incidence is $\theta_0 = 10°$, the above relation predicts that single scattering is allowed for angles of scattering for which $\theta_s > 72.8°$ and $\theta_s < -37.4°$. Conversely, in the interval $-37.4° < \theta_s < 72.8°$ single scattering is *forbidden* due to the form (and parameters) of the power spectrum. From Figs. 18, it is observed that it is just outside this angular interval

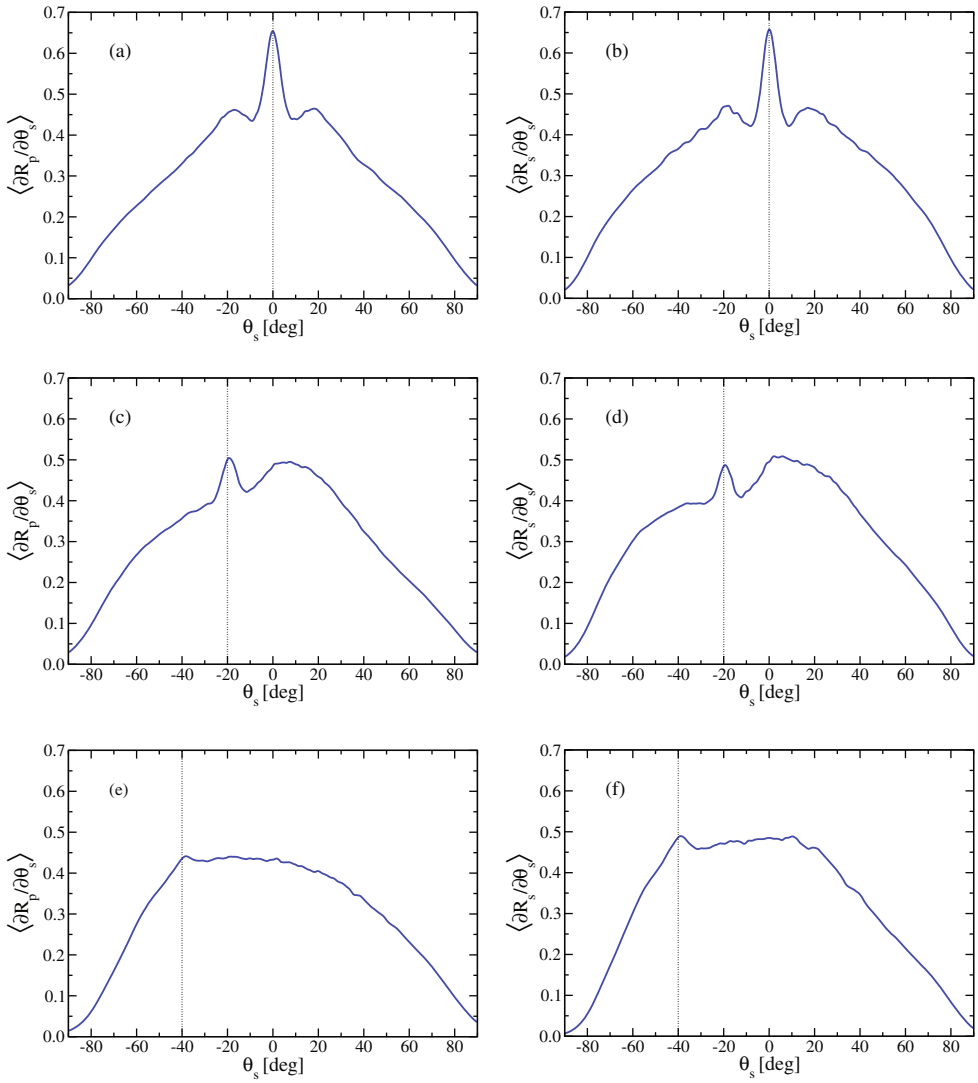

Fig. 19. Rigorous computer simulation results for the angular dependence of the mean differential reflection coefficient for p- (left column) and s-polarized (right column) incident light that was scattered from a strongly rough silver surface. The wavelength of the incident light was $\lambda = 0.6127\,\mu m$ for which the dielectric constant of silver is $\varepsilon(\omega) = -17.2 + i0.498$. The angles of incidence of the light were $\theta_0 = 0^\circ$ (Figs. 19(a) and (b)); $\theta_0 = 20^\circ$ (Figs. 19(c) and (d)); and $\theta_0 = 40^\circ$ (Figs. 19(e) and (f)). The vertical dashed lines indicate the location of the backscattering direction, $\theta_s = -\theta_0$. The strongly rough surface was characterized by a Gaussian height distribution of rms-height $\delta = 1\,\mu$m and the transverse correlation length for the Gaussian correlated surface was $a = 2\,\mu$m. The length of the surface was $L = 25.6\,\mu$m and a finite sized beam of width $g = 6.127\,\mu$m was used in the simulations. The number of discretization points was $N = 500$. The numerical results were all based on an ensemble average over $N_\zeta = 10,000$ realizations of the randomly rough surface.

(when $\theta_0 = 10^\circ$) that the sudden increase in $\langle \partial R_\nu/\partial\theta_s \rangle_{incoh}$ takes place. Similar arguments to those just given apply for other angles of incidence.

Strongly rough surfaces

Strongly rough surfaces will now be considered. In order to conduct theoretical and numerical studies of the enhanced backscattering phenomenon for such surfaces we have to resort to rigorous numerical simulations (Sec. 4.10). In Figs. 19 we present the results of such

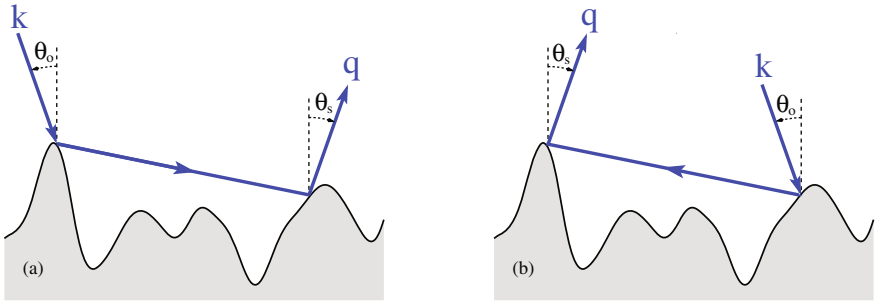

Fig. 20. Diagrams showing two double scattering paths that for strongly rough surfaces contribute to the enhanced backscattering peak phenomenon by interfering constructively whenever $\theta_0 = -\theta_s$.

simulations for the angular dependence of the incoherent component of the mean DRC for p- and s-polarized light of wavelength $\lambda = 0.6127\,\mu m$ incident on a rough vacuum-metal surface of rms-height $\delta = 1\,\mu$m. The correlation length for the Gaussian correlated surface was $a = 2\,\mu$m. The main difference between these results (Figs. 19) and those obtained for the weakly rough surfaces (Figs. 18) is that we now also observe an enhanced backscattering peak in the case of s-polarization. So what is the reason for this difference between weakly and strongly rough surfaces when it comes to the backscattering phenomenon? The explanation lies in the mechanism causing the backscattering peak for strongly rough surfaces [66,168–170]. Since the excitation of surface plasmon polaritons is weak for strongly rough surface, it is unlikely that the reason for the backscattering peak is caused by this type of surface waves. Such a mechanism could not in any case explain the presence of the backscattering peak observed for s-polarization. Instead the backscattering peak for strongly rough surfaces arises due to the constructive interference between multiple scattered volume paths like those shown, for instance, in Figs. 20. In this case, no surface waves are excited, but instead the multiple scattering takes place within the valleys of the strongly rough surface. Similar to the weakly rough case, the two paths of Figs. 20 will interfere constructively in the backscattering direction. Since this mechanism does not involve any surface plasmon polaritons, there is no reason why the backscattering phenomenon should not show up also in s-polarization from strongly rough surfaces. In fact as can be seen from Fig. 19(c) and (d), the backscattering peak in s-polarization is as pronounced as for p-polarization. Observe also that the energy scattered incoherently, which for strongly rough surfaces is close to the total scattered energy, is of roughly the same order for both polarizations. This is in contrast to the situation found for weakly rough surfaces (Fig. 18).

The enhanced backscattering phenomenon from strongly rough surfaces was experimental confirmed (Fig. 21) as early as 1987 by Méndez and O'Donnell [168]. This was just two years after backscattering enhancement was prediction theoretically for weakly rough surfaces by McGurn et al. [124]. These results were the first experimental evidence of enhanced backscattering for any surface discorded system.

In passing, we would like to add that for scattering geometries supporting also transmission, a similar effect to the enhanced backscattering may also exist in transmission [38,171,172,180]. This phenomenon – known as *enhanced transmission* – is also a multiple scattering effect, and its physical origin is analogous to that of enhanced backscattering. Moreover, enhanced transmission has also been observed experimentally [172].

5.2.2 Satellite peaks

The backscattering phenomenon discussed in the previous subsection is not the only multiple scattering effect that might exist when light is scattered from a randomly rough surface. Another such effect is the existence of so-called *satellite peaks* predicted in 1994 by Freilikher, Pustilnik, and Yurkevich [175]. Satellite peaks are enhancements in the angular distribution of light scattered incoherently from scattering systems that supports more the one surface

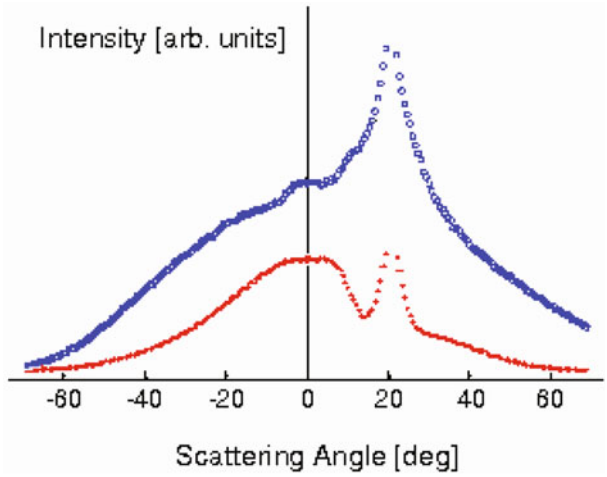

Fig. 21. The experimental measurements of Méndez and O'Donnell [168] showing the first observation of the enhanced backscattering phenomenon in the domain of rough surface scattering. The strongly rough aluminum surface obeyed Gaussian statistics and was characterized by a correlation length $a = 1.8\,\mu$m and an rms-height in the range $\delta = 1$–$2\,\mu$m (the precise value not known). The incident light was s-polarized, its wavelength was $\lambda = 632.8\,$nm, and the polar angle of incidence was $\theta_0 = -20^\circ$. The data shown are for in-plane (blue $\circ$) co-polarized ($s \to s$) scattering; and (red $+$) cross-polarized ($s \to p$) scattering. (Adapted after Ref. [168].)

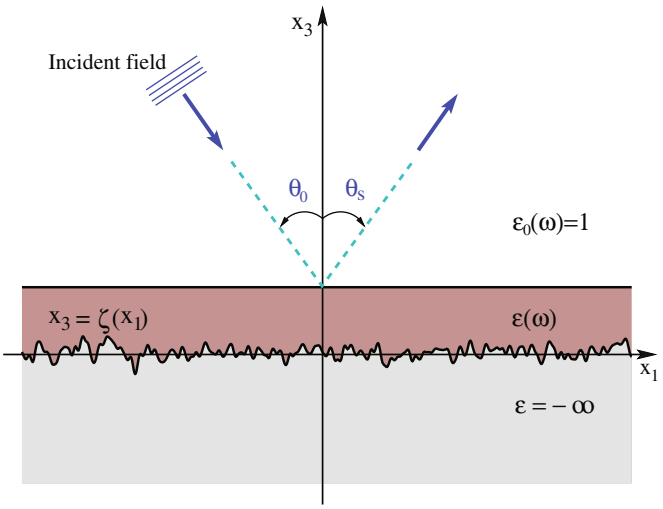

Fig. 22. A sketch of a film scattering geometry that supports guided waves and that may give rise to satellite peaks in the angular dependence of the scattered light.

[175–177,179] or guided wave [97,98,178,180–182]. As will be shown in detail in Sec. 5.2.3, they are not caused by interference between reciprocal paths as was the case for the backscattering phenomenon, but instead by interference of *nonreciprocal* paths. These enhancements should occur for scattering angles that are located symmetrically with respect to the position of the enhanced backscattering peaks that the scattering system also gives rise to. In Section 5.2.3 a detailed mathematical derivation of the angular positions of the satellite peaks will be given.

To illustrate this phenomenon, let us study the specific film scattering geometry shown in Fig. 22. For the satellite peaks phenomenon to exist for a film geometry, one or both of the interfaces will have to be rough, and it is not important which one [38,39,97,98,180,182].

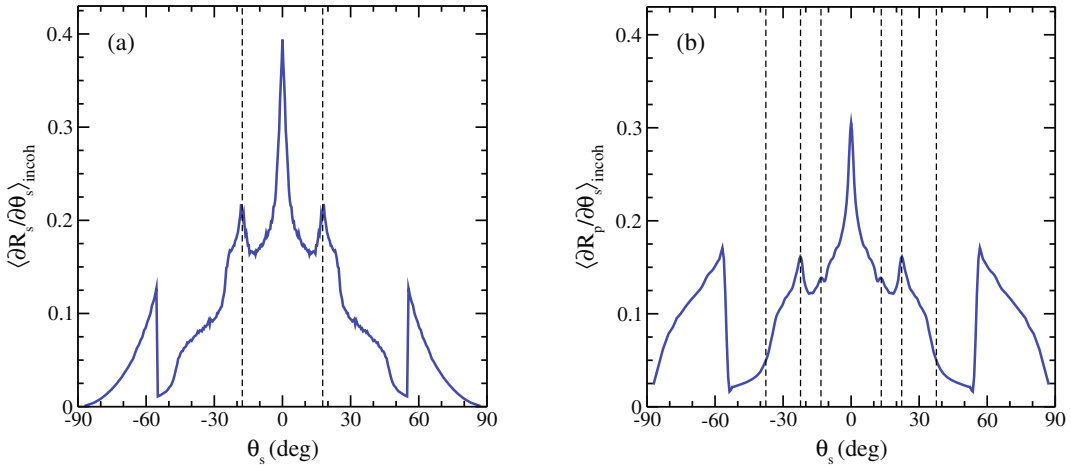

Fig. 23. The contribution to the mean differential reflection coefficient from the incoherent component of the scattered light $\langle \partial R_\nu/\partial\theta \rangle_{\rm incoh}$ as a function of the scattering angle θ_s when an s- (Fig. 23(a)) or p-polarized (Fig. 23(b)) plane wave of wavelength $\lambda = 632.8\,$nm was incident normally ($\theta_0 = 0^\circ$) on the film scattering geometry shown in Fig. 22. The dielectric constant of the film at the wavelength of the incident light was $\varepsilon(\omega) = 2.6896 + i0.01$, and the mean thickness of the film was $d = 500\,$nm. The semi-infinite medium which the film was ruled on was a perfect conductor. The surface profile function $\zeta(x_1)$ of the film-conductor interface was characterized by a Gaussian surface height distribution of rms-height $\delta = 30\,$nm and a West-O'Donnell power spectrum defined by the parameters $k_- = 0.82(\omega/c)$ and $k_+ = 1.97(\omega/c)$. The length of the surface used in the simulations was $L = 160\lambda$ and the results were obtained after averaging over $N_\zeta = 3,000$ realizations of the surface profile function. The dashed vertical lines indicate the estimated positions of the satellite peaks (see Ref. [98] for details). The results were obtained by numerical simulations based on the reduced Rayleigh equation. The data in Fig. 23(b) have been smoothed (with an 11-point Gaussian filter) to make the positions of the satellite peaks more apparent. (After Ref. [98].)

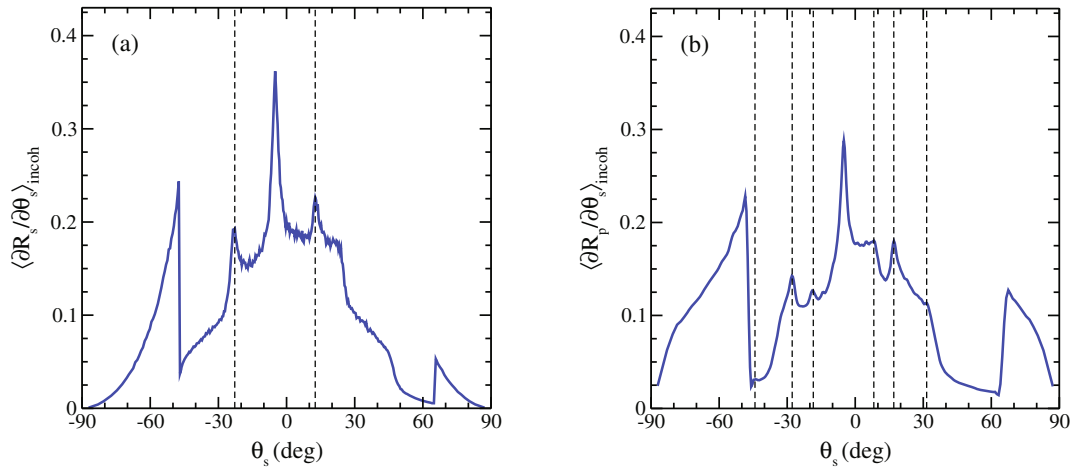

Fig. 24. The same as Figs. 23, but now for an angle of incidence of $\theta_0 = 5^\circ$. (After Ref. [98].)

For the geometry of Fig. 22 the lower interface is rough and the upper is planar. The lower semi-infinite medium is assumed to be a perfect conductor, the film consists of a dielectric medium characterized by a dielectric constant $\varepsilon(\omega)$, while the incident medium is assumed to be vacuum. In Figs. 23 and 24 we show the results of numerical simulations for the mean differential reflection coefficient in the case of s- or p-polarized light incident on the surface at

an angle of incidence $\theta_0 = 0°$ (Figs. 23) and $\theta_0 = 5°$ (Figs. 24), respectively. The remaining surface parameters are given in the caption of Figs. 23.

In the case of s-polarization, and normal incidence, the scattering system of mean film thickness $d = 500\,\text{nm}$ supports two satellite peaks, while in the case of p-polarization it can at most support six such peaks [98]. The positions of these peaks are indicated by dashed vertical lines in Figs. 23. From Fig. 23(a) the two satellite peaks that the scattering system supports are easily distinguished from the background. However, from Fig. 23(b) one sees that only four out of the six possible peaks can be observed. There are two reasons why some of these satellite peaks may not be observable: First, some of them may lie in the non-radiative part of the spectrum, and are therefore not even in principle observable. Second, their strength might be too low to be observable [97,98], *i.e.* one (or both) of the channels involved in the interference process that gives rise to the satellite peaks might have too low intensity [97,98] (see Sec. 5.2.3).

It can be shown (result not shown) that by reducing the thickness of the film, and thus reducing the number of guided waves that the system supports, say to one, all the satellite peaks vanish while the enhanced backscattering peak is still present [182]. In an analogous way, if the film thickness is increased, more than two satellite peaks might be seen [182].

When the light is incident on the film geometry at an angle $\theta_0 \neq 0°$, one observes from Figs. 24 that the satellite peaks move, but are located symmetrically around the backsscattering (anti-specular) direction.

The satellite peak phenomenon has not been observed experimentally for the kind of scattering geometry that we considered here. However, this effect was experimentally observed in a related geometry allowing light scattering by double passage through a strongly diffusing system [183]. In this experimental study both enhanced backscattering and satellite peaks were observed, but also dips.

5.2.3 A formal approach to enhanced backscattering and satellite peaks

In the previous two subsections (Secs. 5.2.1 and 5.2.2) the enhanced backscattering and satellite peak phenomena were discussed. In the present subsection a more detailed analysis and formal approach towards these two phenomena will be presented. In particular we will determine at which angular positions the peaks can be expected.

Let us consider a general film scattering system, where at least one of the interfaces are rough and where one example of such a system is provided in Fig. 22. Depending on the (average) thickness of the film, the scattering system supports $N > 0$ guided waves at the frequency, ω, of the incident light. The wavenumbers of these modes, or "channels" as some authors prefer to call them, will be denoted by $q_n(\omega)$ where $n = 1, \ldots N$. Through the surface roughness the incident light may couple to these guided waves.

In Fig. 25 we show two general double scattering paths[24] where the scattering takes place at the same scattering centers, but in the reverse order. Such paths will in general be phase incoherent due to the randomness of the rough surface. However, we will now look into if there are particular angles of incidence and scattering for which these two paths are phase coherent, *i.e.* have zero phase difference. To this end, let us start by assuming that path $ABCD$ goes through channel m and path $\bar{A}CB\bar{D}$ through the n-channel. The phase difference between these two paths can then be expressed as [38]

$$\Delta\phi_{nm} = \mathbf{r}_{BC} \cdot (\mathbf{k}_0 + \mathbf{k}_s) + |\mathbf{r}_{BC}| \left[q_n(\omega) - q_m(\omega)\right]. \tag{143}$$

Here $\mathbf{k}_0$ and $\mathbf{k}_s$ are the wave vectors of the incident and scattered waves, respectively, while $\mathbf{r}_{BC}$ is the (vector) distance from point B to C. According to its definition, we will have phase coherence when this phase-difference is zero, *i.e.* when $\Delta\phi_{nm} = 0$. Now let us consider separately two cases: (*i*) $n = m$ and (*ii*) $n \neq m$. In the first case, the last term in Eq. (143) is zero with

[24] We here consider double scattering for simplicity. Higher order scattering processes can be treated the same way, but doing so will not change the main conclusions.

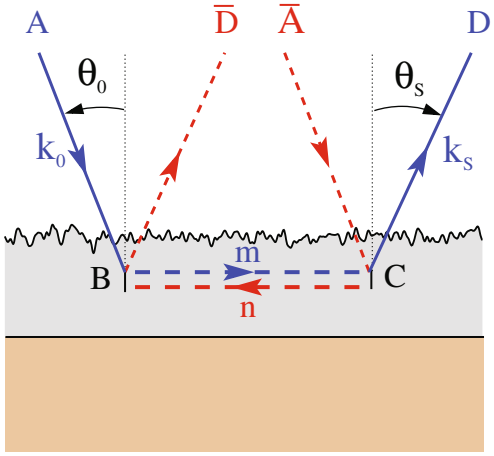

Fig. 25. Illustration of two double scattering sequences occurring in the scattering of electromagnetic waves from a bounded system that supports more the one guided (or surface) wave.

the consequence that one has phase coherence if $\mathbf{k}_s = -\mathbf{k}_0$. This condition is obviously what gives rise to the enhanced backscattering phenomenon. In the second case, when $m \neq n$, the last part of Eq. (143) does not vanish. The condition for phase coherence then becomes [38,180]

$$\sin\theta_s = -\sin\theta_0 \pm \frac{1}{\sqrt{\varepsilon_0(\omega)}}\frac{c}{\omega}\left|q_n(\omega) - q_m(\omega)\right|. \tag{144}$$

In this equation we have also allowed for the case $m = n$ since it naturally includes the position of the backscattering peak. Hence, Eq. (144) defines the angles for which peaks due to both the enhanced backscattering and satellite peak phenomena are expected in the angular dependence of the light scattered incoherently from the randomly rough surface. The angle obtained for $m = n$ is the position of the backscattering peak, while the angles obtained for $m \neq n$ correspond to satellite peaks. The reader should check that the angles obtained from Eq. (144) fit the position of the satellite peaks shown in Fig. 23. The values for $q_n(\omega)$ can be found in Refs. [97,98].

5.3 Enhanced forward scattering (enhanced specular peaks)

The enhanced backscattering and satellite peak phenomena that may exist when light is scattered from randomly rough surfaces were predicted in the 1980s and 1990s, respectively [124,175]. A more recently discovered multiple scattering effect that can exist in rough surface scattering is the so-called *enhanced forward scattering* (or enhanced specular peak) phenomenon that we will introduce and discuss in this section.

The phenomenon was first predicted in 2001 by K.A. O'Donnell based on a high-order (eight order) perturbation theory [173]. This author demonstrated that the intensity of p-polarized light that is scattered *incoherently* (diffusely) from a weakly rough random metal surface can, under certain conditions, in addition to the backscattering enhancement also show a peak (local enhancement relative to that of the background) in the specular direction $\theta_s = \theta_0$ (Figs. 28 and 29).

For the above reason, O'Donnell coined the term "enhanced specular peaks" for the phenomenon. It should be stressed, however, that these peaks are not due to coherent (specular) scattering effects, but instead are features present in the incoherent component of the scattered light. To avoid potential confusion, and to draw on the analogy with the backscattering enhancement, we will in the following refer to the effect by the alternative name – the "*enhanced forward scattering*" phenomenon. So far, the forward scattering enhancement phenomenon has not been observed experimentally.

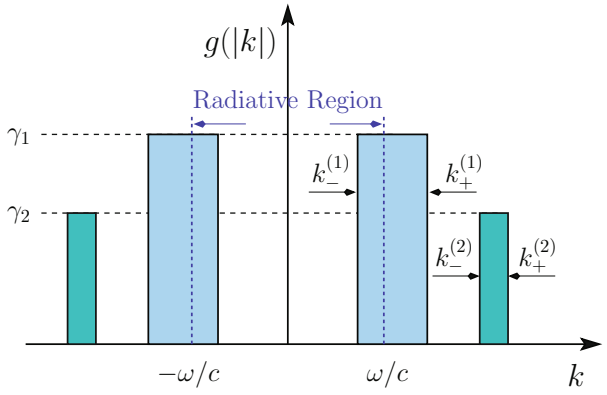

Fig. 26. A sketch of the double-rectangular power spectrum, Eqs. (145), with cutoff wavenumbers, $k_\pm^{(i)}$, and amplitudes γ_i $(i = 1, 2)$ that is used to study the enhanced forward scattering enhancement.

Numerical results showing the forward scattering enhancement phenomenon that are obtained from perturbation theory can be found in Refs. [108,173,174]. Here, however, we prefer to present numerical (Monte Carlo) simulation results that show this effect and are obtained on the basis of the reduced Rayleigh equation (Sec. 4.5) (see also Ref. [174]). Such computer simulations have the advantage of being able to handle scattering system of a level of roughness which is well beyond what can be practically handled by perturbation theory.

Again we consider the (standard) scattering geometry consisting of a randomly rough surface separating vacuum and a metal (Fig. 8). The rough interface is illuminated from the vacuum side by a p-polarized incident wave. However, the power spectrum for the surface roughness used in this case is of a "double-rectangular" form and defined as (Fig. 26)

$$g(|k|) = \gamma_1\, g_1(|k|) + \gamma_2\, g_2(|k|), \tag{145a}$$

with

$$g_i(|k|) = \frac{\pi}{k_+^{(i)} - k_-^{(i)}} \left[\theta(k_+^{(i)} - k)\theta(k - k_-^{(i)}) + \theta(k_+^{(i)} + k)\theta(-k - k_-^{(i)})\right], \tag{145b}$$

where $\gamma_i \geq 0$ $(i = 1, 2)$ are constants so that $\gamma_1 + \gamma_2 = 1$ and $\theta(\cdot)$ denotes the Heaviside step function. Moreover, the wavenumbers $k_\pm^{(i)}$ define the upper $(k_+^{(i)})$ and lower $(k_-^{(i)})$ cutoffs of the rectangular domain i. From Sec. 4.6, Eq. (92b), we recall that the (single) scattering process from wavenumber k into q has a "coupling strength" that is proportional to $g(|q - k|)$. The main purpose of the parts of the power spectrum defined by $k_\pm^{(2)}$ is to allow for the counter-propagation of modes of wavenumber q that satisfies $2|q| \in [k_-^{(2)}, k_+^{(2)}]$. Such counter-propagating surface modes go to the heart of the forward scattering enhancement phenomenon.

For later comparison, we start by briefly presenting results for cases where the power spectrum, $g(|k|)$, consists of only one of the two possible components, *i.e.* when γ_2/γ_1 is 0 or ∞. In the main panels of Figs. 27, we present computer simulation results for the incoherent component of the mean differential reflection coefficient for p-polarized plane waves incident on a silver surface at an angle of incidence θ_0 and where the total power spectrum of the surface roughness was equal to either $g_1(|k|)$ (Fig. 27a) or $g_2(|k|)$ (Fig. 27b). Striking differences are observed between the scattering patterns in the two cases. These differences can be understood on the basis of the discussion made in Sec. 5.2.1, and by noting that SPPs only can be excited by the surface roughness when $\gamma_1 \neq 0$ (for the values of $k_\pm^{(i)}$ assumed here), and when the incident light is p-polarized.

We now address the more interesting situation where neither γ_1 nor γ_2 is zero, *i.e.* the power spectrum, $g(|k|)$, receives contributions from both $g_1(|k|)$ and $g_2(|k|)$ (*c.f.* Eqs. (145)). We note that in this case SPPs of (lateral) wavenumber $k_{spp}(\omega)$, can in principle be excited

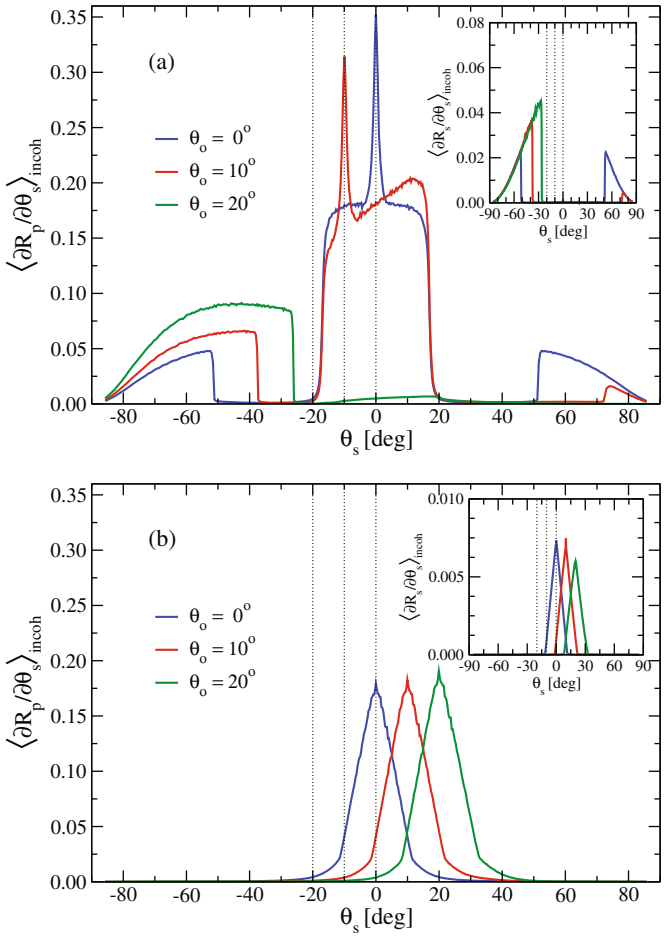

Fig. 27. The incoherent component of the mean differential reflection coefficient, $\langle \partial R_\nu / \partial \theta_s \rangle_{incoh}$, for an either p- (main panel) or s-polarized plane wave (inset) incident from vacuum on a rough silver surface at wavelength $\lambda = 0.4579\,\mu$m ($\varepsilon(\omega) = -7.5 + 0.24i$) and an angle of incidence θ_0 as given by the legends. The rough surface (of length $L = 200\lambda$) had a Gaussian height distribution of rms-height 10 nm, and the power spectrum was characterized by Eqs. (145) with $k_-^{(1)} = 0.782\omega/c$, $k_+^{(1)} = 1.366\,\omega/c$, $k_-^{(2)} = 2.048\,\omega/c$, and $k_+^{(2)} = 2.248\,\omega/c$, with either (a) $\gamma_1 = 1$ and $\gamma_2 = 0$ or (b) $\gamma_1 = 0$ and $\gamma_2 = 1$. The vertical dotted lines indicate the backscattering directions. The results were averaged over 10,000 realizations of the surface roughness. For p-polarized light, incident at an angle $|\theta_0| < \theta_{\max} = 17°$, the enhanced backscattering peaks are readily observed in the diffusely scattered light. (After Ref. [89].)

by the surface roughness and may counter-propagate along it (since $g(2|k_{spp}(\omega)|) \neq 0$) and by doing so give rise to the multiple scattering effect that we focus on in this section. Computer simulation results for the situation where $\gamma_1 \neq 0$ and $\gamma_2 \neq 0$ are presented in Figs. 28 for a set of values of the ratio γ_2/γ_1 distributed over the range $[0, \infty)$. For all cases, the light incident on the surface was p-polarized, and the angle of incidence was $\theta_0 = 10°$. We recall that changing γ_2/γ_1 does not influence the rms roughness of the surface and it was therefore constant (and equal to $\delta = 10$ nm) for all cases.

From Fig. 28(a), and in particular its inset, it is apparent that increasing γ_2/γ_1 (from zero) will gradually lead to the appearance of peaks at the specular direction, $\theta_s = \theta_0$, in addition to the backscattering peaks already existing at $\theta_s = -\theta_0$. It is the presence of these *enhanced forward scattering peaks* located at the specular position that constitutes the forward scattering enhancement phenomenon. However, when γ_2 is becoming significantly larger than γ_1, the backscattering peak disappears, and a "Λ-shaped" intensity distribution of the scattered light

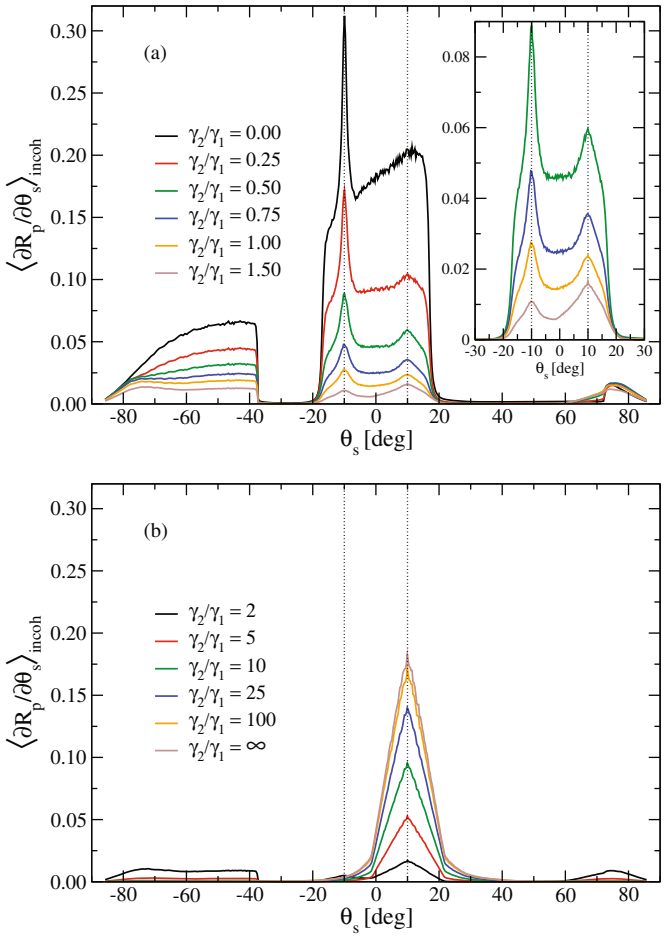

Fig. 28. The same as Fig. 27, but now for a fixed angle of incidence $\theta_0 = 10^\circ$ and for different values of the power spectrum amplitude ratio γ_2/γ_1. When this ratio is different from zero, and $\gamma_2/\gamma_1 \sim 1$ enhanced forward scattering peaks start to be observed in addition to the backscattering peaks. The dotted vertical lines indicate the position of the forward scattering (specular) and backscattering directions. (After Ref. [89].)

is instead emerging (Fig. 28(b)). The intensities of the maxima of these latter distributions, located at the specular positions, are increasing with γ_2/γ_1 while their baseline widths seem to be less affected by the same ratio. In this latter case, as the angle of incidence is changed (for the surface parameters used) to above $\theta_{max} = 17^\circ$ where θ_{max} is defined in Eq. (142) (results not shown), no dramatic effect on the scattering pattern is observed (except for an angular translation), indicating that SPPs are not contributing significantly to the scattering. However, for moderate values of the ratio γ_2/γ_1, and for which also backscattering peaks are observed (Fig. 28(a)), a marked change in the scattering patterns is observed as the angle of incidence is increased from below to above θ_{max} (Fig. 29). Recalling that the coupling constants of the incident light into SPPs essentially is γ_1, the above observations is to be expected.

The physical origin underlying the enhanced forward scattering phenomenon was presented in the original publication predicting its existence [173]. Here O'Donnell showed that the existence of these peaks at the specular position in the intensity of the diffusely scattered light required a power spectrum, $g(|k|)$, that supports the *counter-propagation* of SPPs (or other resonant surface modes)[25]. By counter-propagating SPPs, we mean scattering processes

[25] As long as the power spectrum supports counter-propagation, forward scattering peaks should in principle be possible. However, only when resonant modes can be excited, like SPPs, will the phenomenon be pronounced (Fig. 29).

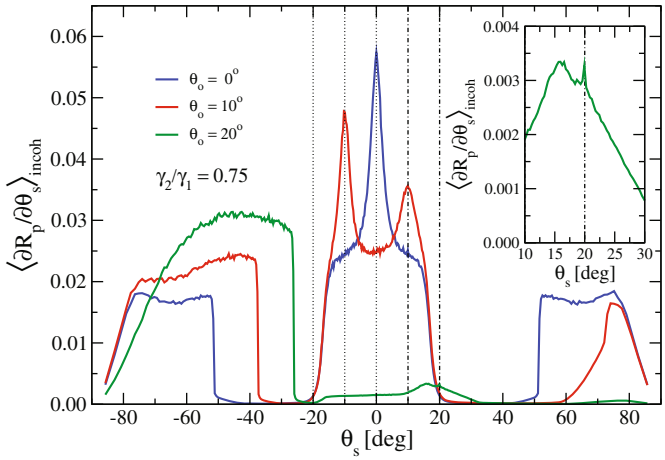

Fig. 29. Same as Fig. 27(a), but for $\gamma_2/\gamma_1 = 0.75$. The vertical dash-dotted lines indicate the forward scattering (specular) directions. The inset shows a closeup of the curve corresponding to $\theta_0 = 20°$. It shows that forward scattering peaks are in principle also possible if SPPs can not be excited by the incident light, but in this case the phenomenon is much less pronounced. (After Ref. [89].)

where an SPP of (lateral) wavenumber $k_{spp}(\omega)$ propagating in one direction being scattered by the surface roughness into another SPP that is propagating in the opposite direction; $\pm k_{spp}(\omega) \to \mp k_{spp}(\omega)$. Such processes are only possible if $g(2k_{spp}) \neq 0$ at the frequency, ω, of the incident light. However, $g(2k_{spp}) \neq 0$ does not guarantee that forward scattering peaks can be observed, since also the coupling of the incident light into SPPs must be strong for this to happen (see Fig. 28(b)).

Furthermore, O'Donnell demonstrated that the lowest order terms in the perturbation theory contributing to the enhanced forward scattering phenomenon consist of a set of fourth order scattering processes that can interfere constructively only in the specular direction, $\theta_s = \theta_0$ [108,173,174]. Such set of paths is depicted in Figs. 30, and we will now outline the details of the physical origin for this phenomenon and to show that these paths may interfere constructively in the specular direction.

One of the contributing scattering sequences is, $k \to -k_{spp} \to k_{spp} \to -k_{spp} \to k$ that includes, as stated above, the counter-propagation of SPPs [108,173,174]. By following a similar approach to that of Sec. 5.2.3, one finds that the phase delay along the path depicted in Fig. 30(a), hereafter referred to as path A, can within the usual far-field approximation be written as [173]

$$\phi_A = k\xi_1 - q\xi_4 + \phi_{1-4}, \tag{146}$$

where ξ_n denotes the x_1-coordinate of surface point n, and ϕ_{1-4} represents the total phase delay along the path (in the metal) $1 \to 2 \to 3 \to 4$. The path of Fig. 30(b) (path B) is obtained from that of path A by keeping ξ_2 and ξ_3 unchanged while adjusting the positions of the start and end points so that they become $\xi_{1'}$ and $\xi_{4'}$, respectively. Hence, the phase delay associated with path B becomes

$$\phi_B = k\xi_{1'} - q\xi_{4'} + \phi_{1'-4'}. \tag{147}$$

If the spatial separations between the start and end points of path A and B are the same, *i.e.* $\xi_4 - \xi_1 = \xi_{4'} - \xi_{1'}$ so that $\phi_{1-4} = \phi_{1'-4'}$, then the phase difference between the two paths depicted in Fig. 30(a)–(b) is

$$\Delta\phi_{BA} \;=\; \phi_B - \phi_A = q\,(\xi_4 - \xi_{4'}) - k\,(\xi_1 - \xi_{1'}) \;=\; (q-k)\,(\xi_1 - \xi_{1'})\,. \tag{148}$$

In order for these two paths to interfere constructively, the phase difference between them has to be zero, $\Delta\phi_{BA} = 0$. From Eq. (148) it follows that this happens whenever $q = k$, or in other words, whenever the angle of scattering is equal to the angle of incidence, $\theta_s = \theta_0$ (the specular

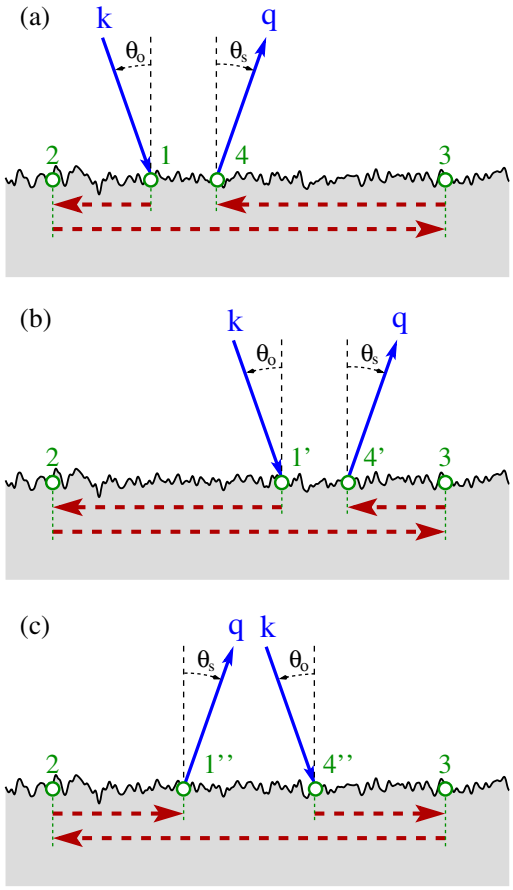

Fig. 30. The (leading order) scattering processes contributing to the enhanced forward scattering (enhanced specular peak) phenomenon. The red dashed horizontal arrows indicate SPPs propagating along the rough surface. (Adapted after Ref. [173].)

direction). We note that for a given path A, there is in principle an infinite number of paths of type B that interfere constructively with path A (provided $\xi_4 - \xi_1 = \xi_{4'} - \xi_{1'}$).

Also another family of paths exists, path C, where the points are visited in opposite order to those of paths A and B; $4'' \to 3 \to 2 \to 1''$ (see Fig. 30(c)) [26]. By symmetry, it is realized that path B and C interfere constructively whenever $\xi_{1'} = \xi_{1''}$ and $\xi_{4'} = \xi_{4''}$. Furthermore, paths A and C, can also interfere constructively, as can be seen by calculating their phase difference which readily can be shown to be (*c.f.* Eq. (143))

$$\phi_{CB} = (q - k)(\xi_1 - \xi_{1''}) + (q + k)\Delta\xi, \tag{149}$$

where $\Delta\xi = \xi_4 - \xi_1 = \xi_{4''} - \xi_{1''}$. Hence, Eq. (149) predicts that paths A and C, interfere constructively in the specular direction whenever $\Delta\xi = 0$, *i.e.* when the start and end points of the two paths close onto themselves ($\xi_1 = \xi_4$ and $\xi_{1''} = \xi_{4''}$).

Hence in summary, it has been demonstrated that the forward scattering enhancement phenomenon arises (to lowest order in perturbation theory) due to the constructive interference of the fourth order scattering processes of Figs. 30 (with the additional condition on them as stated above) [108,173,174]. This higher (than two order) multiple scattering effect has so far not been observed in experiments and it is a challenge for experimentalists.

[26] Depending on the power spectrum of the surface roughness, such path may, or may not, be allowed.

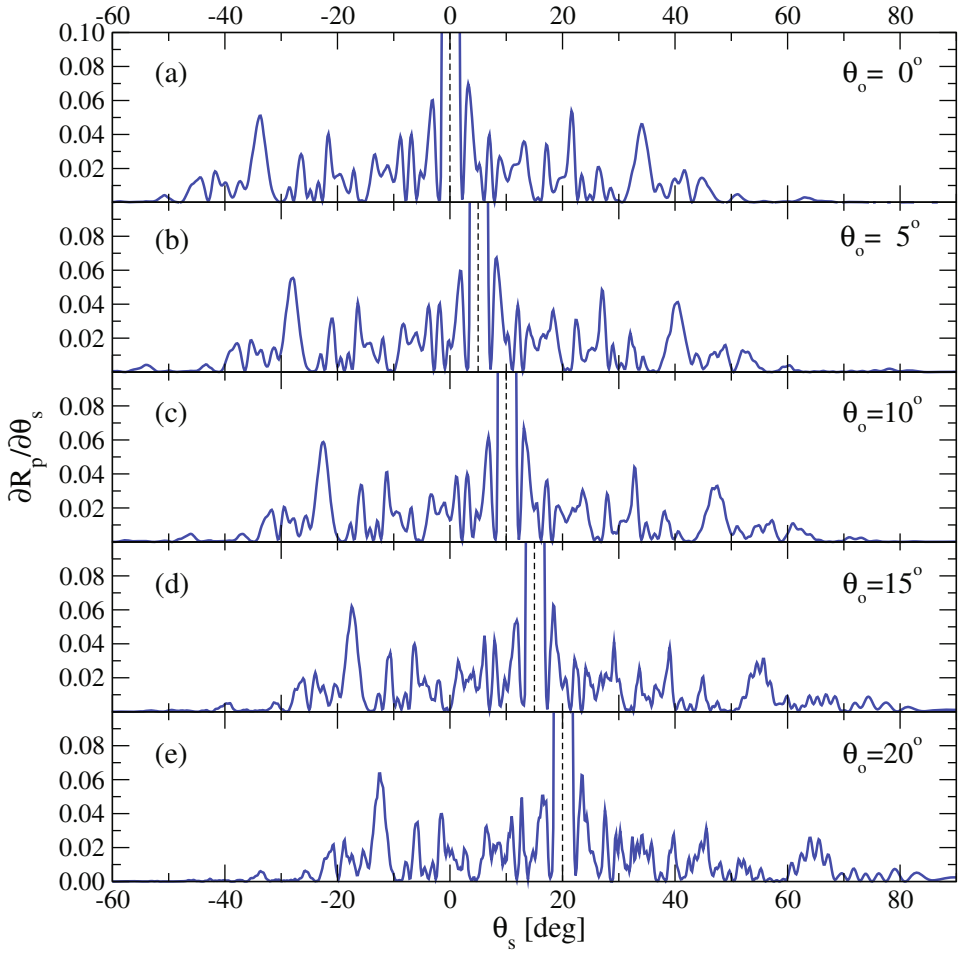

Fig. 31. Speckle patterns that result from the scattering of light of wavelength $\lambda = 0.6127\,\mu$m incident on the same rough silver surface at a selection of angles of incidence, θ_0, as given by the legends. The Gaussian height-distributed surface was characterized by an rms-height $\delta = 8\,$nm and a (Gaussian) correlation length $a = 0.4\,\mu$m. The length of the surface was $L = 100\,\mu$m and the dielectric constant of silver at the wavelength of the incident light is $\varepsilon(\omega) = -17.2 + i0.498$. The dashed vertical lines indicate the specular directions.

5.4 Angular intensity correlations for the scattered light from randomly rough surfaces

It has been known for quite some time that when electromagnetic waves, all of the same frequency, are scattered from a random system, speckle patterns might be observed [13–15,184] (see also Fig. 2). Such patterns are results of interference between waves scattered from different locations in the random medium. From studies of volume disordered systems, such patterns are known to contain a rather rich structure [13–15,184,185]. In particular, it was predicted theoretically [185] for such scattering systems that there should exist three types of intensity correlations – short-range correlations, long-range correlations, and infinitely-range correlations. These correlations were termed the $C^{(1)}$, $C^{(2)}$, and $C^{(3)}$-correlations, respectively, and they have all been observed experimentally [186–188].

We will now discuss speckle correlations, not for light scattered from volume disordered systems, but instead for light scattered from surface disordered system. Examples of such speckle patterns obtained when an electromagnetic wave is scattered from a randomly rough surface are depicted in Fig. 31.

Let us start by considering a planar surface separating two different materials. Since the surface is planar, the scattering is completely understood as expressed through the celebrated

Fresnel's formulae [4,9]. Imagine an experiment where light is incident at an angle θ_0 onto the interface. Since the surface is planar, all the light is scattered into the specular direction $\theta_s = \theta_0$, and its intensity is given by Fresnel formula. If we in a second experiment incident the light at an angle $\theta_0' = -\theta_0$, *i.e.* at an angle that was the specular direction in the first experiment, all the light will be scattered into $\theta_s' = \theta_0' = -\theta_0$ and its intensity is again given by Fresnel's formula. The scattered intensities in these two experiments are in fact equal. This is easily realized from the Fresnel formulae 89b by noting that the α-factors that they contain are unaffected by a change of sign in the lateral wavenumber (momentum variables). Thus, if we know the result of the first experiment, say, we also know the outcome of the second one. In other words, these two intensities are perfectly correlated. We now introduce the lateral wavenumbers q and k related in the usual way to the angles of scattering and incidence, respectively (see *e.g.* Eq. (151) below). Let the notation (q, k) denote a corresponding pair of wavenumbers where q is the scattered (lateral) wavenumber and k the incident wavenumber. For our planar surface geometry we will thus have perfect correlation between the two scattering processes (q, k) and (q', k') if $(q, k) = (-k', -q')$. Furthermore, since any process, of course, is correlated with itself, we in addition will expect perfect correlation when $(q, k) = (q', k')$.

The above example is rather trivial and well-known example of correlations in the scattered intensity from a planar surface. However, what happens to the angular intensity correlations if the surface is not planar, but instead randomly rough? This is an interesting and non-trivial question and we will address it in this section. In the discussion to be presented below we will focus on the angular correlations in the light scattered *incoherently* from a rough surface. Furthermore, we will mainly discuss the case where the surface is weakly rough. In particular, we will try to answer the following question: When, and under what conditions, will the intensity scattered (incoherent) into the far field for different angles of incidence and scattering be related to each other?

5.4.1 Definition of the angular intensity correlation functions

Let us start by introducing the *unnormalized* angular correlation function, $C(q, k|q', k')$, which we will define as[27] [40,41,46,189].

$$C(q, k|q', k') = \langle I(q|k) I(q'|k') \rangle - \langle I(q|k) \rangle \langle I(q'|k') \rangle , \tag{150}$$

where $I(q|k)$ denotes the intensity of the light scattered from the surface, and the angle brackets denote an average taken over an ensemble of realizations of the surface profile function $\zeta(x_1)$. Furthermore, the (lateral) wavenumbers, q and k, are both, in the radiative region ($|q| \leq \sqrt{\varepsilon_0}\omega/c$), understood to be related to the angles of scattering and incidence, θ_s and θ_0, respectively, according to

$$k = \sqrt{\varepsilon_0(\omega)}\, \frac{\omega}{c} \sin\theta_0, \qquad q = \sqrt{\varepsilon_0(\omega)}\, \frac{\omega}{c} \sin\theta_s. \tag{151}$$

The primed wavenumbers, q' and k', are related in a similar way to the primed angles θ_s' and θ_0'. Theses angles, both primed and unprimed, are defined positive according to the convention indicated in Fig. 32. This figure also shows our scattering system consisting of a semi-infinite dielectric medium with a rough interface to vacuum.

Furthermore, the intensity $I(q|k)$ can be defined through the scattering matrix $S(q|k)$ according to the formula

$$I(q|k) = \frac{\sqrt{\varepsilon_0(\omega)}}{L_1} \left(\frac{\omega}{c}\right) |S(q|k)|^2 , \tag{152}$$

where L_1 is the length of the x_1-axis covered by the random surface.

[27] We have here suppressed any explicit reference to the polarization (the ν-index) since no confusion should result from doing so. All quantities in this section should be understood to be referring to one and the same polarization.

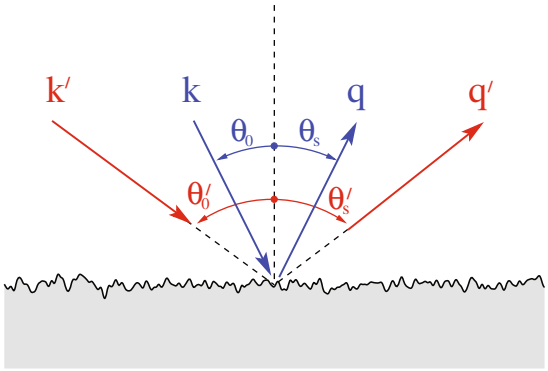

Fig. 32. The scattering system considered in the study of the angular correlation functions.

In many cases it is convenient to work with a normalized correlation function, $\Xi(q,k|q',k')$, in contrast to the unnormalized one. The normalized angular intensity correlation function will we define by[28]

$$\Xi(q,k|q',k') = \frac{\langle I(q|k)I(q'|k')\rangle - \langle I(q|k)\rangle\langle I(q'|k')\rangle}{\langle I(q|k)\rangle\langle I(q'|k')\rangle}. \tag{153}$$

The lesson to be learned from the huge amount of research being conducted on correlation function in the field of random (bulk) disordered systems [185–187,191,192] is that there may exist correlations on many different length scales including *short* to *infinite* range correlations. Thus part of the challenge we are facing will be to separate these different contribution to $C(q,k|q',k')$ (or equivalently to $\Xi(q,k|q',k')$) from one another.

The first step towards such a separation is to rewrite the correlation function in terms of the S-matrix. This is done by substituting the expression for the intensity, Eq. (152), into the definition of the correlation function and thus obtaining

$$C(q,k|q',k') = \frac{\varepsilon_0}{L_1^2}\frac{\omega^2}{c^2}\left[\left\langle |S(q|k)|^2\,|S(q'|k')|^2\right\rangle - \left\langle |S(q|k)|^2\right\rangle\left\langle |S(q'|k')|^2\right\rangle\right]. \tag{154}$$

Due to the stationarity of the surface profile function, the average of the S-matrix should be diagonal in q and k,

$$\langle S(q|k)\rangle = 2\pi\delta(q-k)\,S(k). \tag{155}$$

By now taking advantage of this relation in addition to the cumulant average [193,194]

$$\{AB\} = \langle AB\rangle - \langle A\rangle\,\langle B\rangle\,, \tag{156}$$

the correlation function (154) can be written as

$$\begin{aligned} C(q,k|q',k') = \frac{\varepsilon_0}{L_1^2}\frac{\omega^2}{c^2}\Big[&|\langle\delta S(q|k)\delta S^*(q'|k')\rangle|^2 + |\langle\delta S(q|k)\delta S(q'|k')\rangle|^2 \\ &+ \{\delta S(q|k)\delta S^*(q|k)\delta S(q'|k')\delta S^*(q'|k')\}\Big] + s.t., \end{aligned} \tag{157a}$$

where $\delta S(q|k)$ denotes the incoherent component of the S-matrix defined as

$$\delta S(q|k) = S(q|k) - \langle S(q|k)\rangle\,. \tag{157b}$$

In Eq. (157a) the asterisks denote complex conjugate while *s.t.* means specular terms, *i.e.* terms that are proportional to $\delta(q-k)$ and/or $\delta(q'-k')$. Such terms will not be focused on here since

[28] It should be noticed that a somewhat different definition for the normalized angular intensity correlation function is used by some authors [190]. However, the advantage of the definition 153 is that it does not contain any δ-functions in the denominator.

we will concentrate on the incoherent part of the scattered light. With Eq. (157a) we can now write[29]

$$C(q,k|q',k') = C^{(1)}(q,k|q',k') + C^{(10)}(q,k|q',k') + C^{(N)}(q,k|q',k'), \tag{158a}$$

where

$$C^{(1)}(q,k|q',k') = \frac{\varepsilon_0}{L_1^2}\frac{\omega^2}{c^2}\,|\langle \delta S(q|k)\delta S^*(q'|k')\rangle|^2\,, \tag{158b}$$

$$C^{(10)}(q,k|q',k') = \frac{\varepsilon_0}{L_1^2}\frac{\omega^2}{c^2}\,|\langle \delta S(q|k)\delta S(q'|k')\rangle|^2\,, \tag{158c}$$

and

$$C^{(N)}(q,k|q',k') = \frac{\varepsilon_0}{L_1^2}\frac{\omega^2}{c^2}\,\{\delta S(q|k)\delta S^*(q|k)\delta S(q'|k')\delta S^*(q'|k')\}\,. \tag{158d}$$

Due to reasons which should be clear from the discussion below, the correlation functions in Eqs. (158b) and (158c) are termed *short-range* correlation functions, while the one in Eq. (158d) contains contribution from *long* and *infinite-range* correlations. They will now be discussed in turn.

5.4.2 Short range correlations for weakly randomly rough surfaces

The short range correlation functions, $C^{(1)}$ and $C^{(10)}$, will now be addressed when the roughness is assumed to be weak. These correlation functions are to leading order in the surface profile function a result of single scattering processes [40,41,46,189,190]. However, above leading order they will also receive contributions from multiple scattering. The long and infinite range correlations, $C^{(N)}$, contain at least one multiple scattering process as we will see [189]. Therefore the "optical paths" involved in the processes leading to $C^{(1)}$ and $C^{(10)}$ are typically shorter then those giving rise to $C^{(N)}$. This is one of the reasons why the $C^{(1)}$ and $C^{(10)}$ correlation functions are termed short-range correlation functions. Another reason stems from the fact that $C^{(1)}$ and $C^{(10)}$ are both independent of the length of the random surface. In the next subsection we will demonstrate explicitly that the $C^{(N)}$-correlation function is proportional to $1/L_1$. Hence, in the limit of a long surface the amplitude of the correlation function $C^{(N)}$ is neglectable compared to $C^{(1)}$ and $C^{(10)}$.

The $C^{(1)}$ correlation functions; The memory- and reciprocal memory-effect

From Eqs. (158b) and (158c), it might not immediately be obvious what the features of the short range correlations are. To this end, we will only be concerned about one-dimensional random surfaces, $\zeta(x_1)$, that are stationary and constitutes a Gaussian random process. Under this assumption, the expression $\langle \delta S(q|k)\delta S^*(q'|k')\rangle$, contained in $C^{(1)}$, will be proportional to a Dirac δ-function, *i.e.*

$$\langle \delta S(q|k)\delta S^*(q'|k')\rangle \propto 2\pi\delta(q-k-q'+k'). \tag{159}$$

This is so due to the assumed stationarity of the surface profile function $\zeta(x_1)$. To motivate this, we recall from Sec. 4 (or Ref. [116]), that to lowest order in the surface profile function, the scattering amplitude that is proportional to the S-matrix, is proportional to $\tilde{\zeta}(q-k)$, where $\tilde{\zeta}$ denotes the Fourier transform of the surface profile function. Since $\langle \tilde{\zeta}(q)\tilde{\zeta}^*(k)\rangle = 2\pi\delta(q-k)$, Eq. (159), to lowest order, follows immediately.

Thus, with Eq. (159) we find that the correlation function, $C^{(1)}$, can be written in the convenient form

$$C^{(1)}(q,k|q',k') = \frac{2\pi\delta(q-k-q'+k')}{L_1}\,C_0^{(1)}(q,k|q',q'-q+k). \tag{160}$$

[29] Notice that equivalent expressions can be derived for the normalized correlation functions based on Eq. (153).

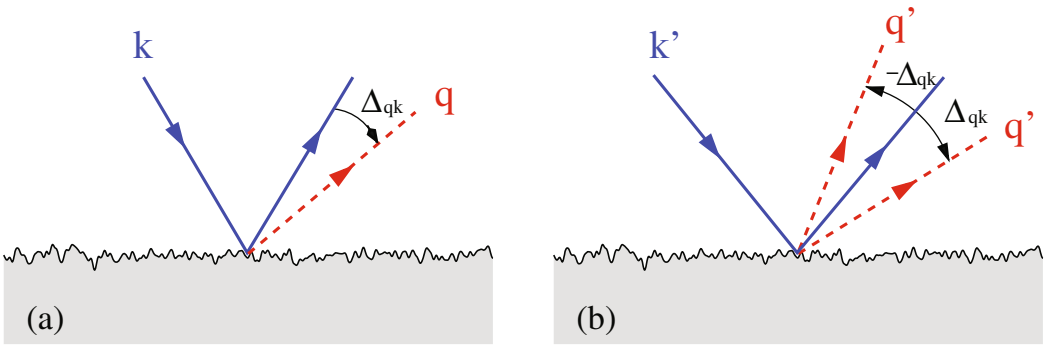

Fig. 33. Interpretation of the correlation condition for the short-range correlation functions (a) $C^{(1)}$ and (b) $C^{(10)}$. The outgoing solid lines indicate the specular direction. The scattering process (q, k) that gives rise to the lateral wavenumber (momentum) transfer $\Delta_{qk} = q - k$ might be correlated with the process (q', k') if $\Delta_{qk} = \Delta_{q'k'}$ $(C^{(1)})$ or if $\Delta_{qk} = -\Delta_{q'k'}$ $(C^{(10)})$.

Here $C_0^{(1)}$ is known as the *envelope function* of $C^{(1)}$ and it is *independent* of the length L_1 of the surface. Notice that the $C^{(1)}$-correlation function can only be non-vanishing when the argument of the δ-function vanishes. Therefore, since $2\pi\delta(0) = L_1$, the (full) $C^{(1)}$-correlation function is also independent of the length of the surface.

To see what the δ-function condition of Eq. (160) means physically, it is convenient to introduce the wavenumber (momentum) transfer that can be associated with the scattering process. If the incident light has wavenumber k and the scattered light is described by the lateral wavenumber q the wavenumber transfer is

$$\Delta_{qk} = q - k. \tag{161}$$

Such a scattering event we recall was earlier denoted by (q, k). Thus, what Eq. (160) says is that the two scattering processes (q, k) and (q', k') might have non-vanishing $C^{(1)}$ correlations if, and only if, the two scattering events have the same wavenumber transfer, *i.e.* if, and only if,

$$\Delta_{qk} = \Delta_{q'k'}. \tag{162}$$

This condition is depicted in Fig. 33(a). From the condition (162) it follows that if the incident wavenumber is changed from say k to $k' = k + \Delta k$, the entire speckle pattern shifts in such a way that any feature initially at q moves to $q' = q + \Delta q$. In terms of the angles of incidence and scattering, we have that if θ_0 is changed to $\theta_0' = \theta_0 + \Delta\theta_0$, any feature in the speckle pattern originally at θ_s is shifted to $\theta_s' = \theta_s + \Delta\theta_s$, where $\Delta\theta_s = \Delta\theta_0(\cos\theta_0/\cos\theta_s)$ to first order in $\Delta\theta_0$. This effect can indeed be seen from the speckle patters presented in Figs. 31.

It should in particular be noticed that condition (162) is satisfied if (*i*) $k = k'$ and $q = q'$ as well as if (*ii*) $k = -q'$ and $q = -k'$. These choices are the ones mentioned in the beginning of this section for the scattering from a planar surface. It is interesting to notice that what for a planar surface were trivial correlations, also holds true for the scattering from randomly rough surfaces, even though as should be noticed, their physical origin is rather different. Situation (*i*) is kind of trivial since any scattering process should be perfectly correlated with itself. This effect is known in the literature as the *memory-effect* [46]. Situation (*ii*), that is less obvious, is a consequence of the reciprocity of the S-matrix; $S(q|k) = S(-k|-q)$ (Eq. (67)). Hence, when $k = -q'$ and $q = -k'$ there should be perfect correlations, and the effect is known as the *reciprocal memory-effect* [46]. If the scattering system does not possess any damping, the system also respects time-reversal symmetry. Due to this reason, the latter effect is also known by some authors as the *time-reversed memory effect*.

In Fig. 34 (solid line) we present the result of perturbative calculations [189] for the envelope of the $C^{(1)}$ correlation function as a function of the scattering angle θ_s' for $\theta_s = -10^\circ$ and $\theta_0 = 20^\circ$. The angle θ_0' is determined from the δ-function condition of Eq. (160). The wave

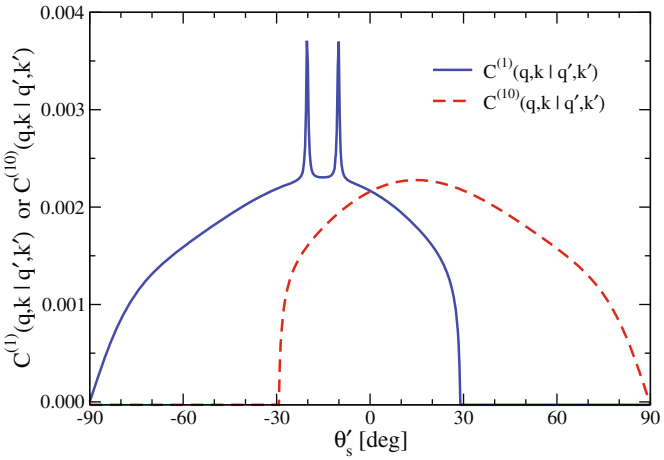

Fig. 34. The envelopes of the short-range correlation functions $C^{(1)}(q,k|q',k')$ (solid line) and $C^{(10)}(q,k|q',k')$ (dashed line) as a function of the scattering angle θ_s' for $\theta_s = -10°$ and $\theta_0 = 20°$. The angle θ_0' is determined from the δ-function constraint. The rough surface was a silver surface characterized by Gaussian height statistics of rms-height $\delta = 5\,\text{nm}$. The correlation function was also Gaussian with a correlation length of $a = 100\,\text{nm}$. The wavelength of the incident light was $\lambda = 457.9\,\text{nm}$. At this wavelength the dielectric constant of silver is $\varepsilon(\omega) = -7.5 + i0.24$. (Adapted after Ref. [189].)

incident on the rough vacuum-metal geometry was p-polarized, and the surface parameters are defined in the caption of this figure. Two well-pronounced peaks at scattering angles $\theta_s = -20°$ and $\theta_s = -10°$ are easily spotted in the envelope of $C^{(1)}$. They correspond respectively to the memory and reciprocal memory effect. It can in fact be shown that by instead considering the envelope of the normalized correlation function, $\Xi^{(1)}$, one will have perfect correlation at the position of these two peaks (see *e.g.* Ref. [195]).

Before proceeding, we would like to point out that the memory and reciprocal memory effect seen in Fig. 34 are due to multiple scattering processes that involves surface plasmon polaritons. Thus, for an s-polarized wave incident onto a weakly rough metal surface, such peaks are not expected to be seen since in this case the incident wave cannot excite surface plasmon polariton at the rough surface [195]. However, for scattering of an s-polarized wave at a dielectric-dielectric interface the $C^{(1)}$ may show peaks [196] even though no surface plasmon polaritons are involved. These peaks originate from multiple scattering processes involving so-called lateral waves [197].

Recently both the memory and reciprocal memory effect have been observed experimentally by West and O'Donnell [190] in the scattering of p-polarized light from a one-dimensional weakly rough gold surface (Fig. 35).

The $C^{(10)}$ correlation function

We now focus on the $C^{(10)}$-correlation function. This correlation function was originally overlooked in the early studies of correlation functions [198] due to the use of the factorization method [191]. By essentially duplicating the arguments used in arriving at Eq. (159), we find in an analogous way that

$$\langle \delta S(q|k)\delta S(q'|k')\rangle \propto 2\pi\delta(q-k+q'-k'), \tag{163}$$

with the consequence that we might write

$$C^{(10)}(q,k|q',k') \propto \frac{2\pi\delta(q-k+q'-k')}{L_1}\, C_0^{(10)}(q,k|q',q'+q+k). \tag{164}$$

Here $C_0^{(10)}(q,k|q',q'+q+k)$ is an envelope function, and both $C^{(10)}$ and its envelope $C_0^{(10)}$ are independent of the length of the randomly rough surface.

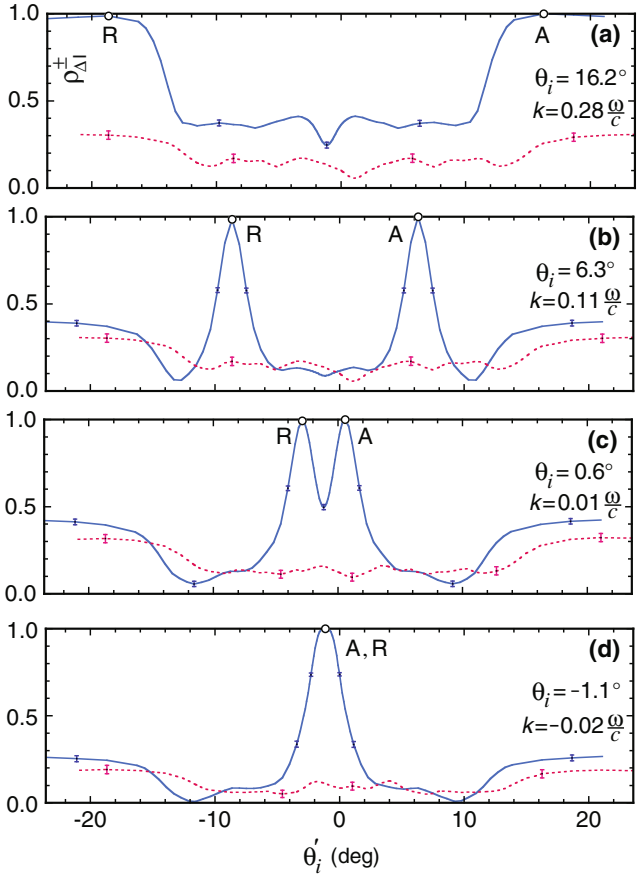

Fig. 35. Experimental measurements of the normalized correlation functions $\rho^{+}_{\Delta I}(k, k', \Delta_{qk})$ (solid lines) and $\rho^{-}_{\Delta I}(k, k', \Delta_{qk})$ (dashed lines) as defined by West and O'Donnell [190] as function of the angle of incidence θ_i'. These correlation functions are these authors equivalent to our envelope functions $\Xi_0^{(1)}(q, k|q', k')$ and $\Xi_0^{(10)}(q, k|q', k')$ (see Ref. [190] for details). The incident light had wavelength $\lambda = 612$nm and the lateral wavenumber transfer was $\Delta_{qk} = 0.04(\omega/c)$. The Gaussian height-distributed gold surface had rms-height $\delta \simeq 15.5$ nm. Its correlation was characterized by a West-O'Donnell (rectangular) power spectrum of parameters $k_- = 0.83(\omega/c)$ and $k_+ = 1.30(\omega/c)$. These values satisfy $k_- < k_{spp} < k_+$ where $k_{spp} = 1.06(\omega/c)$ is the surface plasmon polariton wavenumber, and hence an incident wave of wavenumber k may couple strongly to such modes (when $g(|k_{spp} - k| \neq 0)$. The memory and the time-revised memory peaks are indicated in these figures by A and R, respectively. At these two positions we see that there are perfect correlations. (Adapted after Ref. [190].)

The presence of the δ-function on the right hand side of Eq. (164) is in terms of the wavenumber transfer equivalent to

$$\Delta_{qk} = -\Delta_{q'k'}. \tag{165}$$

What this condition implies for the speckle pattern is that if we change the angle of incidence in such a way that k goes into $k' = k + \Delta k$, a feature originally at $q = k - \Delta q$ will be shifted to $q' = k' + \Delta q$, *i.e.* to a point as much to one side of the new specular direction as the original point was on the other side of the original specular direction. For one and the same incident beam the $C^{(10)}$ correlation function therefore reflects the symmetry of the speckle pattern with respect to the specular direction (see Fig. 33(b)).

The dashed line in Fig. 34 shows the angular dependence, obtained from perturbation theory [189], for the envelope of $C^{(10)}$. The parameters used to obtain these results were the same used to obtain the $C^{(1)}$ correlation shown by the solid line in the same figure. It is seen that

the $C_0^{(10)}$ envelope is a smooth function of θ_s', and in particular does not show any peaks. Moreover, its amplitude is roughly of the same order of magnitude as the $C^{(1)}$ correlation function. This behavior is the same as the one found by West and O'Donnell [190] in their experimental investigation of the $C_0^{(10)}$ envelope (Figs. 35).

It should be pointed out that the $C^{(10)}$ correlation function has no known analogy within scattering from volume disordered system. This new type of correlation in surface scattering was first predicted from perturbation theory by Malyshkin et al. in 1997 [189,199].

5.4.3 Long- and infinite-range correlations

We will now consider the last term of the right hand side of Eq. (158) that gives rise to $C^{(N)}$. Due to the stationarity of the surface

$$\{\delta S(q|k)\delta S^*(q|k)\delta S(q'|k')\delta S^*(q'|k')\} \propto 2\pi\delta(0) = L_1.$$

Hence, the correlation function itself, in light of Eq. (158d), should behave as

$$C^{(N)}(q,k|q',k') \propto \frac{1}{L_1}. \tag{166}$$

It should be noticed that the $C^{(N)}$-correlation function is not constrained in its wavenumbers through δ-functions as we saw earlier was the case for the short-range correlation functions.

Even though we will not address this point explicitly here it has recently been shown that $C^{(N)}$ can be written as a sum of the three following terms [189,199]

$$C^{(N)}(q,k|q',k') = C^{(1.5)}(q,k|q',k') + C^{(2)}(q,k|q',k') + C^{(3)}(q,k|q',k').$$

Here $C^{(1.5)}$ denotes a correlation function of *intermediate-range*, $C^{(2)}$ is a correlation function of *long-range*, while $C^{(3)}$ is an *infinite-range* correlation function. For explicit expressions for these three correlation functions the interested reader is directed to Refs. [189,199,200]. In scattering from bulk disordered systems $C^{(2)}$ [185,187,192] and $C^{(3)}$ [185,186] have their analogies. However, the intermediate range correlation function, $C^{(1.5)}$, predicted theoretically by Malyshkin et al. in 1997 [189,199], has no equivalent in scattering from volume disordered systems. It is unique to scattering from randomly rough surfaces that support surface plasmon polaritons at the frequency of the incident light. An explicit example of such a scattering system is provided by a randomly rough metal surface in p-polarization.

Based on a diagrammatic perturbation theoretical study, Malyshkin *et al.* [189] found that $C^{(1.5)}$ shows a rather rich peak structure. Peaks in $C^{(1.5)}$ are expected to occur for a number of cases in which a linear combination of three of the wavenumbers q, k, q' and k' add up to $\pm k_{spp}$, where k_{spp}, is the wavenumber of the surface plasmon polariton. These conditions are summarized in Table 2. In an expansion of $C^{(1.5)}$ in powers of the surface profile function the leading order is $\mathcal{O}(\zeta^6)$. The intermediate-range correlation function $C^{(1.5)}$ is therefore for a weakly rough surface a result of correlations between a single scattering and a multiple scattering process that involves surface plasmon polaritons. In Fig. 36(a) we have plotted the intermediate-rang correlation function $C^{(1.5)}$ for the randomly rough silver surface that led to the results shown earlier in Fig. 34. In this graphs several peaks are easily seen. Their positions should be compared to the predictions that can be obtained from Table 2.

So far there is no experimental measurements for any of the correlations contained in $C^{(N)}$. In fact such an experimental confirmation represents a real challenge to the experimentalists. The reason is that for long surfaces these correlations are rather small (due to the factor $1/L_1$ in Eq. (166)). In order to be able to observe them, one probably has to use a well-focused incident beam, or a short surface.

Malyshkin et al. [189] also showed perturbatively that the $C^{(2)}$-correlation function should have a peak structure, while the infinite range correlation function, $C^{(3)}$, should be a smooth

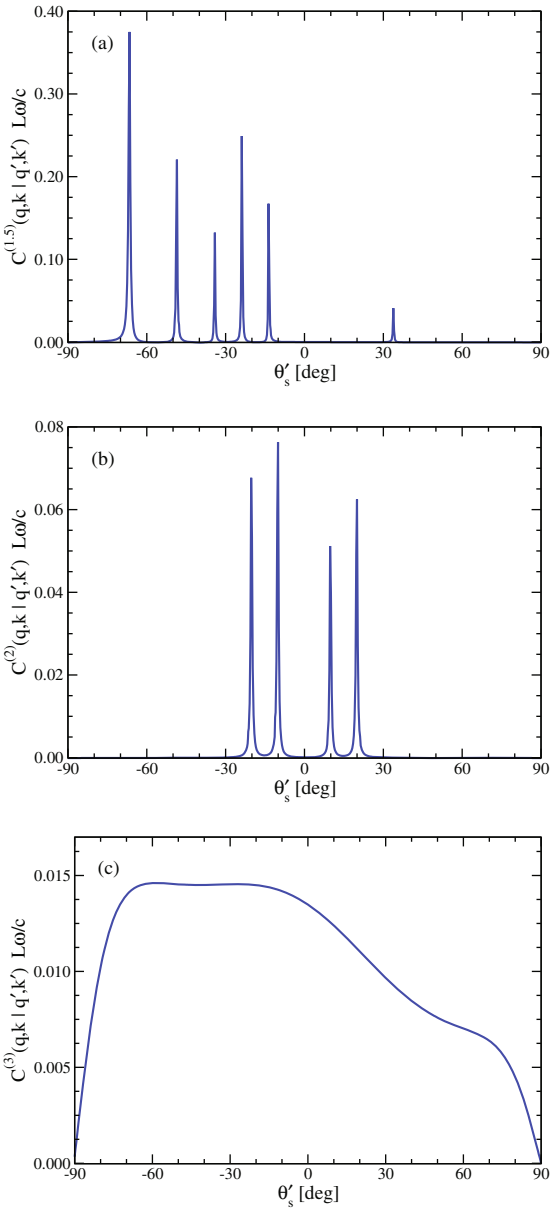

Fig. 36. Perturbative results for the angular dependence of the correlation functions (a) $C^{(1.5)}(q,k|q',k')$, (b) $C^{(2)}(q,k|q',k')$ and (c) $C^{(3)}(q,k|q',k')$ on the scattering angle θ_s' for $\theta_s = -10^\circ$, $\theta_0 = 20^\circ$ and $\theta_0' = 30^\circ$. The remaining parameters were the same used in Fig. 34. (Adapted after Ref. [189].)

function of its arguments. This is seen from the perturbative results plotted in Fig. 36(b) ($C^{(2)}$) and Fig. 36(c) ($C^{(3)}$). The correlations described by the $C^{(2)}$-correlations function are result of correlation between two multiple scattering processes. For weakly rough metal surfaces this correlation function is dominated by double scattering processes. Its peaks are associated with surface plasmon polaritons, as was found to be the case also for $C^{(1.5)}$. The peak conditions for $C^{(2)}$ are that two of the four wavenumbers involved should add/subtract to zero. That is to say that for fixed k, q, and k', peaks are expected when $q' = \pm k'$, $q' = \pm k$ or $q' = \pm q$ (see Table 2). Also the infinite range correlations are due to multiple scattering events. What distinguish the long-range correlation, $C^{(2)}$, from the infinite-range, $C^{(3)}$, is that the latter involves at least

Table 2. The peak conditions for the intermediate range $C^{(1.5)}$ and long range correlation function $C^{(2)}$ for a metallic one-dimensional surface. See text for details.

Correlation function	Peak condition
$C^{(1.5)}$	$-k' + k + q' = -k_{spp}$
$C^{(1.5)}$	$q - q' + k' = k_{spp}$
$C^{(1.5)}$	$q' + q - k' = -k_{spp}$
$C^{(1.5)}$	$q' - k' + q = -k_{spp}$
$C^{(1.5)}$	$k + k' - q' = k_{spp}$
$C^{(1.5)}$	$q' - q + k = k_{spp}$
$C^{(2)}$	$q' = -k$
$C^{(2)}$	$q' = q$
$C^{(2)}$	$q' = -q$
$C^{(2)}$	$q' = k$

one triple scattering process[30]. For more detailed information about $C^{(1.5)}$, $C^{(2)}$, and $C^{(3)}$, the reader is invited to consult Refs. [189,199,200].

5.4.4 Angular intensity correlation functions for strongly rough surfaces

Before ending our discussion of angular intensity correlations functions, we would like to make a few remarks regarding strongly rough surfaces. Above we always assumed that the surface was a weakly rough metal surface. We saw that many of the interesting features of $C(q, k|q', k')$ appeared due to excitations of surface plasmon polaritons. For strongly rough surfaces the excitation of surface plasmon polaritons, if any, is weak, and the dominating mechanism for multiple scattering from such surfaces is multiple scattering of volume waves. As might have been guessed, multiple scattering of volume waves take, for strongly rough surfaces, over the role that surface plasmon polaritons had for weakly rough surfaces. These multiple scattered volume waves give rise to the memory and reciprocal memory effect for strongly rough surface. This is in fact the case for both p- and s-polarized incident light in contrast to what is the case for weakly rough surfaces. This is illustrated by the rigorous computer simulation results of Fig. 37(a) showing the $C_0^{(1)}$ envelope for s-polarized incident light [195]. It is also seen from this figure that as the rms-height of the surface is increased from a value corresponding to a weakly rough surface the memory and reciprocal memory peaks start to emerge in the $C_0^{(1)}$ envelope due to the increased contribution from multiple scattered volume waves.

It was realized recently [195] that a measurement of the angular intensity correlations can provide valuable information regarding the statistical properties of the amplitude of the scattered field. In particular, it was shown that the short-range correlation function $C^{(10)}$ is in a sense a measure of the non-circularity of the complex Gaussian statistics of the scattering matrix. If the random surface is such that only the $C^{(1)}$ and $C^{(10)}$ correlation functions are observed, then $S(q|k)$ obeys complex Gaussian statistics. If the random surface is such that only $C^{(1)}$ is observed, then $S(q|k)$ obeys circular complex Gaussian statistics[31]. This can indeed be seen from Fig. 37(b), which shows that as the surface is made rougher, and therefore $\delta S(q|k)$ approaches a circular complex Gaussian process, the $C^{(10)}$-correlation vanishes as compared to $C^{(1)}$. Finally, if the random surface is such that $C^{(1.5)}$, $C^{(2)}$ and $C^{(3)}$ are observed in addition to both $C^{(1)}$ and $C^{(10)}$, then $\delta S(q|k)$ is not a Gaussian random process at all. However, what kind of statistics $\delta S(q|k)$ obeys in this case is not clear for the moment. These results fits the findings from standard speckle theory [14,184,201] which assumes that the disorder is strong and that $\delta S(q|k)$ constitutes a circular complex Gaussian process.

[30] The leading contribution to $C^{(3)}$ is of order ζ^{10} in the surface profile function $\zeta(x_1)$ [189].

[31] Two complex random variables $A = A_1 + iA_2$ and $B = B_1 + iB_2$ are said to be *circular* complex Gaussian if [14,201] $\langle A_1 B_1 \rangle = \langle A_2 B_2 \rangle$ and $\langle A_1 B_2 \rangle = -\langle A_2 B_1 \rangle$.

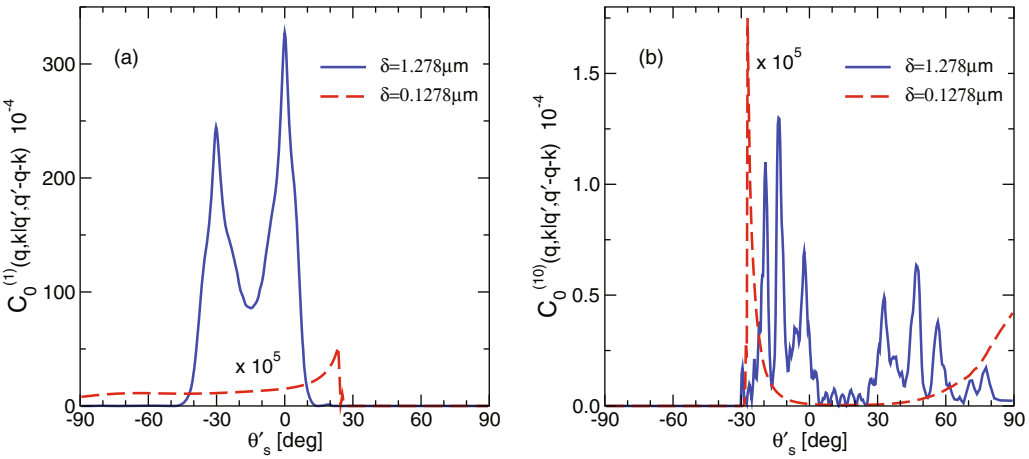

Fig. 37. Rigorous numerical simulation results for the (a) $C_0^{(1)}$ and (b) $C_0^{(10)}$ envelopes as functions of θ_s' for $\theta_0 = 30^\circ$ and $\theta_s = 0^\circ$. The angle θ_0' was determined from the δ-function constraint. The s-polarized incident light had wavelength $\lambda = 632.8\,\text{nm}$. The randomly rough silver surface characterized by a (Gaussian) correlation length $a = 3.85\,\mu\text{m}$. The rms-height of the Gaussian height-distributed surface was $\delta = 1.278\,\mu\text{m}$ (solid line) $\delta = 0.1278\,\mu\text{m}$ (dashed line). As the rms-height is increased one observes that the memory and reciprocal memory peaks start appearing in the envelope of $C^{(1)}$. (After Ref. [195].)

5.5 Second harmonic generation of scattered light

So far in Sec. 5, we have discussed exclusively rough surface scattering phenomena that find their explanation within linear electromagnetic theory. There are still many exciting nonlinear [84–86] surface scattering effects that have to be addressed in the future. Such nonlinear studies are still in their infancies. The studies that have been conducted so far on nonlinear surface scattering effects have mainly been related to the angular distribution of the scattered *second harmonic* generated light [4,9]. In particular what have been studied are some new features in the backscattering directions of the second harmonic light. In this section we will discuss some of these results. The presentation given below follows closely the one given in Ref. [202].

It is well-known from solid state physics that an (infinite) homogeneous and isotropic metal has inversion symmetry [87,88]. A consequence of this is that there is no nonlinear polarization in the bulk. If, however, the metal is semi-infinite with an interface to vacuum, say, the inversion symmetry is broken. Thus, a nonlinear polarization, different from zero, will exist close to the surface. As we move into the bulk of the metal, this effect will become smaller and smaller and finally vanish. Therefore, one might talk about a nonlinear surface layer which, through nonlinear interactions, will give rise to light that is scattered away from the rough surface at the second harmonic frequency.

The scattering system that we will be considering is the by now standard one depicted in Fig. 8. This geometry is illuminated from the vacuum side, $x_3 > \zeta(x_1)$, by a p-polarized plan wave of (fundamental) frequency ω. Only the p-polarized component of the scattered second harmonic generated light will be considered here, even though there also will exist a weak s-polarized component due to the nonlinear interaction at the surface. However, the p-polarized component represents the main contribution to the scattered light at the second harmonic frequency 2ω, and will therefore be our main concern here. Moreover it will be assumed that the generation of the second harmonic light does not influence the field at the fundamental frequency in any significant way.

To motivate the study, we in Figs. 38 show some experimental results (open circles) due to K.A. O'Donnell and R. Torre [203] for the so-called normalized[32] intensity of the second

[32] It can be shown that the total power scattered from a randomly rough surface at the second harmonic frequency is proportional to the square of the irrandiance, the incident power per unit area,

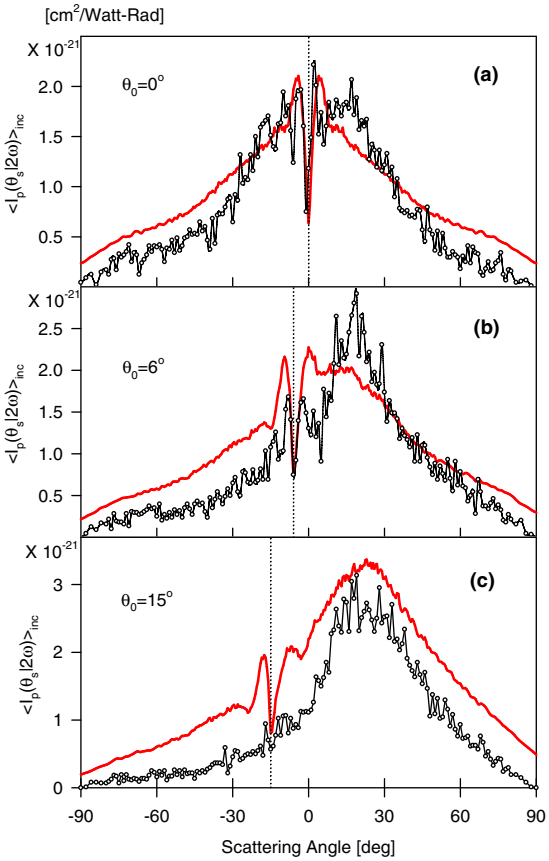

Fig. 38. The mean normalized second harmonic intensity as a function of the scattering angle θ_s for the scattering of p-polarized light from a randomly rough silver surface. The surface was characterized by a Gaussian height distribution of rms-height $\delta = 1.81\,\mu$m, as well as a Gaussian correlation function of correlation length $a = 3.4\,\mu$m. The dielectric constants were at the fundamental and second harmonic frequency $\varepsilon(\omega) = -56.25 + i0.60$ and $\varepsilon(2\omega) = -11.56 + 0.37$ respectively. The thick lines represent the results of numerical simulations and the open circles represent the experimental results of O'Donnell and Torre [203]. The incident plane wave had a wavelength $\lambda = 1.064\,\mu$m. In the numerical simulations the surface had length $L = 40\lambda$ and it was sampled with an interval $\Delta x_1 = \lambda/20$. The numerical results were averaging over $N_\zeta = 2000$ realizations of the surface, and the angles of incidence were (a) $\theta_0 = 0°$, (b) $\theta_0 = 6°$, and (c) $\theta_0 = 15°$. (Adapted after Ref. [202].)

harmonic light scattered incoherently from a strongly rough silver surface. The surface was characterized by Gaussian height statistics of rms-height $\delta = 1.81\,\mu$m and a Gaussian correlation function of correlation length $a = 3.4\,\mu$m. The wavelength of the incident light was $\lambda = 2\pi c/\omega = 1.064\,\mu$m, while the angles of incidence considered were $\theta_0 = 0°$, $6°$, and $15°$ as indicated in Fig. 38. For completeness and comparison the corresponding mean DRCs for the linear problems at frequencies ω and 2ω are given in Figs. 39.

The most noticeable feature of the experimental results of the scattered second harmonic light (open circles) shown in Figs. 38 are, without question, the *dips* seen in the backscattering direction for which the intensity of the light scattered linearly by the same rough surface shows enhanced backscattering *peaks* (Figs. 39). So why do we have a dip for the intensity of the scattered second harmonic light at the backscattering direction, and, for instance, not a peak?

on the surface. One therefore defines the normalized intensity of the scattered second harmonic light so that it is independent of the incident power. The analytic expressions for this quantity can be found in Eq. (34) of Ref. [202].

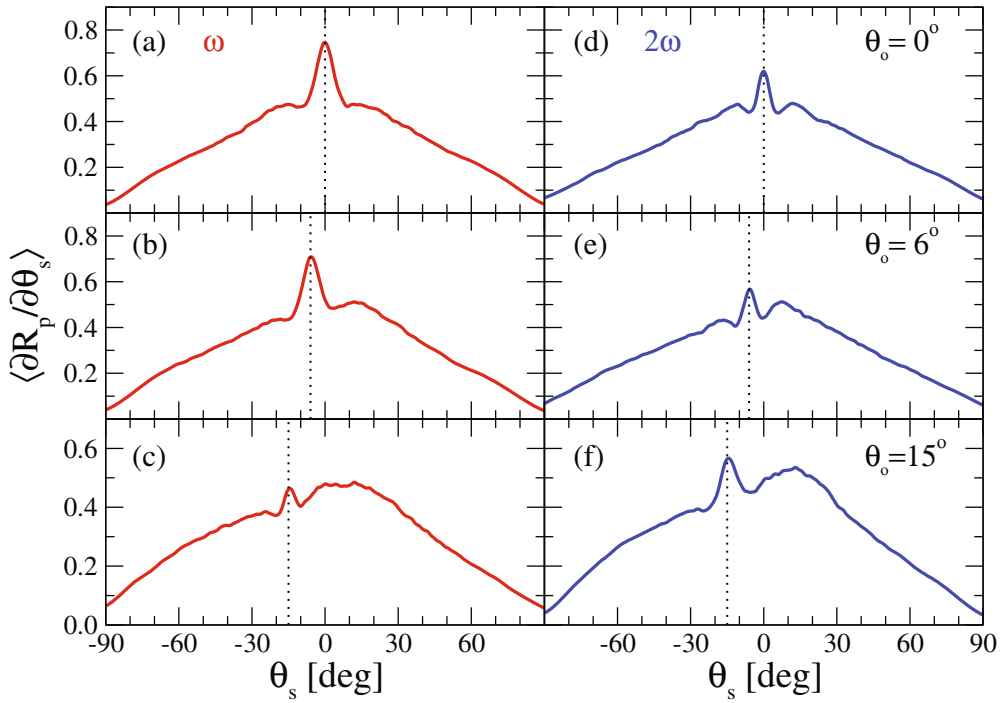

Fig. 39. Similar to Figs. 38, but now showing rigorous computer simulation results for the mean differential reflection coefficient $\langle \partial R_p/\partial\theta_s \rangle$ for the linear problems at frequencies ω (Figs. 39(a)–(c)) and 2ω (Figs. 39(d)–(e)) as well as angles of incidence $\theta_0 = 0°$, $6°$ and $15°$. The vertical dashed lines indicate the backscattering directions. The remaining parameters are given in the caption of Figs. 38.

5.5.1 Strongly rough surfaces: A numerical simulation approach to the second harmonic generated light

With the help of numerical simulations, we will try to present a deeper understanding of what causes these dips. The nonlinear layer existing along the surface is of microscopic dimensions. Since we are working with the macroscopic Maxwell's equations it is natural to assume that this layer is infinitely thin. Under this assumption, the effect of the nonlinear boundary layer is accounted for in the boundary conditions to be satisfied by the field, and its normal derivative, at the second harmonic frequency. These boundary conditions have jumps at the nonlinear interface, and their degree of discontinuity depends on the nonlinear polarization, or equivalently, on the parameters that describes this polarization. The form of the (nonlinear) boundary conditions at the second harmonic frequency 2ω can be written in the form [202]

$$\mathcal{F}_\nu^+(x_1|2\omega) - \mathcal{F}_\nu^-(x_1|2\omega) = \mathcal{A}(x_1), \tag{167a}$$

$$\mathcal{N}_\nu^+(x_1|2\omega) - \mathcal{N}_\nu^-(x_1|2\omega) = \mathcal{B}(x_1), \tag{167b}$$

where the sources $\mathcal{F}_\nu$ and $\mathcal{N}_\nu$ have been defined in Eqs. (128). As before, the superscripts $\pm$ denote the sources evaluated just above $(+)$ and below $(-)$ the rough surface defined by $x_3 = \zeta(x_1)$. The functions $\mathcal{A}(x_1)$ and $\mathcal{B}(x_1)$ are related to the nonlinear polarization $\mathbf{P}(x_1, x_3)$ through the integral of this quantity over the nonlinear boundary layer [202]. To fully specify the nonlinearity of the problem, the polarization $\mathbf{P}(x_1, x_3)$ has to be specified. For instance for a free electron model, that we will consider here for simplicity, it takes on the form [204–206]

$$\mathbf{P}(x_1, x_3) = \gamma\nabla\left(\mathbf{E}\cdot\mathbf{E}\right) + \beta\mathbf{E}\left(\nabla\cdot\mathbf{E}\right). \tag{168a}$$

Here the constants γ and β are defined as

$$\gamma = \frac{e^3 n_0(\mathbf{r}_\perp(x_1, x_3))}{8m^2\omega^4}, \tag{168b}$$

$$\beta = \frac{e}{8\pi m\omega^2}, \tag{168c}$$

where n_0 is the electron number density, $\mathbf{r}_\perp(x_1, x_3)$ is a vector normal to the local surface at point (x_1, x_3), and e and m are the charge and mass of the electron, respectively. The explicit expressions for $\mathcal{A}(x_1)$ and $\mathcal{B}(x_1)$ can, within this model, be found in Ref. [202].

Since the surfaces used in the experiments leading to the results shown in Figs. 38 are strongly rough, perturbation theory does not apply, and one has in theoretical studies to resort to rigorous numerical calculations of the second harmonic scattered light. Such kind of simulations are conducted on the basis of the rigorous simulation approach presented in Sec. 4.10. The calculations are now, however, made out of two main steps: First, one calculates the (linear) source functions $\mathcal{F}_\nu(x_1|\omega)$ and $\mathcal{N}_\nu(x_1|\omega)$; the field and it's normal derivative evaluated on the surface at the fundamental frequency ω. This is done exactly as described in Sec. 4.10. From the knowledge of the linear sources functions at the fundamental frequency, the right-hand-side of the boundary conditions (167) can be calculated since they depend directly on these source functions as well as on the form of the nonlinear polarization $\mathbf{P}(x_1, x_3)$ [202]. In all numerical results to be presented later in this section the form for the nonlinear polarization given by Eq. (168) will be used. With the functions $\mathcal{A}(x_1)$ and $\mathcal{B}(x_1)$ available, the nonlinear sources, $\mathcal{F}^{\pm}_\nu(x_1|2\omega)$ and $\mathcal{N}^{\pm}_\nu(x_1|2\omega)$, are readily calculated from an approach similar to the one described in detail in Sec. 4.10. The only main difference is that now the boundary conditions to be used when coupling the two integral equations are the nonlinear boundary conditions given in Eqs. (167). With the source functions both for the fundamental and second harmonic frequency available, all interesting quantities about the scattering process, both linear and nonlinear, are easily obtained. The full details of this approach can be found in Ref. [202].

Based on this numerical approach, we compare in Figs. 38 the numerical simulation results (solid lines) obtained by Leyva-Lucero et al. [202] to the experimental results obtained by O'Donnell and Torre (open circles) [203]. The dielectric constants used in the simulations were at the fundamental frequency $\varepsilon(\omega) = -56.25 + i0.60$ and $\varepsilon(2\omega) = -11.56 + i0.37$ at the second harmonic frequency. Indeed by comparing the experimental and theoretical results shown in Figs. 38, a nice correspondence is observed both qualitatively and quantitatively. Particular in light of the oversimplified model used in the simulations for the nonlinear interaction, the agreement is no less then remarkable.

From the experimental and theoretical results shown in Figs. 38(a), a clear dip is seen in the incoherent component of the mean normalized second harmonic intensity for the backscattering direction $\theta_s = 0°$. For the linear scattering problem, however, there is an enhancement at the same scattering angle (Figs. 39). So what is the reason for the dip in the intensity of the scattered second harmonic light? O'Donnell and Torre [203], that conducted the experiments leading to the results shown in Figs. 38, suggested that these dips were due to coherent effects. In particular they suggested that the dips originated from destructive interference between waves scattered multiple times in the valleys of the strongly rough surface. Since the numerical simulation approach seems to catch the main physics of the second harmonic generated light, it might therefore serve as a useful tool for testing the correctness of the suggestion made by of O'Donnell and Torre [203].

This can be done by applying a single scattering approximation to the generation of the second harmonic light. As described above, the numerical approach leading to the theoretical results shown as solid lines in Figs. 38, consists mainly of a linear and nonlinear step where each step is solved essentially by some variant of the approach presented in Sec. 4.10. By using a single scattering approach, like the Kirchhoff approximation [30,141,207], to both steps of the calculation, a single scattering approximation for the full problem is obtained. The single scattering processes included in such a calculation are illustrated in Figs. 40. Notice that also unphysical scattering processes like the one shown in Fig. 40(b), are included in this approximation.

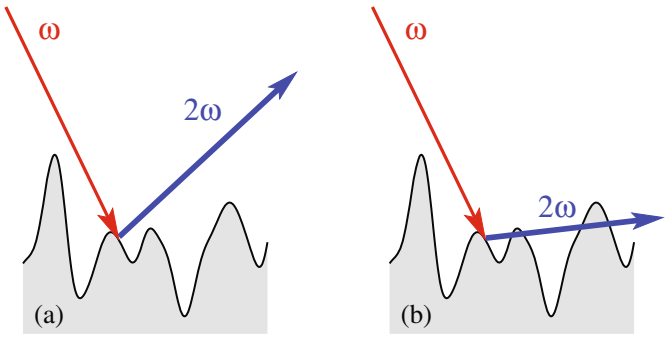

Fig. 40. Diagrams illustrating two of the single scattering processes that produce the second harmonic scattered light in a single scattering approach. The thin red arrows represent light of frequency ω, while the thick blue arrows represent light of frequency 2ω. Notice that the process in Fig. 40(b) is unphysical. (Adapted after Ref. [202].)

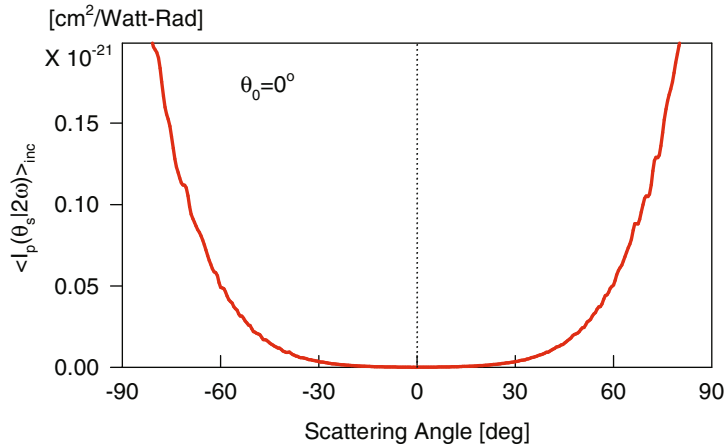

Fig. 41. The mean normalized second harmonic intensity $\langle I_p(\theta_s|2\omega)\rangle_{inc}$ as a function of the scattering angle θ_s calculated in a single scattering approximation. The angle of incident of the light was $\theta_0 = 0^\circ$, while the remaining parameters used in the simulation were those given in the caption of Figs. 38. (Adapted after Ref. [202].)

In Fig. 41 we present (for $\theta_0 = 0^\circ$) the consequence for the angular dependence of the normalized intensity $\langle I_p(\theta_s|2\omega)\rangle$ of only including single scattering processes in the second harmonic generation. From this figure it is easily seen that the intensity of the second harmonic generated light calculated in a single scattering approximation does *not* give rise to a dip (or peak) in the backscattering direction. In fact, the overall angular dependence of $\langle I_p(\theta_s|2\omega)\rangle$ in the single scattering approximation is quite different from the one obtained by the rigorous approach described above. Similar result holds for the other two angles of incidence considered in Figs. 38. Hence, one may conclude that the dips present in the backscattering direction of the incoherent component for the mean second harmonic generated light is not due to single scattering. It therefore has to be a multiple scattering phenomenon.

To look more closely into this, the authors of Ref. [202] used an iterative approach for the linear part of the scattering problem which enabled them to calculate the scattered fields according to the order of the scattering process. Such a (Neumann-Liouville) iterative approach has been developed and used earlier in the literature [66,208,209]. For the nonlinear part of the calculation the rigorous simulation approach was used and thus all higher order scattering processes were here taken into account. Some of the processes accounted for by this procedure and which give rise to the second harmonic light is depicted in Figs. 42.

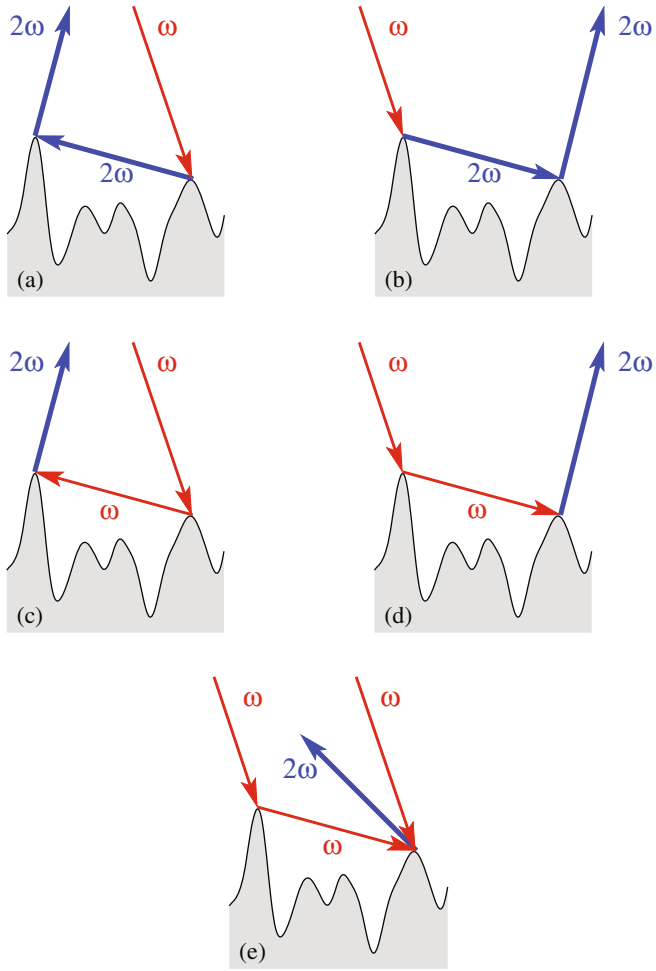

Fig. 42. Diagrams illustrating some of the multiple scattering processes that produce the second harmonic scattered light. The thin red arrows represent light of frequency ω, while the thick blue arrows represent light of frequency 2ω. (Adapted after Ref. [202].)

We notice that the processes depicted in Figs. 42(a) and (b) represent single scattering in the linear part and are thus taken properly into account by using the standard Kirchhoff approximation [141,207] (for the linear part). However, for the paths shown in Figs. 42(c) and (d), one needs to consider a pure double scattering approximation (for the linear part) in order to include these processes properly. In Figs. 43 the simulation results for the second harmonic light $\langle I_p(\theta_s|2\omega)\rangle$ are shown for the case where a single scattering (Fig. 43(a)) and a pure double scattering (Fig. 43(b)) approximation are used for the linear part of the scattering process. In both cases dips in the backscattering direction are observed. In order to obtain the solid curve of Fig. 43(c) *both* single and double scattering processes were taken into account for the linear part of the calculation. This result will, therefore, include any interference effect between the paths shown in Figs. 42. The dashed line in Fig. 43(c) is the sum of the curves shown in Figs. 43(a) and (b). It does therefore not contain any interference effects between type I paths (Figs. 42(a)–(b)) and type II paths (Figs. 42(c)–(d)). That the two curves shown in Fig. 43(c) are so close to each other tells us that the interference between type I and type II paths are rather small (if any). Furthermore, paths of the type illustrated in Fig. 42(e) do not seem to be important, and they do not have coherent partners.

The numerical results presented so far for the intensity of the second harmonic scattered light seem to indicate that the behavior in the backscattering direction is affected by

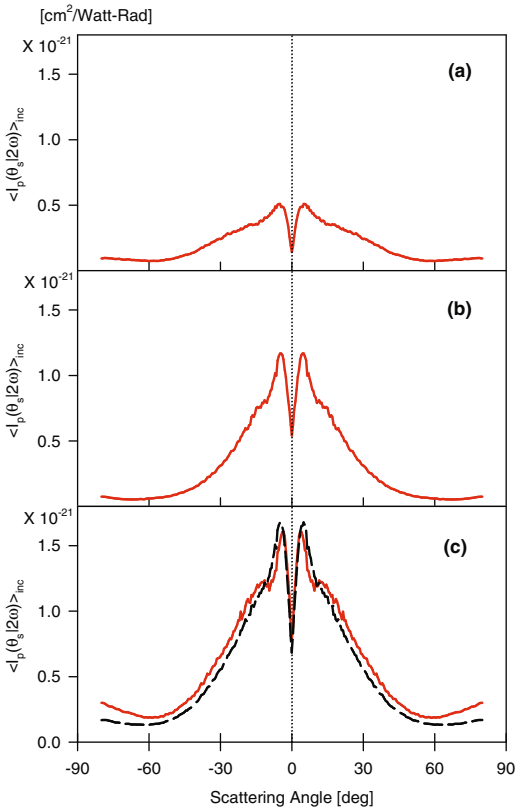

Fig. 43. Calculations of the mean normalized second harmonic intensity as a function of the scattering angle θ_s for the scattering of p-polarized light from a random silver surface where the linear part of the problem was solved by iteration. The angle of incidence of the light was $\theta_0 = 0^\circ$ and the other parameters of the simulation were as in Figs. 38. The curves have, (a) the single scattering contributions in the linear scattering and all contributions at the second harmonic frequency, (b) pure double scattering contributions in the linear scattering and all contributions at the second harmonic frequency, and (c) the single and double scattering contributions in the linear scattering and all contributions at the second harmonic frequency. In (c), the curve shown with the dashed line represents the sum of the curves shown in (a) and (b). (Adapted after Ref. [202].)

interference between the paths of either type I or type II. In the backscattering direction, there is no phase difference due to optical path difference between, say, the two type I paths, and with a similar argument holding for the type II paths. Hence, any phase difference between the two paths has to come from phase shifts during the reflection. In the linear multiple-scattering processes giving rise to enhanced backscattering the phase shifts due to reflection will be the same for the two processes because the local Fresnel coefficients are *even* functions of the angle of incidence. Hence, the two paths in the backscattering direction will for the full linear problem both have the same phase and hence interferer constructively giving rise to the celebrated enhanced backscattering peak. However, for multiple scattering processes involving second harmonic generated light the situation is quite different. The reason for this is that the local nonlinear Fresnel coefficient is not an even, but an *odd* function of the angle of incidence [202]. Hence, the phase difference between the two type I paths, say, will not in general be zero any more since the phases for these two paths will add instead of subtract. If this phase shift is positive in Fig. 42(a), say, then it will be negative for the path shown in Fig. 42(b) since the local angle of incidence in the two cases have different sign and the local nonlinear Fresnel reflection coefficient is an odd function of the angle of incidence. Hence, in the nonlinear case the phase difference in the backscattering direction is different from zero for the paths that

seem to interfere. From the numerical results shown in this subsection, they in fact seem to be close to π out of phase resulting in destructive interference, or a dip in $\langle I_p(\theta_s|2\omega)\rangle$ at the backscattering direction as compared to its background.

5.5.2 Weakly rough surfaces

We have so far presented both experimental and numerical results for the second harmonic generated light scattered from strongly rough surfaces. However, experiments for weakly rough surfaces have also been conducted [210]. The results are quite similar to the experimental results presented in Figs. 38. In particular, also the second harmonic generated light scattered from weakly rough surfaces show dips in the backscattering direction. However, in theoretical studies [211–213] *both* dips and peaks in the backscattering direction have been predicted. If it is a peak or dip depends on the values used for the nonlinear phenomenological constants. Even though predicted theoretically, only dips have so far been seen in experiments.

For weakly rough surface the scattering processes giving rise to these dips (or peaks) are believed to be different for weakly and strongly rough surfaces. This situation resembles closely what was found for the origins of the enhanced backscattering peak for weakly and strongly rough surfaces. Indeed, for weakly rough surfaces the origin of the dip in the intensity of the diffusely scattered light at frequency 2ω is intimately related to the excitation of surface plasmon polaritons at this frequency [212,213]. Thus such dips are not to be expected for the second harmonic light generated in *s*-polarization from weakly rough surfaces.

5.6 Scattering from two-dimensional random surfaces

So far in this review, we have mainly considered one-dimensional roughness. To obtain theoretical and numerical solutions to the scattering problem, the assumption that the surface roughness is one-dimensional, reduces the complexity and challenge of the problem considerably, since a scalar wave equation can be used for its description. This in particular applies to the case when multiple scattering effects are studied and for which rigorous simulation approaches often are required. Due to this main reason, electromagnetic wave scattering from one-dimension rough surfaces has attracted the most attention in the literature. However, it is a fact, that most natural occurring and many man-made surfaces are two-dimensional, so the two-dimensional scattering problem is well worth investigating in more detail.

The main difference between the electromagnetic wave scattering from a one- and two-dimensional randomly rough surface, is that the latter scattering geometry allows for so-called *cross-polarization*, *i.e.* scattering where the incident and scattered (or transmitted) light have *different* polarizations. Furthermore, cross-polarized scattering (or transmission) observed in the plane of incident is a consequence of multiple scattering. For a one-dimensional scattering geometry[33], the polarization of the scattered (and transmitted) light is *always* that of the incident light and all the intensity of the scattered (or transmitted) light is distributed in this plane. However, for a two-dimensional scattering geometry, the intensity, and particularly the polarization of the scattered light, are complex functions of the scattering angles.

As was seen in Sec. 5.2.1, the initial experimental studies of the enhanced backscattering phenomenon was done for two-dimensional randomly rough surfaces where one focused on the in-plane scattering (Fig. 21) [168,169]. Subsequent experimental studies measured the full angular distribution of the intensity of the light, both co- and cross-polarized, scattered on metallic [214] and dielectric [215] two-dimensional randomly rough surfaces. In parallel with this experimental activity, numerous theoretical and numerical studies, using both rigorous and approximate approaches, were performed for two-dimensional scattering problems [36,67,104,105,216–226]. However, only recently have the full angular intensity distributions of the light

[33] This is the geometry discussed extensively in Sec. 4, *i.e.* where the rough surface is one dimensional, the plane of incidence is perpendicular to the grooves of the surface, and the electric field vector is either parallel or perpendicular to this plane.

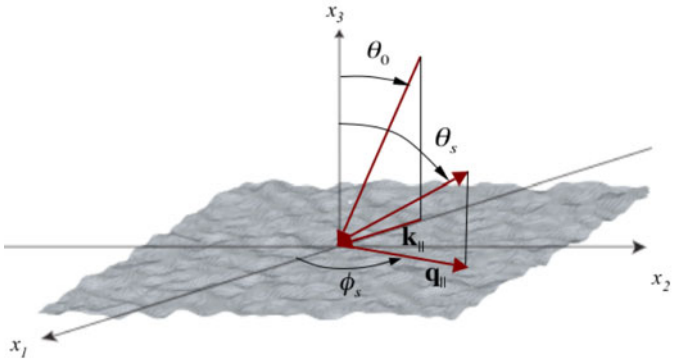

Fig. 44. An illustration of the two-dimensional scattering geometry defining the coordinate system used as well as the polar (θ) and azimuthal (ϕ) angles of incidence and scattering.

scattered from strongly two-dimensional rough surfaces been approached by rigorous methods due to the computational difficulties of the problem [224,225].

In order to illustrate and further investigate some of the interesting features and characteristics of the two-dimensional electromagnetic scattering problem, we start by defining the relevant scattering geometry that will be considered (Fig. 44). The surface profile function is defined by, $x_3 = \zeta(\mathbf{x}_\parallel)$, where $\mathbf{x}_\parallel$ denotes the projection of the spatial vector $\mathbf{x}$ onto the x_1x_2-plane. The profile function, $\zeta(\mathbf{x}_\parallel)$, is assumed to have the statistical properties

$$\left\langle \zeta(\mathbf{x}_\parallel) \right\rangle = 0, \tag{169a}$$

$$\left\langle \zeta(\mathbf{x}_\parallel)\zeta(\mathbf{x}'_\parallel) \right\rangle = \delta^2 \, W\left(\left| \mathbf{x}_\parallel - \mathbf{x}'_\parallel \right| \right), \tag{169b}$$

that are similar to those defined in Eqs. (3) and (4) for the one-dimensional profile function. In Eqs. (169), δ denotes the rms-roughness of the surface; $W(\cdot)$ is the (lateral) height-height correlation function; and $\langle\cdot\rangle$ signifies an average over an enable of realizations of the surface roughness. Above the surface, $x_3 > \zeta(\mathbf{x}_\parallel)$, the medium is vacuum, and below the surface (the substrate), one has a metal or dielectric characterized by a frequency dependent dielectric constant $\varepsilon(\omega)$. The direction of the incident light is defined by the polar and azimuthal angles of incidence, θ_0 and ϕ_0, respectively, and in a similar fashion the direction of the scattered field is determined by the angles of scattering θ_s and ϕ_s (Fig. 44). Notice specially for what directions these angles are defined to be positive.

For the case study that we will concern ourselves with in this section, it has been assumed, for simplicity, that the substrate ($x_3 < \zeta(\mathbf{x}_\parallel)$) consists of a perfect electric conductor (PEC) for which $\varepsilon(\omega) = -\infty$. The surface profile function was characterized by an rms-height $\delta = \lambda$ with λ the wavelength of the incident light. Moreover, the correlation function of the surface roughness, $W(\cdot)$, was taken to be Gaussian with a correlation length $a = 2\lambda$. For such roughness parameters, the surface can be considered to be strongly rough [29] and one expects that the intensity of the scattered light will receive substantial contributions from multiple scattering events. For those reasons, any perturbative treatment of this scattering problem will, for these surface parameters, most probably fail considerably. Hence, a rigorous numerical treatment based on a surface integral technique is the most suitable approach for solving this problem although it is rather computationally expensive and challenging [67,224].

Similar to what was done in Sec. 4.10 for the one-dimensional case, a coupled inhomogeneous two-dimensional integral equation can be formulated for the tangential components of the electromagnetic field – the surface currents. It is not our intention to here show how this can be done, and the interested reader is directed to the literature for details [145,146,224,225]. From the solution of this integral equation, the scattered field can be calculated everywhere from the Stratton-Chu and/or Franz formulas [4,145,146,224,225]. In particular, one can defined and calculated the mean differential reflection coefficient, $\langle \partial R_{\beta\alpha}/\partial\Omega_s \rangle$, corresponding to

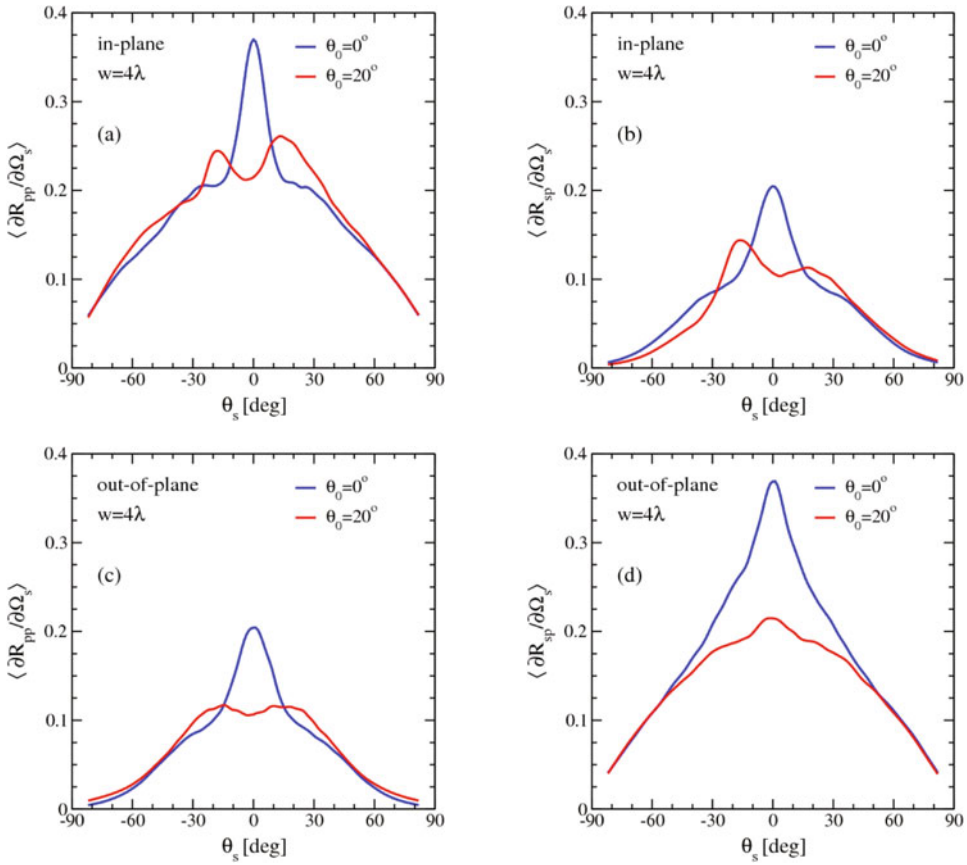

Fig. 45. The mean differential reflection coefficients, $\langle \partial R_{\beta\alpha}/\partial\Omega_s \rangle$ ($\alpha \to \beta$), as functions of the polar scattering angle θ_s for the in-plane ($\phi_s = \phi_0$ or $\phi_s = \phi_0 + 180^\circ$) (a) co-polarized ($p \to p$) and (b) cross-polarized scattering ($p \to s$), and the out-of-plane ($\phi_s = \phi_0 \pm 90^\circ$) (c) co-polarized ($p \to p$) and (d) cross-polarized scattering ($p \to s$) of a p-polarized incident beam ($\alpha = p$) of width $w = 4\lambda$ ($\theta_0 = 0^\circ$ and $\theta_0 = 20^\circ$; $\phi_0 = 0^\circ$) scattered from a Gaussian randomly rough perfectly conducting surface. The Gaussian correlated surface had a correlation length $a = 2\lambda$ and an rms-height $\delta = \lambda$. To facilitate comparison between the various configurations presented in this figure, notice that we have used similar scales for all ordinate axes. Moreover, to simplify the presentation of the figures, a convention was adopted where negative (positive) values of θ_s correspond to $\phi_s = \phi_0 + 180^\circ$ ($\phi_s = \phi_0$). (After Ref. [224].)

the polarization of the incident (α) and scattered (β) light. This quantity is defined as the ratio between the time-averaged power scattered and incident on the surface in an analogous way to how it was defined for the one-dimensional case in Sec. 4.3 and 4.10 (*c.f.* Ref. [224] for details). Moreover, from the expressions for the scattered fields corresponding to various states of polarization of the incident light, the 16 elements of the Müeller matrix of the rough surface can (in principle) be obtained [227–231]. With the knowledge of this matrix, the full polarization response of the rough surface, including co- and cross-polarization, is completely described for any state of polarization of the incident light.

In Fig. 45 we present the mean differential reflection coefficients as functions of the polar scattering angle θ_s for the in-plane ($\phi_s = 0^\circ$) and out-of-plane ($\phi_s = \pm 90^\circ$), co- ($p \to p$) and cross-($p \to s$) polarized scattered light due to a p polarized Gaussian beam incident on the surface. The results depicted in Figs. 45 were obtained as averages over 12,000 realizations of the surface profile function. The area of the surface was $16\lambda \times 16\lambda$ that was discretized on a 112×112 grid of points corresponding to a discretization interval of $\lambda/7$ for both directions. The width of the incident Gaussian beam used was 4λ. It was noted when obtaining these results

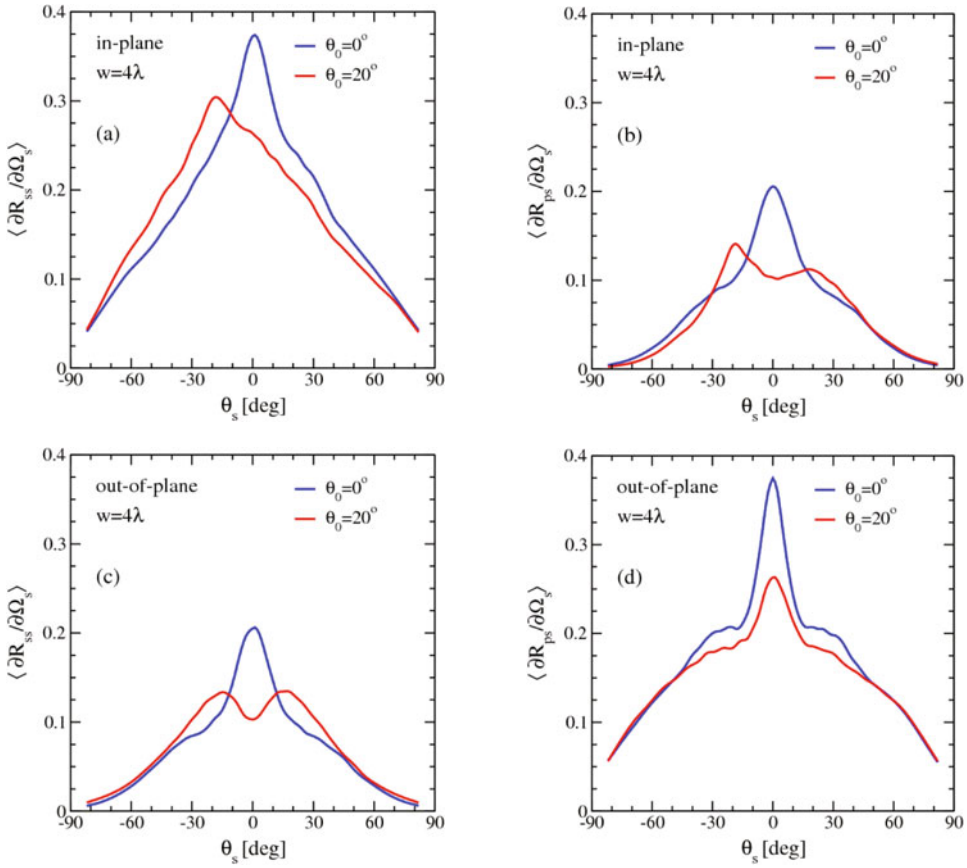

Fig. 46. Same as Fig. 45, but for an *s*-polarized incident beam. (After Ref. [224].)

that at least for the roughness parameters assumed, the contribution to the mean differential reflection coefficient from the light scattered coherently is smaller than the contribution from the light scattered incoherently by a factor of approximately 10^{-4}.

It should be noted that there is no single scattering contribution in the cases of in-plane cross-polarized (Fig. 45(b)) and out-of-plane co-polarized (Fig. 45(c)) scattering. This we believe is the main reason for the reduced amplitude of the mean differential reflection coefficients in these cases relative to those of Fig. 45(a) and (d) where single scattering is allowed. The peaks at $\theta_s = 0°$ and $-20°$ [34] for in-plane co-polarized scattering (Figs. 45(a)) are enhanced backscattering peaks [215,232–234]. However, the structures seen as peaks in the backscattering directions of the cross-polarized scattering, Fig. 45(b), are not real peaks, as will be seen below from the full angular intensity distributions. The results that the mean differential reflection coefficients for out-of-plane co- and cross-polarized scattering (Figs. 45(c) and (d)) are even functions of θ_s are consequences of the scattering geometry, namely that $\phi_0 = 0°$, $\phi_s = \pm 90°$, and the isotropy of the power spectrum of the surface roughness.

We present in Fig. 46 corresponding results to those of Fig. 45, but now for an *s*-polarized incident Gaussian beam. There is no single scattering contribution to the in-plane cross-polarized and out-of-plane co-polarized scattering, as in the case of *p* polarization. Also in this case the peaks seen in the in-plane co-polarized scattering (Fig. 46(a)) are enhanced backscattering peaks, while the structures seen in the in-plane cross-polarized scattering (Fig. 46(b)) in the backscattering direction are not real peaks.

[34] When in the text discussing the results of Figs. 45 and 46, we follow the sign convention for θ_s introduced in the caption of Fig. 45. Elsewhere, however, the standard spherical coordinate convention ($\theta_s \geq 0°$) will be followed.

The full angular distributions of the intensity of the scattered light, as obtained by a rigorous computer simulation approach, are presented as color contour plots for either p or s polarized incident beam and polar angles of incidence $\theta_0 = 0°$ (Figs. 47); 20° (Figs. 48); and 40° (Figs. 49) ($\phi_0 = 0°$ for all cases). It is observed from Figs. 47–49 that the angular intensity distributions of the scattered light, for given polarizations of the incident light, are far from trivial and show strong and complex angular dependencies.

For instance, for p-polarized normal incident light that is scattered by the surface into p- and s-polarized light (*i.e.* polarization not recorded), Fig. 47(a), the angle-dependent scattering is for the most part rather isotropic, except for a slight anisotropy seen as an elongated (along the q_2-direction) structure around the normal scattering direction. This structure is caused by the wider intensity distribution in the direction perpendicular to the direction of the incident electric field as compared to the intensity distribution along it[35]. The central peak present in Fig. 47(a) is the enhanced backscattering peak, and is not related to specular scattering which for these roughness parameters can be neglected [224]. A similar behavior is seen for the scattering of (normally) incident s-polarized light into either p- or s-polarized light (Fig. 47(b)). Also here an apparent enhanced backscattering peak is observed. In the case of s-polarization, one sees though that the central anisotropic portion of the scattering has a different orientation compared to that in the case of p-polarization. It remains true, however, that there is a stronger scattering perpendicular to the (average) direction of the incident electric field independent of the polarization of the incident light.

It should be noted that with the full angular intensity distributions of the scattered light available, the energy conservation (unitarity) of the simulations performed can be explicitly checked by comparing the power incident on the surface to that scattered from it

$$\mathcal{U}_\alpha = \sum_{\beta=p,s} \int d\Omega_s \left\langle \frac{\partial R_{\beta\alpha}}{\partial \Omega_s} \right\rangle . \tag{170}$$

According to the definition of the mean differential reflection coefficient, one should have $\mathcal{U}_\alpha = 1$ if there is no absorption (or transmission) and the incident light is α-polarized [224]. For normal incidence, for instance, one from the simulation results obtains $\mathcal{U}_p = 0.9976$ and $\mathcal{U}_s = 0.9970$ for p- and s-polarized incident light, respectively. For the other angles of incidence considered, $\theta_0 = 20°$ and 40° (Figs. 48 and 49), energy conservation was satisfied within 0.5% or better. Even if energy conservation is only a necessary requirement, such results, however, still testify to the accuracy of the simulations and the approaches used to obtain them.

For the simulation results presented in Figs. 47(a)–(b) the incident light was either p- or s-polarized while, on the other hand, the polarization was *not* recorded for the scattered light. However, the simulation approach used allows also to study the angular intensity distributions of the polarized scattered light. An interesting question is therefore how the intensity of the scattered light of *given* linear polarization is distributed. Will the p- and s-polarized scattered light be distributed in more-or-less the same way? In fact, this is rather far from being true. In Figs. 47(c) and (d) we present the scattering into p-polarized scattered light from, respectively, a (normally) incident p- and s-polarized Gaussian beam. Similarly, depicted in Figs. 47(e) and (f) are the scattering into s-polarized scattered waves for an incident p- or s-polarized Gaussian beam. We note that taking the sum of the distributions shown in *e.g.* Figs. 47(c) and (e) produces the angular distribution shown in Fig. 47(a). From Figs. 47(c)–(f) it follows that the intensity distributions for scattering from one polarization into another, or into the same one, show a dipole-like angular dependence.

For co-polarized scattering, *i.e.* the polarization of the incident light and the (recorded) polarization of the scattered light are the same, the "forward direction" of the dipole-like pattern is oriented along q_1 (Figs. 47(c) and (f)), while for cross-polarization, it is oriented along the q_2

[35] Note that for an incident p-polarized Gaussian beam the electric field vector is in the plane of incidence, the q_1q_3-plane, while for an s-polarized beam the same vector is perpendicular to this plane.

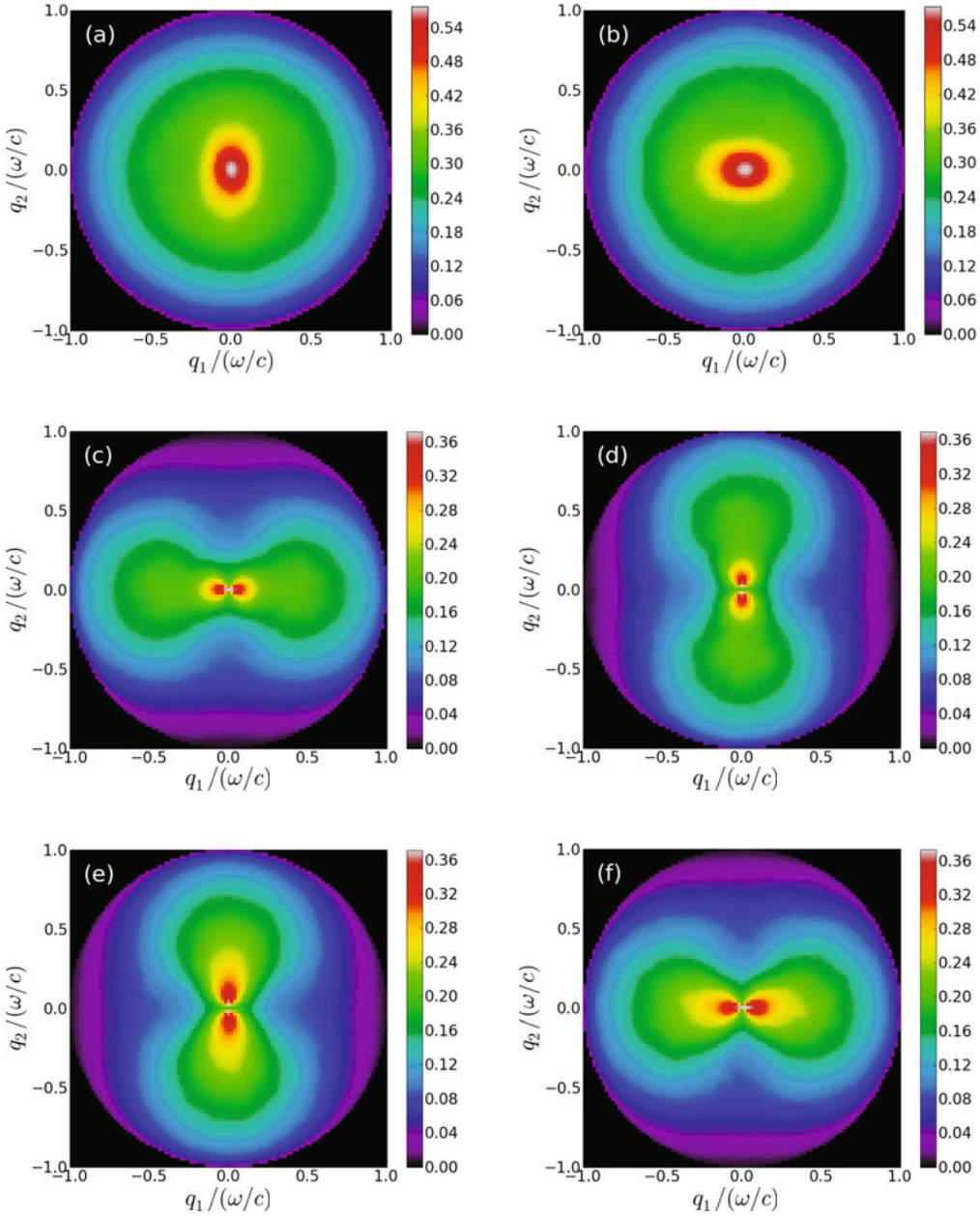

Fig. 47. The complete angular distributions of the mean differential reflection coefficient, $\langle \partial R_{\beta\alpha}/\partial\Omega_s \rangle$, for the scattering of an α-polarized Gaussian beam incident on the surface at polar angle $\theta_0 = 0^\circ$ and azimuthal angle $\phi_0 = 0^\circ$. The perfectly conducing rough surface was characterized by a Gaussian height distribution of rms-value $\delta = \lambda$ and a Gaussian correlation function of transverse correlation length $a = 2\lambda$. The incident beam was p-polarized in Figs. 47(a), (c) and (e) [left column]; and s-polarized in Figs. 47(b), (d) and (f) [right column]. Moreover, in the top two figures [Figs. 47(a) and (b)] the polarization of the scattered light was not recorded; in Figs. 47(c) and (d) [central row] only p-polarized scattered light was recorded; while the bottom two figures correspond to recording only s-polarized scattered light [Figs. 47(e) and (f)]. The rough surface, covering an area $16\lambda \times 16\lambda$, was discretized at a grid of 112×112 points corresponding to a distcretization interval $\lambda/7$ for both directions. The presented figures were obtained by averaging the mean differential reflection coefficient over $12,000$ surface realizations. (After Ref. [224].)

direction [36]. For normal incidence, the **k**-vector used to define the incident Gaussian beam, does not (together with $\hat{\mathbf{x}}_3$) define a plane of incidence. However, we have used the convention in the simulations, that the plane of incidence is defined as the plane having $\hat{\phi}_0 = -\sin\phi_0\hat{\mathbf{q}}_1 + \cos\phi_0\hat{\mathbf{q}}_2$ as its normal vector which is well-defined for all polar angles of incidence (also $\theta_0 = 0°$) and coincides with the usual definition when $\theta_0 \neq 0$. Since $\phi_0 = 0°$ was assumed for all the simulation results presented, it follows (with this convention) that the plane of incidence is the q_1q_3-plane. With this definition for the plane of incidence, we may rephrase the above observation: For co- and cross-polarized scattering the dipole-like pattern is oriented *along* and *perpendicular* to the plane of incidence, respectively. Below we will see that this statement also holds true for non-normal incidence.

We now turn our attention to the scattering for non-normal incidence. In Figs. 48 we present the results for the angular distribution of the mean differential reflection coefficient for either a *p*- or *s*-polarized Gaussian beam incident onto the surface at a polar angle $\theta_0 = 20°$ and scattered into various polarization states. From Figs. 48(a) and (b), for which the polarization of the scattered light is not recorded, one observes that there are pronounced enhanced backscattering peaks located around the backscattering direction (at $\theta_s = 20°$ and $\phi_s = 180°$). It is also observed that the *p*-polarized incident beam tends to scatter more light into the forward plane ($q_1 > 0$) than does an *s*-polarized incident beam.

The first thing to notice from Figs. 48(c)–(f), where the polarization of the scattered light is recorded, is that the co-polarized scattering shows up as an elongated structure with the long axis of the pattern directed along the plane of incidence, while the cross-polarized scattering has the long axis of the scattering pattern perpendicular to this plane. This observation is in agreement with what was already observed above for normal incidence. However, for non-normal incidence, the patterns do show less symmetry, as expected, and an even richer and more complicated angular structure. In principle, the enhanced backscattering peak phenomenon should exist in both co- and cross-polarized scattering [215,233,234]. However, for the roughness parameters assumed in this work, one observes instead of a well-pronounced peak in the backscattering direction, a ridge of *constant* enhanced intensity in parts of the backscattering plane ($q_1 < 0$) forming (what seems to be) a half circle of constant polar scattering angle $\theta_s \approx \theta_0 = 20°$ with $\phi_s \in [90°, 270°]$ (Figs. 48(d) and (e)). In exactly the backscattering direction, $\theta_s = \theta_0$ and $\phi_s = 180°$, there seems to be little, if any, "extra" enhancement in the cross-polarized scattering as compared to the intensities at other values of ϕ_s in the interval $[90°, 270°]$. The enhancement ridge seen is Figs. 48(d) and (e) we speculate is caused by a constructive interference effect similar in nature to the underlying enhanced backscattering.

In passing, we note that having available only the in-plane and out-of-plane results for the same angle of incidence, the local enhancements observed in *e.g.* Figs. 45(b) and 46(b) for $\theta_0 = 20°$, could easily have been mistaken for well-localized features in the backscattering direction, similar to what one has for co-polarized scattering (Figs. 48(c) and (f)). In this respect, the angular intensity distributions of the kind presented in Figs. 47–49 can provide important contributions to a better understanding of the multiple scattering phenomena.

Figures 49 present contour plots of the angular distributions of the mean differential reflection coefficient for a polar angle of incidence $\theta_0 = 40°$. Since these results rather closely resembles those of Figs. 48, we will not discuss them further. However, we note that the structures due to coherent interference seen in the cross-polarized components for $\theta_0 = 20°$, are much harder to identify in the results for $\theta_0 = 40°$. This is believed to be caused by the relatively large angle of incidence, for which it is known that coherent effects become weaker [232].

Electromagnetic wave scattering from two-dimensional randomly rough surfaces is a rich phenomenon where open questions still remains. Only recently has it been practically possible, due to the high demand on computer power, to conduct rigorous computer simulations for this problem and to obtain the full angular intensity distribution of the scattered light. With computers getting increasingly more powerful, it is to be expected that such simulations will

[36] The simulation results reported herein assumed an azimuthal angle of $\phi_0 = 0°$ which also determines the directions of the electric field vector associated with the incident Gaussian beam, and also defines (in our convention) the rotation angle of the incident plane. Another choice for ϕ_0 would consequently also alter the orientation of the dipole-like patterns.

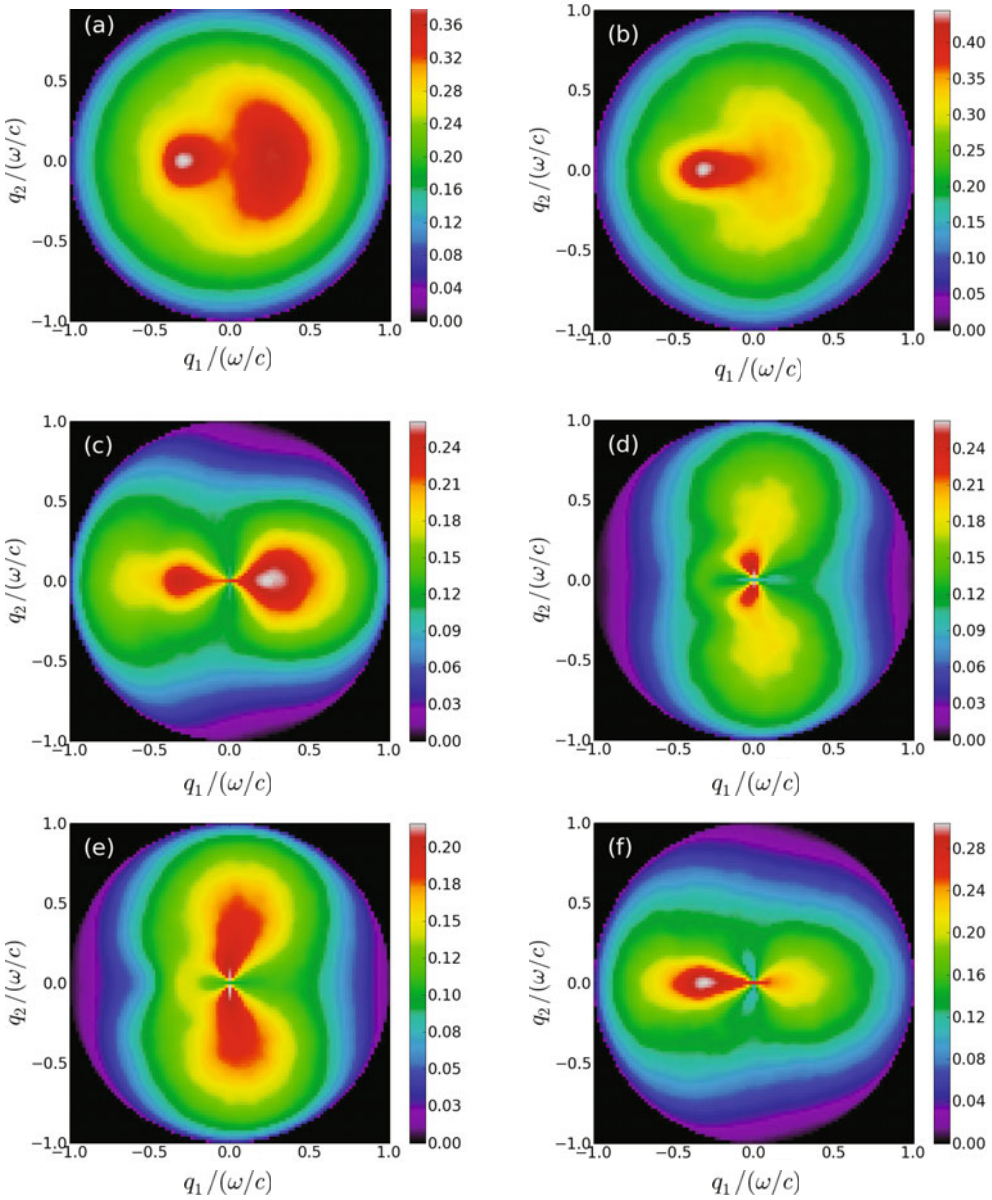

Fig. 48. Same as Figs. 47, but for a polar angle of incidence $\theta_0 = 20°$. (After Ref. [224].)

become available in the coming years. This will, for instance, open for a direct comparison of experimental and rigorous numerical simulation results for the intensity of the light scattered from strongly rough surface. In the past, this has only do done for weakly rough surfaces, or by the use of various approximate methods for calculating the scatted field [67, 222].

6 Concisions and directions for future research

In this review we have introduce the rich field of electromagnetic wave scattering from randomly rough surfaces, presented a selection of multiple scattering effects and their explanations, as well as given an account of the present status of the field. Since rough surfaces are abundant in nature and technological man-made systems, the topic of this review is relevant in numerous

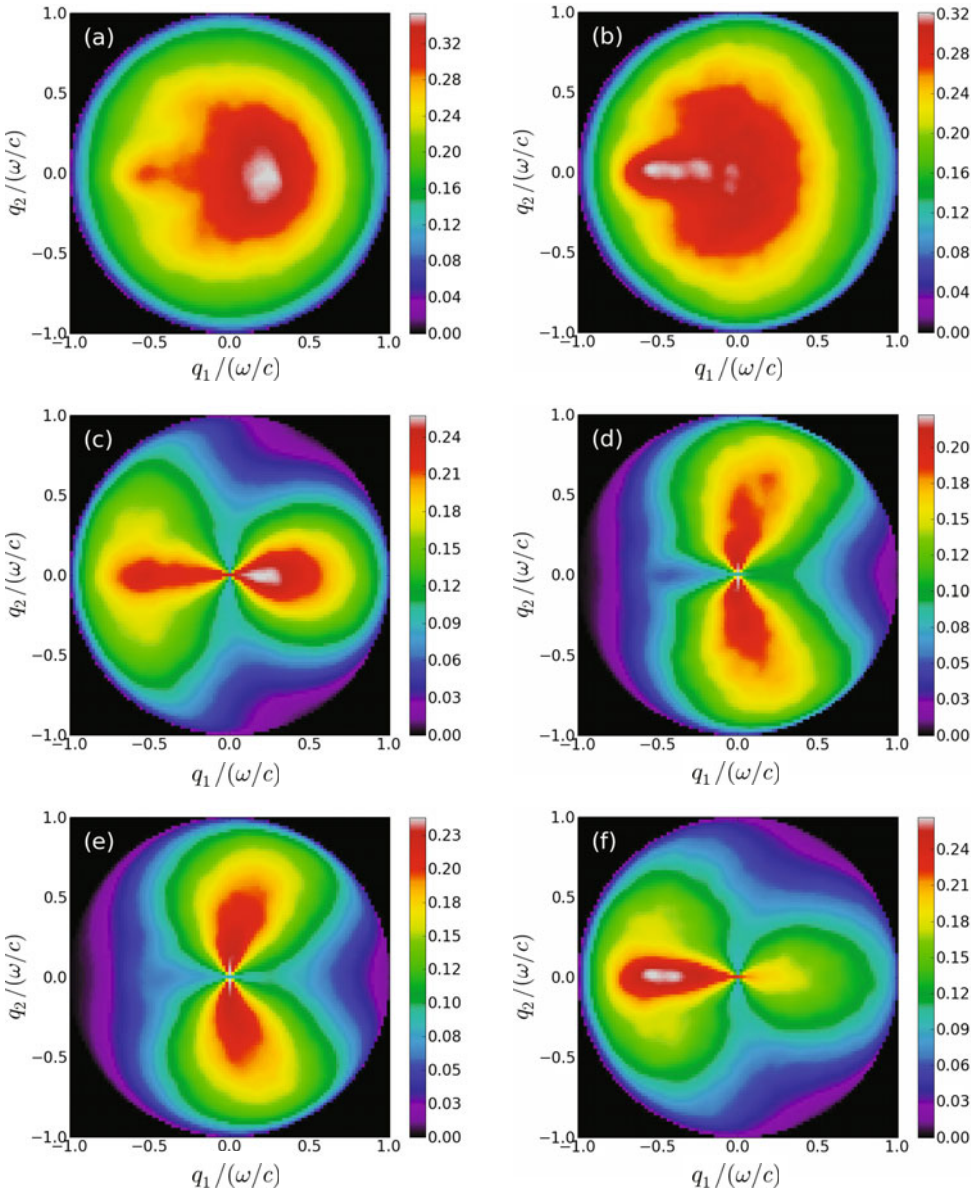

Fig. 49. Same as Figs. 47, but for a polar angle of incidence $\theta_0 = 40°$. (After Ref. [224].)

fields of science and engineering. With this in mind, our aim when preparing this review was to make the presented material accessible to a wider audience, that is, to make it available to non-specialists that "simply" wanted an introduction or a better understanding of what can happen when light is interacting with randomly rough surfaces.

To achieve this goal, we introduced the statistical method used to characterize and describe randomly rough surface; we presented some of the analytic and numerical technique most frequently used to study the rough surface scattering problem; and finally we described and explained the physical origins of a selection of multiple scattering phenomena, both linear and non-linear, that may exist when light is scattered from, or transmitted through, surface random systems.

Even though much is already known about wave scattering from randomly rough surfaces, there are still, after more than a century of intense research, many questions that have not

been properly addressed, and new ones that have been raised recently partly due to advances in nano-technology or being motivated by applications.

One of the remaining open problems in the field of wave scattering from discorded systems, concerns geometries consisting of, for instance, a random volume disordered substrate bounded by a randomly rough surface. This problem has so far been given only little attention and is unsolved in its general form, in spite of some progress made recently for the simplest geometry of this kind [235–239]. In order to make progress towards a solution of this problem, the two wave scattering communities, working on volume and surface disorder systems, will have to work closely together.

Another scattering geometry that needs more attention in the future is one where some of the media involved are characterized by inhomogeneous dielectric functions [240] or anisotropic dielectric tensors [1]. For instance, it is of interest to study the scattering from a randomly rough surface bounded by an anisotropic substrate where, for example, the dielectric properties in the mean plan are different from those perpendicular to the same plane.

Work still remains in the classic one-dimensional scattering problem where a substrate of homogeneous and isotropic dielectric properties is bounded by a randomly rough surfaces. Here, one of the main challenges is related to properly being able to handle the situation when the light is incident on the rough surface at grazing angle of incidence.

Even if the problem of scattering from two-dimensional randomly rough surfaces has been worked on for decades, and important new results keep getting published [224,225], this problems still needs more focus and attention. First, one needs to work towards more accurate theoretical approached, but, not the least, also more efficient algorithms for its numerical solution where the rapid development in modern computer hardware and architecture is taken into consideration. Second, the properties of scattering systems that are bounded by several two-dimensional randomly rough interfaces need to be investigated, and progress on this problem will have practical implications on, *e.g.*, the design and the efficiency of photovoltaic systems. Moreover, a comparison of experimental and (rigorous) computer simulations results for the angular intensity distributions of the scattered or transmitted light needs to be performed for well-characterized, strongly rough metal or dielectric surfaces.

The final suggestion for further research to be given here is related to the important problem of optical inverse scattering [15,34,241,242]. Such problems takes on at least two forms. In the first, one tries to design optical surface rough elements so that the scattered (or transmitted) light has well-defined angular or spectral properties. For this problem, significant progress has recently been made [34], but still new geometries and, not the least, applications of these techniques will need more research and development. In the second form of the optical inverse surface scattering problem, one is faced with the challenge of determining the surface statistics or reconstructing the topography of the randomly rough surface from the scattered intensity or the scattered field amplitudes and phases in the far or near field zone [15,241]. This problem, like any inverse problem, is rather challenging and much more work needs to be dedicated to it in order to make significant progress. A satisfactory solution to this problem will potentially have far reaching consequences for optical characterization methods and remote sensing of micro- or nano-scale structures.

It is to hope that this review can contribute to more interest in, and understanding of, rough surface scattering problems in general. Since randomly rough surfaces are abundant in nature, scientists and engineers from many different disciplines are expected to benefit from advances made in the study of rough surface scattering when, for instance, interpreting their experimental results. If this review can prompt non-specialists to the field of optics of disorder surfaces to be more aware of, and, in particular, start to use for their own research the advances made within rough surface scattering studies over the years, the time put into preparing this review was well spent.

It is a pleasure to acknowledge fruitful discussion on topics related to this review with numerous friends and colleagues: Alex Hansen, Ola Hunderi, Tamara A. Leskova, Alexei A. Maradudin, Eugenio R. Méndez, Stéphane Roux, and Damien Vandembroucq. Moreover, the author thanks numerous of his students, in particular T. Berg, for assisting in identifying misprints in formulae and pointing out

unclear and misleading formulations in an early version of the manuscript. Finally, the author is grateful to T. Berg, T.A. Leskove, E.R Méndez, and K.A. O'Donnell for sharing theirs data and figures, and to Department of Physics and Astronomy, University of California, Irvine for kind hospitality during the time that part of this research was conducted.

This research was supported in part by The Research Council of Norway via småforsk and Contract No. 32690/213, Norsk Hydro ASA, Total Norge ASA, Centre National de la Recherche Scientifique (CNRS), the Army Research Office (DAAD19-99-1-0321), and an NTNU mobility grant.

A Matrix elements

In this appendix, some calculational details are presented for the matrix elements appearing in the matrix equations (136) and that are used to determine the source functions needed in the rigorous numerical simulation approach given in Sec. 4.10.

From this section, Eqs. (137), we recall that the matrix elements are defined as

$$\mathcal{A}^{\pm}_{mn} = \int_{\xi_n-\Delta\xi/2}^{\xi_n+\Delta\xi/2} dx_1'\; A_{\pm}(\xi_m|x_1') \quad = \quad \int_{-\Delta\xi/2}^{\Delta\xi/2} du\; A_{\pm}(\xi_m|\xi_n+u), \tag{A.1a}$$

$$\mathcal{B}^{\pm}_{mn} = \int_{\xi_n-\Delta\xi/2}^{\xi_n+\Delta\xi/2} dx_1'\; B_{\pm}(\xi_m|x_1') \quad = \quad \int_{-\Delta\xi/2}^{\Delta\xi/2} du\; B_{\pm}(\xi_m|\xi_n+u), \tag{A.1b}$$

where we in the last transition have made a change of variable $u = x_1 - \xi_n$ and where the kernels, according to Eqs. (129) and (134), are given by

$$A_{\pm}(x_1|x_1';\omega) = \lim_{\eta\to 0^+} \frac{1}{4\pi}\,\gamma(x_1')\partial_{n'}G_{\pm}(\mathbf{r}|\mathbf{r}';\omega)\Big|_{\substack{x_3=\zeta(x_1)+\eta\,,\\ x_3'=\zeta(x_1')}} \tag{A.2a}$$

$$B_{\pm}(x_1|x_1';\omega) = \lim_{\eta\to 0^+} \frac{1}{4\pi}\,G_{\pm}(\mathbf{r}|\mathbf{r}';\omega)\Big|_{\substack{x_3=\zeta(x_1)+\eta\,,\\ x_3'=\zeta(x_1')}} \tag{A.2b}$$

with $\mathbf{r} = (x_1, x_3)$ and a similar expression holds for $\mathbf{r}'$, and

$$\xi_n = -\frac{L}{2} + \left(n - \frac{1}{2}\right)\Delta\xi, \qquad n = 1, 2, 3, \ldots, N, \tag{A.3}$$

with $\Delta\xi = L/N$. In the above expressions, $G_{\pm}(\mathbf{r}|\mathbf{r}';\omega)$ denote the free-space Green's functions for the Helmholtz equation. In two-dimensions, as we will be considering here, it can be written as [148]

$$G_{\pm}(\mathbf{r}|\mathbf{r}';\omega) = i\pi H_0^{(1)}\left(\sqrt{\varepsilon_{\pm}}\frac{\omega}{c}\,|\mathbf{r}-\mathbf{r}'|\right), \tag{A.4}$$

where $H_0^{(1)}(z)$ denotes the Hankel function of the first kind and zeroth-order [90,148]. By substituting this expression for the Green's function into the kernels, Eqs. (A.2), one gets

$$\begin{aligned} A_{\pm}(x_1|x_1';\omega) = \lim_{\eta\to 0^+} &\left(-\frac{i}{4}\right)\varepsilon_{\pm}\frac{\omega^2}{c^2}\frac{H_1^{(1)}(\chi_{\pm}(x_1|x_1'))}{\chi_{\pm}(x_1|x_1')} \\ &\times\left[(x_1-x_1')\zeta'(x_1') - (\zeta(x_1)-\zeta(x_1')+\eta)\right], \end{aligned} \tag{A.5a}$$

$$B_{\pm}(x_1|x_1';\omega) = \lim_{\eta\to 0^+}\left(-\frac{i}{4}\right)H_0^{(1)}(\chi_{\pm}(x_1|x_1'))\,, \tag{A.5b}$$

where we have defined

$$\chi_{\pm}(x_1|x_1') = \sqrt{\varepsilon_{\pm}(\omega)}\,\frac{\omega}{c}\,\sqrt{(x_1-x_1')^2 + (\zeta(x_1)-\zeta(x_1')+\eta)^2}. \tag{A.5c}$$

Notice that since the Hankel functions are divergent for vanishing argument [90,148], so are the kernels $A_\pm(x_1|x_1';\omega)$ and $B_\pm(x_1|x_1';\omega)$. However, fortunately these singularities are integrable, so the matrix elements $\mathcal{A}^\pm_{mn}$ and $\mathcal{B}^\pm_{mn}$ are actually non-singular everywhere and in particular when $\xi_m = \xi_n$. We will now show this and obtain explicit expressions for these matrix elements.

We start by considering the off-diagonal elements where the kernels are non-singular. In this case, one may approximate the integrals in Eqs. (A.1) by for example the midpoint method [94] with the result that $(m \neq n)$

$$\mathcal{A}^\pm_{mn} = \Delta\xi\ A_\pm(\xi_m|\xi_n;\omega), \tag{A.6a}$$

$$\mathcal{B}^\pm_{mn} = \Delta\xi\ B_\pm(\xi_m|\xi_n;\omega), \tag{A.6b}$$

where the expressions for the kernels are understood to be taken in the form Eqs. (A.5).

So what about the diagonal matrix elements for which the kernels are singular? In order to calculate these elements, we start by noting that $\chi_\pm(\xi_m|\xi_m+u)$, needed in order to evaluate the matrix elements, can be written as

$$\begin{aligned}\chi_\pm(\xi_m|\xi_m+u) &= \sqrt{\varepsilon_\pm}\,\frac{\omega}{c}\,\sqrt{u^2+\left(\zeta'(\xi_m)u+\frac{1}{2}\zeta''(\xi_m)u^2+\ldots+\eta\right)^2}\\ &= \sqrt{\gamma(\xi_m)u^2-2\eta\zeta'(\xi_m)u+\eta^2+\ldots}\\ &= \sqrt{\varepsilon_\pm}\,\frac{\omega}{c}\gamma(\xi_m)|u|+\ldots,\end{aligned} \tag{A.7}$$

where we have Taylor expanded $\zeta(\xi_m+u)$ around ξ_m and used that $\gamma(x_1) = \sqrt{1+\zeta'^2(x_1)}$ (Eq. (124b)). Below we will need the following (small argument) asymptotic expansions for the Hankel functions [90]

$$H_0^{(1)}(z) = \frac{2i}{\pi}\left(\ln\frac{z}{2}+\gamma\right)+1+\mathcal{O}(z^2\ln z), \tag{A.8a}$$

$$\frac{H_1^{(1)}(z)}{z} = -\frac{2i}{\pi}\frac{1}{z^2}+\frac{i}{\pi}\left(\ln\frac{z}{2}+\gamma+\frac{1}{2}\right)-\frac{1}{2}+\mathcal{O}(z^2\ln z), \tag{A.8b}$$

where $\gamma = 0.5772157\ldots$ is the Euler constant.

By introducing these expansions into the kernels, it is rather straightforward to obtain the diagonal matrix elements by integrating the resulting expressions term-by-term. To demonstrate this, we start by handling the $\mathcal{B}^\pm_{mm}$ matrix element. From Eq. (A.6b), with Eqs. (A.5b), (A.7) and (A.8a), it follows that the leading term of the diagonal $\mathcal{B}$-matrix elements is

$$\begin{aligned}\mathcal{B}^\pm_{mm} &= 2\int_0^{\Delta\xi/2} du\ B_\pm(\xi_m|\xi_m+u)\\ &\simeq -\frac{i}{2}\int_0^{\Delta\xi/2} du\ H_0^{(1)}\left(\sqrt{\varepsilon_\pm}\frac{\omega}{c}\gamma(\xi_m)u\right)\\ &= -\frac{i}{2}\int_0^{\Delta\xi/2} du\left[\frac{2i}{\pi}\left\{\ln\left(\sqrt{\varepsilon_\pm}\frac{\omega}{c}\gamma(\xi_m)u\right\}+\gamma\right)+1+\ldots\right]\\ &= -\frac{i}{2}\frac{\Delta\xi}{2}\left[\frac{2i}{\pi}\left\{\ln\left(\sqrt{\varepsilon_\pm}\frac{\omega}{c}\frac{\gamma(\xi_m)\Delta\xi}{2e}\right)+\gamma\right\}+1+\ldots\right]\\ &\simeq -\frac{i}{4}\Delta\xi\,H_0^{(1)}\left(\sqrt{\varepsilon_\pm}\frac{\omega}{c}\frac{\gamma(\xi_m)\Delta\xi}{2e}\right),\end{aligned} \tag{A.9}$$

where in the last transition we have used Eq. (A.8a) once again.

Furthermore, and in a similar fashion, it follows from the use of Eqs. (A.8b) and (A.7) that the leading term of the diagonal elements of $\mathcal{A}$ can be written

$$\begin{aligned}
\mathcal{A}^{\pm}_{mm} &= \int_{-\Delta\xi/2}^{\Delta\xi/2} du\; A_{\pm}(\xi_m|\xi_m+u) \\
&= \frac{i}{4}\varepsilon_{\pm}\frac{\omega^2}{c^2}\lim_{\eta\to 0^+}\int_{-\frac{\Delta\xi}{2}}^{\frac{\Delta\xi}{2}} du\left[-\frac{2i}{\pi}\frac{1}{\chi^2_{\pm}(\xi_m|\xi_m+u)}+\ldots\right]\left[\eta+\frac{1}{2}\zeta''(\xi_m)u^2+\ldots\right] \\
&= \lim_{\eta\to 0^+}\frac{1}{2\pi}\int_{-\frac{\Delta\xi}{2\eta}}^{\frac{\Delta\xi}{2\eta}} du\;\frac{1}{\gamma^2(\xi_m)u^2-2\zeta'(\xi_m)u+1} \\
&\quad +\frac{1}{4\pi}\frac{\zeta''(\xi_m)}{\gamma^2(\xi_m)}\int_{-\frac{\Delta\xi}{2}}^{\frac{\Delta\xi}{2}} du \\
&= \frac{1}{2\pi}\lim_{\eta\to 0^+}\left[\tan^{-1}\left(-\zeta'(\xi_m)+\gamma(\xi_m)u\right)\right]_{u=-\frac{\Delta\xi}{2\eta}}^{\frac{\Delta\xi}{2\eta}}+\Delta\xi\frac{\zeta''(\xi_m)}{4\pi\gamma^2(\xi_m)} \\
&= \frac{1}{2}+\Delta\xi\frac{\zeta''(\xi_m)}{4\pi\gamma^2(\xi_m)}.
\end{aligned} \tag{A.10}$$

To summarize, we have the following expressions for the matrix elements [38,66,68,139]

$$\mathcal{A}^{\pm}_{mn} = \begin{cases} \Delta\xi\, A_{\pm}(\xi_m|\xi_n), & m\neq n, \\ \frac{1}{2}+\Delta\xi\,\frac{\zeta''(x_m)}{4\pi\gamma^2(\xi_m)}, & m=n, \end{cases} \tag{A.11}$$

and

$$\mathcal{B}^{\pm}_{mn} = \begin{cases} \Delta\xi\, B_{\pm}(\xi_m|\xi_n), & m\neq n, \\ -\frac{i}{4}\Delta\xi\, H_0^{(1)}\left(\sqrt{\varepsilon_{\pm}}\frac{\omega}{c}\frac{\gamma(\xi_m)\Delta\xi}{2e}\right), & m=n. \end{cases} \tag{A.12}$$

In these equations, $A_{\pm}(\xi_m|\xi_n)$ and $B_{\pm}(\xi_m|\xi_n)$ are given by Eqs. (A.2).

B The χ-functions used in small amplitude perturbation theory

In this appendix some of the lengthy formulae found in small amplitude perturbation theory, Sec. 4.6, are given. In particular, we have given the first few χ-functions found in Eqs. (91). We will now in the next two subsections explicitly give these functions for p and s-polarization. All explicit reference to the frequency ω has been suppressed. We have also for completeness used ε_0 for the dielectric constant of the upper medium. In the case of vacuum this constant is $\varepsilon_0 = 1$.

B.1 p-polarization

The three first functions in the set $\{\chi_p^{(n)}\}$ are [109,117]:

$$\chi_p^{(1)}(q|k) = \frac{\varepsilon-\varepsilon_0}{\varepsilon\alpha_0(q)+\varepsilon_0\alpha(q)}\left[\varepsilon_0\alpha(q)\alpha(k)-\varepsilon qk\right]\frac{2\alpha_0(k)}{\varepsilon\alpha_0(k)+\varepsilon_0\alpha(k)}, \tag{B.13a}$$

$$\begin{aligned}
\chi_p^{(2)}(q|p_1|k) &= \frac{\varepsilon-\varepsilon_0}{\varepsilon\alpha_0(q)+\varepsilon_0\alpha(q)}\left\{\varepsilon\alpha(q)\left[\alpha_0^2(k)-qk\right]+\varepsilon_0\alpha(k)\left[\alpha^2(q)-qk\right]\right\}\frac{2\alpha_0(k)}{\varepsilon\alpha_0(k)+\varepsilon_0\alpha(q)} \\
&\quad -2\frac{(\varepsilon-\varepsilon_0)^2}{\varepsilon\alpha_0(q)+\varepsilon_0\alpha(q)}\frac{\alpha(q)\alpha_0(p_1)+qp_1}{\varepsilon\alpha_0(p_1)+\varepsilon_0\alpha(p_1)}\frac{2\alpha_0(k)\left[\varepsilon_0\alpha(p_1)\alpha(k)-\varepsilon p_1k\right]}{\varepsilon\alpha_0(k)+\varepsilon_0\alpha(k)},
\end{aligned} \tag{B.13b}$$

and

$$\begin{aligned}\chi_p^{(3)}(q|p_1|p_2|k) = \frac{\varepsilon-\varepsilon_0}{\varepsilon\alpha_0(q)+\varepsilon_0\alpha(q)}\big\{&2\varepsilon\alpha^2(q)\alpha_0^2(k)+\left[\alpha^2(q)+\alpha_0^2(k)\right]\left[\varepsilon_0\alpha(q)\alpha(k)-\varepsilon qk\right]\\ &-2\varepsilon_0 qk\alpha(q)\alpha(k)\big\}\frac{2\alpha_0(k)}{\varepsilon\alpha_0(k)+\varepsilon_0\alpha(k)}\\ &-3\frac{\varepsilon-\varepsilon_0}{\varepsilon\alpha_0(q)+\varepsilon_0\alpha(q)}\left[\alpha(q)\alpha_0(p_1)+qp_1\right]\frac{\varepsilon-\varepsilon_0}{\varepsilon\alpha_0(p_1)+\varepsilon_0\alpha(p_1)}\\ &\times\left\{\varepsilon\alpha(p_1)\left[\alpha_0^2(k)-p_1k\right]+\varepsilon_0\alpha(k)\left[\alpha^2(p_1)-p_1k\right]\right\}\frac{2\alpha_0(k)}{\varepsilon\alpha_0(k)+\varepsilon_0\alpha(k)}\\ &-\Bigg\{3\frac{\varepsilon-\varepsilon_0}{\varepsilon\alpha_0(q)+\varepsilon_0\alpha(q)}\left[\alpha(q)\alpha_0(p_2)+qp_2\right]\left[\alpha(q)-\alpha_0(p_2)\right]\\ &-6\frac{\varepsilon-\varepsilon_0}{\varepsilon\alpha_0(q)+\varepsilon_0\alpha(q)}\left[\alpha(q)\alpha_0(p_1)+qp_1\right]\\ &\times\frac{\varepsilon-\varepsilon_0}{\varepsilon\alpha_0(p_1)+\varepsilon_0\alpha(p_1)}\left[\alpha(p_1)\alpha_0(p_2)+p_1p_2\right]\Bigg\}\\ &\times\frac{\varepsilon-\varepsilon_0}{\varepsilon\alpha_0(p_2)+\varepsilon_0\alpha(p_2)}\left[\varepsilon_0\alpha(p_2)\alpha(k)-\varepsilon p_1k\right]\frac{2\alpha_0(k)}{\varepsilon\alpha_0(k)+\varepsilon_0\alpha(k)}.\end{aligned}\tag{B.13c}$$

B.2 *s*-polarization

Here follows the corresponding expressions for *s*-polarization [109,117]:

$$\chi_s^{(1)}(q|k) = \frac{\omega^2}{c^2}\frac{\varepsilon_0-\varepsilon}{\alpha_0(q)+\alpha(q)}\frac{2\alpha_0(k)}{\alpha_0(k)+\alpha(k)},\tag{B.14a}$$

$$\chi_s^{(2)}(q|p_1|k) = \frac{\omega^2}{c^2}\frac{\varepsilon_0-\varepsilon}{\alpha_0(q)+\alpha(q)}\left(\alpha(q)+\alpha(k)+2\frac{\omega^2}{c^2}\frac{\varepsilon_0-\varepsilon}{\alpha_0(p_1)+\alpha(p_1)}\right)\frac{2\alpha_0(k)}{\alpha_0(k)+\alpha(k)},\tag{B.14b}$$

and

$$\begin{aligned}\chi_s^{(3)}(q|p_1|p_2|k) = \frac{\omega^2}{c^2}\frac{\varepsilon_0-\varepsilon}{\alpha_0(q)+\alpha(q)}\Bigg\{&\alpha^2(q)+2\alpha(q)\alpha(k)+\alpha_0^2(q)\\ &+3\frac{\omega^2}{c^2}\frac{\varepsilon_0-\varepsilon}{\alpha_0(p_1)+\alpha(p_1)}\left[\alpha(p_1)+\alpha(k)\right]+3\left[\alpha(q)-\alpha_0(p_1)\right]\\ &+2\frac{\omega^2}{c^2}\frac{\varepsilon_0-\varepsilon}{\alpha_0(p_1)+\alpha(p_1)}\frac{\omega^2}{c^2}\frac{\varepsilon_0-\varepsilon}{\alpha_0(p_2)+\alpha(p_2)}\Bigg\}\frac{2\alpha_0(k)}{\alpha_0(k)+\alpha(k)}.\end{aligned}\tag{B.14c}$$

With these expressions we close this appendix.

References

1. J.D. Jackson, *Classical Electrodynamics*, 3rd edn. (John Wiley & Sons, New York, 1999)
2. J.A. Stratton, *Electromagnetic Theory*, IEEE Press Series on Electromagnetic Wave Theory (John Wiley & Sons, New Jersey, 2007)
3. L.D. Landau, E.M. Lifshitz, *The Classical Theory of Fields*, 4th revised English edn. vol. 2 of Course of Theoretical Physics (Butterworth-Heinemann, 1980)
4. J.A. Kong, *Electromagnetic Wave Theory* (EMW Publishing, Cambridge, 2005)

5. J.G. Van Bladel, *Electromagnetic Fields*, 2nd edn. IEEE Press Series on Electromagnetic Wave Theory (John Wiley & Sons, New Jersey, 2007)
6. W.K.H. Panofsky, M. Phillips, *Classical Electricity and Magnetism*, 2nd edn. (Addison-Wesley Publishing Company, Reading, MA, 1962)
7. B. Thidé, *Electromagnetic Field Theory*, 2nd edn. (`http://www.plasma.uu.se/CED/Book/, 2009`)
8. W.C. Chew, *Waves and Fields in Inhomogeneous Media*, IEEE Press Series on Electromagnetic Wave Theory (IEEE Press, New Jersey, 1995)
9. M. Born, E. Wolf, *Principles of Optics : Electromagnetic Theory of Propagation, Interference and Diffraction of Light*, 7th (expanded) edn. (Cambridge University Press, Cambridge, 1999)
10. E. Hecht, *Optics*, 4th edn. (Addison Wesley, New York, 2001)
11. L. Novotny, B. Hecht, *Principles of Nano-Optics* (Cambridge University Press, Cambridge, 2006)
12. P. Sheng, *Introduction to Wave Scattering, Localization and Mesoscopic Phenomena*, 2nd edn. Springer Series in Materials Science (Springer-Verlag, New York, 2006)
13. H.M. Pedersen, J. Opt. Soc. Am. **66**, 1204 (1976)
14. J.W. Goodman, *Statistical Optics* (Wiley, New York, 1985)
15. J.-J. Greffet, R. Carminati, Speckle Pattern in the Near Field, in *Light Scattering and Nanoscale Surface Roughness*, edited by A.A. Maradudin (Springer-Verlag, New York, 2007), 409–435
16. Lord Rayleigh, Proc. R. Soc. London Ser. A **79**, 399 (1907)
17. Lord Rayleigh, *The theory of sound* (Dover, New-York, 1945)
18. A.G. Voronovich, Rayleigh Hypothesis in *Light Scattering and Nanoscale Surface Roughness*, edited by A.A. Maradudin (Springer-Verlag, New York, 2007), 93–107
19. L.I. Mandel'shtam, Ann. Physik **41**, 609 (1913)
20. S.O. Rice, Commun. Pure Appl. Math. **4**, 351 (1951)
21. M.A. Isakovich, Zh. Eksp. Teor. Fiz **23**, 305 (1952)
22. D.W Berreman, Phys. Rev. **163**, 855 (1967)
23. D. Beaglehole, O. Hunderi, Phys. Rev. B **2**, 309 (1970)
24. O. Hunderi, D. Beaglehole, Phys. Rev. B **2**, 321 (1970)
25. P. Beckmann, A. Spizzichino, *The scattering from electromagnetic waves from rough surfaces*, (Artech House, 1963)
26. F.G. Bass, I.M. Fuks, *Wave Scattering from Statistically Rough Surfaces* (Pergamon, Oxford, UK, 1979)
27. A. Ishimaru, *Wave Propagation and Scattering in Random Media* (Academic Press, New York, 1978)
28. A. Ishimaru, *Electromagnetic Wave Propagation, Radiation and Scattering* (Prentice Hall, Englewood Cliff, NJ, 1991)
29. J.A. Ogilvy, *Theory of wave scattering from random rough surfaces* (IOP Publishing, Bristol, UK, 1991)
30. M. Nieto-Vesperinas, *Scattering and Diffraction in Physical Optics* (John Wiley & Sons, New York, 1991)
31. M. Nieto-Vesperinas and J.C. Dainty (Eds.) *Scattering in Volumes and Surfaces* (North Holland, Amsterdam, 1990)
32. A.G. Voronovich, *Wave scattering from Rough Surfaces*, 2nd edn. (Springer Verlag, 1999)
33. A.A. Maradudin, ed., *Light Scattering and Nanoscale Surface Roughness* (Springer-Verlag, New York, 2007)
34. A.A. Maradudin, E.R. Méndez, T.A. Leskova, *Designer Surfaces* (Elsevier, Amsterdam, 2008)
35. W.C. Chew, J.-M. Jin, C.-C. Lu, E. Michielssen, J.M. Song, IEEE Trans. Antennas Propagat. **45**, 533 (1997)
36. K.F. Warnick, W.C. Chew, Waves Random Media **11**, R1 (2001)
37. M. Saillard, A. Sentenac, Waves Random Media **11**, R103 (2001)
38. V. Freilikher, E. Kanzieper, A.A. Maradudin, Phys. Rep. **288**, 127 (1997)
39. A.V. Zayats, I.I. Smolyaninov, A.A. Maradudin, Phys. Rep. **408**, 131 (2005)
40. A.V. Shchegrov, A.A. Maradudin, E.R. Méndez, Multiple Scattering of Light from Randomly Rough Surfaces, in *Progress in Optics* vol. XLVI, edited by E. Wolf (Elsevier, Amsterdam, 2004), 117–241
41. A.A. Maradudin, E.R. Méndez, Sci. Prog. **90**, 161 (2007)
42. J.A. DeSanto, Overview of rough surface scattering, in *Light Scattering and Nanoscale Surface Roughness*, edited by A.A. Maradudin (Springer-Verlag, New York, 2007), 211–237
43. S.A. Maier, *Plasmonics: Fundamentals and Applications* (Springer-Verlag, Berlin, 2007)

44. M.L. Brongersma, P.G. Kik (Eds.), *Surface Plasmon Nanophotonics* (Springer-Verlag, New York, 2009)
45. T. Berg, *Numerical study of light scattering from rough surfaces* (MSc thesis, Norwegian University of Science and Technology (NTNU), Trondheim, Norway, 2006)
46. T.A. Leskova, A.A. Maradudin, Multiple-scattering Effects in Angular Intensity Correlation Functions, in *Light Scattering and Nanoscale Surface Roughness*, edited by A.A. Maradudin (Springer-Verlag, New York, 2007), 371–409
47. C.S. West, K.A. O'Donnell J. Opt. Soc. Am. A **12**, 390 (1995)
48. K.A. O'Donnell, Experimental studies of scattering from weakly rough surfaces, in *Light Scattering and Nanoscale Surface Roughness*, edited by A.A. Maradudin (Springer-Verlag, New York, 2007), 237–259
49. A.A. Maradudin, I. Simonsen, T.A. Leskova, E.R. Méndez, Opt. Lett. **24**, 1257 (1999)
50. E.R. Méndez, E.E. Garcia-Guerrero, T.A. Leskova, A.A. Maradudin, J. Muñoz-Lopez, I. Simonsen Appl. Phys. Lett. **81**, 798 (2002)
51. A.A. Maradudin, I. Simonsen, T.A. Leskova, E.R. Méndez, Waves Random Media **11**, 529 (2001)
52. T.A. Leskova, A.A. Maradudin, E.E. García-Guerrero, E.R. Méndez, Metamaterials **1**, 19 (2007)
53. S. Fahr, C. Rockstuhl, F. Lederer Appl. Phys. Lett. **92**, 171114 (2008)
54. J.M. Bennet, L. Mattsson, *Introduction to Surface Roughness ans Scattering*, 2nd edn. (Optical Society of America, Washington D.C., 1999)
55. J.M. Bennet, Characterization of Surface Roughness, in *Light Scattering and Nanoscale Surface Roughness*, edited by A.A. Maradudin (Springer-Verlag, New York, 2007), 1–35
56. S. Ross, *Introduction to Probability Models*, 6th edn. (Academic Press, San Diego, 1997)
57. W. Feller, *An Introduction to Probability Theory and its Applications* Vol. 1, 3rd edn. (John Wiley & Sons, New York, 1968)
58. W. Feller, *An Introduction to Probability Theory and its Applications* Vol. 2, 2nd edn. (John Wiley & Sons, New York, 1971)
59. E. Parzen, *Stochastic processes* (Holden-Day, San Francisco, 1962)
60. A. Papoulis, *Probability, random variables, and stochastic processes*, 2nd edn. (McGraw-Hill, New York, 1984)
61. A. Papoulis, *Probability and statistics* (Prentice Hall, Englewood Cliffs, NJ, 1990)
62. A. Mendoza-Suárez, E.R. Méndez, Appl. Opt. **36**, 3521 (1997)
63. A. Mendoza-Suárez, E.R. Méndez, Opt. Commun. **134**, 241 (1997)
64. A.A. Maradudin, T. Michel, J. Stat. Phys. **58**, 485 (1990)
65. S. West, K.A. O'Donnell, J. Opt. Soc. Am. A**12**, 390 (1995)
66. A.A. Maradudin, T. Michel, A.R. McGurn, E.R. Méndez, Ann. Phys. **203**, 255 (1990)
67. J.T. Johnson, Computer Simulations of Rough Surface Scattering, in *Light Scattering and Nanoscale Surfaces Roughness*, edited by A.A. Maradudin (Springer, New York, 2007), 181–211
68. I. Simonsen, T.A. Leskova, A.A. Maradudin, O. Hunderi, Proc. Int. Soc. Opt. Eng. **4100**, 65 (2000)
69. P. Meakin, Phys. Rep. **235**, 189 (1993)
70. L. Barabasi, H.E. Stanley, *Fractal Growth Models* (Cambridge University Press, Cambridge, 1995)
71. P. Meakin, *Fractals, scaling and growth far from equilibrium* (Cambridge University Press, 1998)
72. E. Bouchaud, G. Lapasset, J. Planès, Europhys. Lett, **13**, 73 (1990)
73. J. Schmittbuhl, Ph.D. thesis, Université Paris 6 (1994)
74. A. Hansen and O. M. Nes, *IKU Report,* unpublished, 1997
75. F. Plouraboué, M. Boehm, Trib. Int. **32**, 45 (1999)
76. T. Vicsek, M. Cserzö, V.K. Horváth, Physica A **167**, 315 (1990)
77. J. Feder, *Fractals* (Plenum, New York, 1988)
78. I. Simonsen, A. Hansen, O.M. Nes Phys. Rev. E **58**, 2779 (1998)
79. C.K. Peng *et al.* Phys. Rev. E **49**, 1685 (1994)
80. T. Vicsek, *Fractal growth phenomena*, 2nd edition, (World Scientific, Singapore, 1992)
81. B.B. Mandelbrot, *The fractal geometry of nature* (Freeman, 1975)
82. A.A. Maradudin, in *Surface Polaritons-Electromagnetic Waves at Surfaces and interfaces*, edited by V. M. Agranovich, D. L. Mills (North-holland Publishing Company, 1982)
83. A.A. Maradudin, R.F. Wallis, L. Dobrzynski, *Handbook of Surfaces and interfaces, Volume 3: Surface Phonons and Polaritons* (Garland STPM Press, 1980)
84. O. Keller, (Ed.), *Nonlinear optics in solids* (Springer-Verlag, Berlin, 1990)
85. D.L. Mills, *Nonlinear Optics: Basic Concepts*, 2nd edn. (Springer-Verlag, New York, 1998)

86. R.W. Boyd, *Nonlinear Optics*, 3rd edn. (Academic Press, 2008)
87. C. Kittel, *Introduction to solid state physics*, 7th edition (John Wiley & Sons, New York, 1996)
88. N.W. Ashcroft, N.D. Mermin, *Solid State Physics* (Saunders College, Philadelphia, 1976)
89. I. Simonsen, Enhanced Back and Forward Scattering in the Reflection of Light from Weakly Rough Random Metal Surfaces, to appear phys. stat. sol. (b) (2010)
90. M. Abramowitz, I.A. Stegun, *Handbook of Mathematical Functions* (Dover, New York, 1964)
91. R.J. Potton, Rep. Prog. Phys. **67**, 717 (2004)
92. M.V. de Hoop, A.T. de Hoop, Proc. R. Soc. A Math. **456**, 641 (2000)
93. R. Carminati, M. Nieto-Vesperinas, J.-J. Greffet, J. Opt. Soc. Am. A **15**, 706 (1998)
94. W.H. Press, S.A. Teukolsky, W.T. Vetterling, B.P. Flannery, *Numerical Recipes in fortran,* 2nd edn. (Cambridge University Press, Cambridge, 1992)
95. F. Toigo, A. Marvin, V. Celli, N.R. Hill, Phys. Rev. B **15**, 5618 (1977)
96. A.A. Maradudin, J. Opt. Soc. Am. **73**, 759 (1983)
97. A. Madrazo, A.A. Maradudin, Opt. Commun. **134**, 251 (1997)
98. I. Simonsen, A.A. Maradudin, Opt. Commun. **162**, 99 (1999)
99. T. Watanabe, Y. Choyal, K. Minami, V.L. Granatstein, Phys. Rev. E **69**, 056606 (2004)
100. A.V. Tishchenko, Opt. Express **17**, 17102 (2009)
101. R.F. Millar, Proc. Camb. Phil. Soc. **65**, 773 (1969)
102. R.F. Millar, Proc. Camb. Phil. Soc. **69**, 217 (1971)
103. N.R. Hill, V. Celli, Phys. Rev. B **17**, 2478 (1978)
104. G. Berginc, Small-amplitude Perturbation Theory for Two-dimensional Surfaces, in *Light Scattering and Nanoscale Surfaces Roughness*, edited by A.A. Maradudin (Springer, New York, 2007), 127–181
105. A. Soubret, G. Berginc, C. Bourrely, Phys. Rev. B **63**, 245411 (2001)
106. A. Soubret, G. Berginc, C. Bourrely, J. Opt. Soc. Am. A **18**, 2778 (2001)
107. T.A. Leskova, A.A. Maradudin, Proc. Int. Soc. Opt. Eng. **7065**, 706505 (2008)
108. K.A. O'Donnell, Small-amplitude Perturbation Theory for One-dimensionally Rough Surfaces in *Light Scattering and Nanoscale Surface Roughness*, edited by A.A. Maradudin (Springer-Verlag, New York, 2007), 107–127
109. A. Shchegrov, Ph.D. thesis, University of California, Irvine, USA (1998)
110. E.I. Thorsos, D.R. Jackson, J. Ac. Soc. Am. **66**, 261 (1989)
111. J.M. Soto-Crespo, M. Nieto-Vesperinas, A.T. Friberg, J. Opt. Soc. Am. A **7**, 1185 (1990).
112. M.F. Chen, S.C. Wu, A.K. Fung, J. Wave-Material Interaction **2**, 9 (1987)
113. R. Newton, *Scattering Theory of Waves and Particles*, 2nd edn. (Springer-Verlag, Heidelberg, 1982)
114. G.C. Brown, V. Celli, M. Coopersmith, M. Haller, Surf. Sci. **129**, 129 (1983)
115. G.C. Brown, V. Celli, M. Haller, A. Marvin, Surf. Sci. **136**, 381 (1984)
116. A.A. Maradudin, E.R. Méndez, Appl. Opt. **32**, 3335 (1993)
117. J.A. Sánchez-Gil, A.A. Maradudin, E.R. Méndez, J. Opt. Soc. Am. A **12**, 1547 (1995)
118. K.A. O'Donnell, C.S. West, E.R. Méndez, Phys. Rev. B **57**, 13207 (1998)
119. B.A. Lippmann, J. Schwinger, Phys. Rev. **79**, 469 (1950)
120. G. Brown, V. Celli, M. Haller, A.A. Maradudin, A. Marvin, Phys. Rev. B. **31**, 4993 (1985)
121. S. Takeno, Prog. Theo. Phys. **40**, 942 (1968)
122. H. Bethe, E. Salpeter, Phys. Rev. **84** 1232 (1951)
123. T.N. Antsygina, V.D. Freylikher, S.A. Gredeskul, L.A. Pustur, V.A. Slusarev, Journal of Electromagnetic Waves and Applications **5**, 873 (1991)
124. A.R. McGurn, A.A. Maradudin, V. Celli, Phys. Rev. B **31**, 4866 (1985)
125. J. Shen, A.A. Maradudin, Phys. Rev. B **22**, 4234 (1980)
126. R.M. Fitzgerald, A.A. Maradudin, Waves Random Media **4**, 275 (1994)
127. D. Winebrenner, A. Ishimaru, Radio Sci. **20**, 161 (1985)
128. I. Simonsen, Å. Larsen, E. Andreassen, E. Ommundsen, K. Nord-Varhaug, phys. stat. sol. (b) **242**, 2995 (2005)
129. I. Simonsen, Å. Larsen, E. Andreassen, E. Ommundsen, K. Nord-Varhaug, Phys. Rev. A **79**, 063813 (2009)
130. A.G. Voronovich, Sov. Phys.-JETP **62**, 65 (1985)
131. A.G. Voronovich, Waves Random Media **4**, 337, (1994)
132. A.G. Voronovich, Waves Random Media **6**, 151 (1996)
133. S.K. Sinha, E.B. Sirota, S. Garoff, H.B. Stanley, Phys. Rev. B **38**, 2297 (1988)

134. T.A. Leskova, A.A. Maradudin, Waves Random Media **7**, 395 (1997)
135. G.S. Agarwal, Phys. Rev. B **15**, 2371 (1977)
136. E. Bahar, IEEE Trans. Antennas Propagat. **29**, 443 (1981)
137. D.M. Milder, J. Acoust. Soc. Am. **89**, 529 (1991)
138. E. Rodriguez, Y. Kim, Radio Sci. **27**, 79 (1992)
139. B. Baumeier, T.A. Leskova, A.A. Maradudin, J. Opt. A: Pure Appl. Opt. **8**, S191 (2006)
140. R.F. Harrington, *Field Computation by Moment Methods* (Macmillan, New York, 1968)
141. A.G. Voronovich, The Kirchhoff and related approximations, in *Light Scattering and Nanoscale Surface Roughness*, edited by A.A. Maradudin (Springer-Verlag, New York, 2007), 35–61
142. P.P Ewald, Ann. Physik **49**, 1 (1916)
143. C.W. Oseen, Ann. Physik **48**, 1 (1915)
144. J.J Sein, Opt. Commun. **2**, 170 (1970)
145. G.S. Agarwal, Opt. Commun. **18**, 238 (1976)
146. D.N. Pattanayak, Opt. Commun. **15**, 335 (1975)
147. E. Wolf, A generalized extinction theorem and its role in scattering theory, in *Coherence and Quantum Optics*, edited by L. Mandel, E. Wolf (Plenum, New York: 1973) pp 339–357
148. P.M. Morse, H. Feshbach, *Methods of Theoretical Physics*, Part 1 and 2 (McGraw-Hill, New York, 1953)
149. A. Sommerfeld, *Optics* (Academic Press, 1954)
150. G.H. Golub, C.F. Van Loan, *Matrix Computation* 3rd edn. (The John Hopkins University Press, Baltimore, 1996)
151. M.C.W. van Rossum, Th.M. Nieuwenhuizen, Rev. Mod. Phys. **71**, 313 (1999)
152. P. Sheng, *Scattering and Localization of classical Waves in Random Media* (World Scientific, Singapore, 1990)
153. A. Lagendijk, B.A. van Triggelen, Phys. Rep. **270**, 143 (1996)
154. E. Jakeman, in *Fractals in physics*, edited by L. Pietronero, E. Tossati (Elsevier, 1986)
155. E. Bouchaud, J. Phys. Condens. Matter **9**, 4319 (1997)
156. S. Roux, H. Herrmann, (Eds.), *Statistical Models for the Fracture of Disordered Media* (Elsevier, New York, 1990)
157. E. Bouchaud, G. Lapasset, J. Planés, Europhys. Lett. **13**, 73 (1990)
158. L. Ponson, D. Bonamy, E. Bouchaud, Phys. Rev. Lett. **96**, 035506 (2006)
159. K.J. Måløy, A. Hansen, E.L. Hinrichsen, S. Roux, Phys. Rev. Lett. **68**, 213 (1992)
160. D. Vandembroucq, A. Tarrats, J.-J. Greffet, S. Roux, F. Plouraboué, Opt. Commun. **187**, 289 (2001)
161. I. Simonsen, Physica A **322**, 597 (2003)
162. I. Simonsen, D. Vandembroucq, S. Roux, Phys. Rev. E **61**, 5914 (2000)
163. I. Simonsen, D. Vandembroucq, S. Roux, J. Opt. Soc. Am. A **18**, 5914 (2001)
164. P. Lévy, *Théorie de l'Addition des Variables Aléatoires* (Gauthier-Villars, Paris, 1937)
165. E.D. Palik, (Ed.), *Handbook of Optical Constants of Solids III* (Academic Press, New York, 1998)
166. I. Simonsen, A. Tarrats, D. Vandembroucq, J. Opt. A: Pure Appl. Opt. **4**, S168 (2002)
167. J.Q. Lu, A.A. Maradudin, T. Michel, J. Opt. Soc. Am. B **8**, 311 (1991)
168. E.R. Méndez, K.A. O'Donnell, Opt. Commun. **61**, 91 (1987)
169. K.A. O'Donnell, E. R. Méndez, J. Opt. Soc. Am. A **4**, 1194 (1987)
170. M. Nieto-Vesperinas, J.M. Soto-Crespo, Opt. Lett. **12**, 979 (1987)
171. A.R. McGurn, A.A. Maradudin, Opt. Commun. **72**, 279 (1989)
172. Z.-H. Gu, R.S. Dummer, A.A. Maradudin, A.R. McGurn, E.R. Méndez, Appl. Opt. **30**, 4094 (1991)
173. K.A. O'Donnell, J. Opt. Soc. Am. A **18**, 1507 (2001)
174. K.A. O'Donnell, E.R. Méndez, J. Opt. Soc. Am. A **20**, 2338 (2003)
175. V. Freilikher, M. Pustilnik, I. Yurkevich, Phys. Lett. A **193**, 467 (1994)
176. V. Freilikher, M. Pustilnik, I. Yurkevich, A.A. Maradudin, Opt. Commun. **110**, 263 (1994)
177. J.Q. Lu, A.A. Maradudin, R.F. Wallis, Waves Random Media **1**, 309 (1991)
178. A.R. McGurn, A.A. Maradudin, J. Opt. Soc. Am. B **4**, 910 (1987)
179. A.R. McGurn, A.A. Maradudin, R.F. Wallis, Waves Random Media **1**, 43 (1991)
180. J.A. Sánchez-Gil, A.A. Maradudin, J.Q. Lu, V.D. Freilikher, Phys. Rev. B **51**, 17100 (1995)
181. J.A. Sánchez-Gil, A.A. Maradudin, J.Q. Lu, V.D. Freilikher, M. Pustilnik, I. Yurkevich, Phys. Rev. B**50**, 15353 (1994)
182. J.A. Sánchez-Gil, A.A. Maradudin, J.Q. Lu, V.R. Freilikher, J. Mod. Opt. **43**, 435 (1995)

183. H.M. Escamilla, E.R. Méndez, E.I. Chaikina, J. Opt. Soc. Am. A **18**, 1122 (2001)
184. J.C. Dainty, (Ed.), *Laser Speckle and Related Phenomena* (Springer-Verlag, Berlin, 1975)
185. S. Feng, C. Kane, P.A. Lee, A.D. Stone, Phys. Rev. Lett. **61**, 834 (1988)
186. I. Freund, M. Rosenbluh, Opt. Commun. **82**, 362 (1991)
187. M.P. van Albada, J.F. de Boer, A. Lagendijk, Phys. Rev. Lett. **64**, 2787 (1990)
188. F. Scheffold, G. Maret, Phys. Rev. Lett. **81**, 5800 (1998)
189. V. Malyshkin, A.R. McGurn, T.A. Leskova, A.A. Maradudin, M. Nieto-Vesperinas, Waves Random Media **7**, 479 (1997)
190. C.S. West, K.A. O'Donnell, Phys. Rev B **59**, 2393 (1999)
191. B. Shapiro, Phys. Rev. Lett. **57**, 2168 (1986)
192. N. Garcia, A.Z. Genack, Phys. Rev. Lett. **63**, 1678 (1989)
193. R. Kubo, Phys. Soc. Japan **17**, 1100 (1962)
194. R.K. Pathria, *Statistical Mechanics*, 2nd edn. (Butterworth-Heinemann, Oxford, 1996)
195. T.A. Leskova, I. Simonsen, A.A. Maradudin, Waves Random Media **12**, 307 (2002)
196. I. Simonsen, A.A. Maradudin, T.A. Leskova, Proc. Int. Soc. Opt. Eng. **3784**, 218 (1999)
197. L.B. Felsen and N. Marcuvitz, *Radiation and Scattering of Waves*, (Prentice-Hall, Inc., Engelwood Cliffs, New Jersey, 1973)
198. A. Arsenieva, S. Feng, Phys. Rev. B **47**, 13047 (1993)
199. V. Malyshkin, A.R. McGurn, T.A. Leskova, A.A. Maradudin, M. Nieto–Vesperinas, Opt. Lett. **22**, 946 (1997)
200. A.R. McGurn, A.A. Maradudin, Opt. Commun. **155**, 79 (1998)
201. J.W. Goodman, Opt. Commun. **14**, 324 (1975)
202. M. Leyva-Lucero, E.R. Méndez, T.A. Leskova, A.A. Maradudin, Opt. Commun. **161**, 79 (1999)
203. K.A. O'Donnell, R. Torre, Opt. Commun. **138**, 341 (1997)
204. E.R. Méndez, A.G. Navarrete, R.E. Luna, J. Opt. Soc. Am. A **12**, 2507 (1995)
205. N. Bloembergen, R.K. Chang, S.S. Jha, C.H. Lee, Phys. Rev. **174**,813 (1968)
206. D. Maystre, M. Nevière, Appl. Phys. A **39**, 115 (1986)
207. J.A. Sánchez-Gil, M. Nieto-Vesperinas, J. Opt. Soc. Am. A **8**, 1270 (1991)
208. E.G. Liska, J.J. McCoy, J. Acoust. Soc. Am. **71**, 1093 (1982)
209. A. Sentenac, A.A. Maradudin, Waves Random Media **3**, 343 (1993)
210. K.A. O'Donnell, R. Torre, C.S. West, Opt. Lett. **21**, 1738 (1996)
211. A.R. McGurn, V.M. Agranovich, T.A. Leskova, Phys. Rev. B **44**, 11441 (1991)
212. M. Leyva-Lucero, E.R. Méndez, T.A. Leskova, A.A. Maradudin, J.Q. Lu, Opt. Lett. **21**, 1809 (1996)
213. T.A. Leskova, M. Leyva-Lucero, E.R. Mńdez, A.A. Maradudin, I.V. Novikov, Opt. Commun. **183**, 529 (2000)
214. M.E. Knotts, K.A. O'Donnell, K. A. Opt. Commun. **99**, 1 (1993)
215. E.I. Chaikina, P. Negrete-Regagnon, V. Ruiz-Cortés, E.R. Mendéz, Opt. Commun. **208**, 215 (2002)
216. P. Tran, A.A. Maradudin, Opt. Commun. **110**, 269 (1994)
217. P. Tran, V. Celli, A.A. Maradudin, J. Opt. Soc. Am. A**11**, 1686 (1994)
218. R.L. Wagner, J. Song, W.C. Chew, IEEE Trans. Antennas Propagat. **45**, 235 (1997)
219. L. Tsang, C.H. Chan, K. Pak, Electron. Lett. **29**, 1153 (1993)
220. L. Tsang, C.H. Chan, K. Pak, J. Opt. Soc. A**11**, 711 (1994)
221. K. Pak, L. Tsang, C.H. Chan, J.T. Johnson, J. Opt. Soc. Am. A**12**, 2491 (1995)
222. J.T. Johnson, L. Tsang, R.T. Shin, K. Pak, C.H. Chan, A. Ishimaru, Y. Kuga, IEEE Trans. Antennas Propagat. **44**, 748 (1996)
223. G. Soriano, M. Saillard, J. Opt. Soc. Am. A**18**, 124 (2001)
224. I. Simonsen, A.A. Maradudin, T.A. Leskova, Phys. Rev. A **81**, 013806 (2010)
225. I. Simonsen, A.A. Maradudin, T.A. Leskova, *The Scattering of Electromagnetic Waves from Two-Dimensional Randomly Rough Penetrable Surfaces*, arXiv:1002.2200, To appear Phys. Rev. Lett. (2010)
226. T.A. Leskova, A.A. Maradudin, I. Simonsen, Rev. Mex. Fis. S **54**, 54 (2008)
227. R. Chipman, *Polarimetry*, in Handbook of Optics, Vol. 2, Chapter 22 (McGraw-Hill, 1994)
228. P.S. Hauge, Surf. Sci. **96**, 81 (1980)
229. T.A. Germer, C.C. Asmail, J. Opt. Soc. Am. A **16**, 1326 (1999)
230. K. Sarabandi, Radio Sci. **27**, 553 (1992)
231. I.V. Novikov, A.A. Maradudin, Radio Sci. **34**, 599 (1999)

232. A.R. McGurn, A.A. Maradudin, V. Celli, Phys. Rev. B **31**, 4866 (1985)
233. E.R. Méndez, K.A. O'Donnell, Opt. Commun. **61**, 91 (1987)
234. D. Torrungrueng, J.T. Johnson, J. Opt. Soc. Am. A **18**, 2518 (2001)
235. J.M. Elson, Phys. Rev. B **30**, 5460 (1984)
236. J.M. Elson, J.M. Bennett, J. C. Stove, Appl. Opt. **32**, 3362 (1993)
237. K. Pak, L. Tsang, C.H. Chan, Radio Sci. **28**, 331 (1993)
238. J.M. Elson, Waves Random Media **7**, 303 (1997)
239. A. Sentenac, H. Giovannini, M. Saillard, J. Opt. Soc. Am. A **19**, 727 (2002)
240. K. Sarabandi, T. Chiu, IEEE Trans. Antennas Propagat. **45**, 1419 (1997)
241. E.R. Méndez, D. Macías, Inverse Problems in Optical Scattering, in *Light Scattering and Nanoscale Surface Roughness*, edited by A.A. Maradudin (Springer-Verlag, New York, 2007), 435–465
242. M. Pascual, W. Zierau, T.A. Leskova, A.A. Maradudin, Opt. Commun. **155**, 351 (1998)